REPORT DOCUMENTATION PAGE

AFRL-SR-BL-TR-98-

0746

1. AGENCY USE ONLY (Leave Blank)	2. REPORT DATE May, 1994	3. REPORT TYPE AND DATES COVERED Final

4. TITLE AND SUBTITLE	5. FUNDING NUMBERS
Ultrahigh Vacuum Metalorganic Chemical Vapor Deposition and In Situ Characterization of Nanoscale Titanium Dioxide Films	

6. AUTHORS
Polly Wanda Chu

7. PERFORMING ORGANIZATION NAME(S) AND ADDRESS(ES) Cornell University	8. PERFORMING ORGANIZATION REPORT NUMBER

9. SPONSORING/MONITORING AGENCY NAME(S) AND ADDRESS(ES) AFOSR/NI 4040 Fairfax Dr, Suite 500 Arlington, VA 22203-1613	10. SPONSORING/MONITORING AGENCY REPORT NUMBER

11. SUPPLEMENTARY NOTES

12a. DISTRIBUTION AVAILABILITY STATEMENT Approved for Public Release	12b. DISTRIBUTION CODE

13. ABSTRACT *(Maximum 200 words)*
See Attachment

14. SUBJECT TERMS	15. NUMBER OF PAGES
	16. PRICE CODE

17. SECURITY CLASSIFICATION OF REPORT Unclassified	18. SECURITY CLASSIFICATION OF THIS PAGE Unclassified	19. SECURITY CLASSIFICATION OF ABSTRACT Unclassified	20. LIMITATION OF ABSTRACT UL

DTIC QUALITY INSPECTED 3

ULTRAHIGH VACUUM METALORGANIC CHEMICAL

VAPOR DEPOSITION AND *IN SITU* CHARACTERIZATION OF

NANOSCALE TITANIUM DIOXIDE FILMS

A Dissertation

Presented to the Faculty of the Graduate School

of Cornell University

in Partial Fulfillment of the Requirements for the Degree of

Doctor of Philosophy

by

Polly Wanda Chu

May 1994

ULTRAHIGH VACUUM METALORGANIC CHEMICAL VAPOR DEPOSITION AND *IN SITU* CHARACTERIZATION OF NANOSCALE TITANIUM DIOXIDE FILMS

Polly Wanda Chu, Ph.D.

Cornell University 1994

Thin titanium dioxide films were produced by metalorganic chemical vapor deposition on sapphire(0001) in an ultrahigh vacuum (UHV) chamber. A method was developed for producing controlled submonolayer depositions from titanium isopropoxide precursor. Film thickness ranged from 0.1 to 2.7 nm. *In situ* X-ray photoelectron spectroscopy (XPS) was used to determine film stoichiometry with increasing thickness. The effect of isothermal annealing on desorption was evaluated. Photoelectron peak shapes and positions from the initial monolayers were analyzed for evidence of interface reaction.

Deposition from titanium isopropoxide is divided into two regimes: depositions below and above the pyrolysis temperature. This temperature was determined to be 300°C. Controlled submonolayers of titanium oxide were produced by cycles of dosing with titanium isopropoxide vapor below and annealing above 300°C. Precursor adsorption below the pyrolysis temperature was observed to saturate

after 15 minutes of dosing. The quantity absorbed was shown to have an upper limit of one monolayer. The stoichiometry of thin films grown by the cycling method were determined to be TiO_2.

Titanium dioxide film stoichiometry was unaffected by isothermal annealing at 700°C. Annealing produced a decrease in film thickness. This was explained as due to desorption. Desorption ceased at approximately 2.5 to 3 monolayers, suggesting bonding of the initial monolayers of film to sapphire is stronger than to itself.

Evidence of sapphire reduction at the interface by the depositions was not observed. The XPS O 1s peak shifted with increased film thickness. The shifts were consistent with oxygen in sapphire and titanium dioxide having different O 1s photoelectron peak positions. Simulations showed the total shifts for thin films ranging in thickness of 0.1 to 2.7 nm to be -0.99 to -1.23 eV. Thick films were produced for comparison. Total shifts were -1.07 to -1.19 eV for thick films ranging from 0.1 to 0.15 µm; these films were grown by continuous depositions above the pyrolysis temperature.

Biographical Sketch

Polly Wanda Chu was born in New York City, New York on October 22, 1965. In May 1986, she received a Bachelor of Engineering in Chemical Engineering from The Cooper Union for the Advancement of Science and Art. From 1986 to 1988, she was employed by the Personal Products Company. In 1988, she enrolled in the Department of Materials Science and Engineering at Cornell University. She received her Master of Science in August 1990, and Doctorate in May 1994.

to my parents

Jack and Shuk Wah

and

to Bill

Acknowledgements

I would like to express my gratitude to Professor Rishi Raj, Chairman of the Thesis Committee, for his guidance and help throughout my years at Cornell University. His support and insight were invaluable in producing this work. I also wish to thank Professors Stephen Sass and Frank Disalvo for serving on the Thesis Committee and reviewing my work.

Special thanks goes to Professor Jack Blakely and the members of his research group for generously extending invitations to join in your meetings and activities.

For moral and technical support, I acknowledge the members of the Raj research group. Our discussions and interactions have broadened my technical, cultural, and political horizons. I want to especially acknowledge Dr. Sunggi Baik, Dr. Jiong-Ping Lu, Jean-Louis, Tom, Hsu, Huyang, Venkat, Yujiun, Bob, and Bill.

I also wish to thank my friends, especially Ann Marie, Christian, Steve, Jim, and Darlene, for warm memories of Ithaca.

Table of Contents

List of Tables

List of Figures

List of Abbreviations

AES	Auger electron spectroscopy
AFM	atomic force microscopy
CVD	chemical vapor deposition
IMFP	inelastic mean free path
LEED	low energy electron diffraction
MOCVD	metalorganic chemical vapor deposition
RBS	Rutherford backscattering spectroscopy
RHEED	reflective high energy electron diffraction
TEM	transmission electron microscopy
TPD	temperature-programmed desorption
UHV	ultrahigh vacuum
XPS	X-ray photoelectron spectroscopy
XRD	X-ray diffraction

Chapter 1
Introduction

1.1   Motivation for research

Thin oxide films have properties of interest for fundamental research and technological applications. Among the oxides, titanium dioxide films have been investigated for coating, dielectric, and sensor applications. The epitaxial relationships between titanium dioxide and sapphire are also of interest.

Studies of titanium oxide have generally focused on characterization of films with thicknesses in the μm range. The properties of a film at the initial few monolayers may be different from the bulk film due to effects such as strain at the substrate interface or interfacial reactions. It is of fundamental and technological interest to characterize thin films limited to a few monolayers. To do so requires the capability to produce and analyze thin films with thicknesses in the nanometer range. The use of *in situ* surface sensitive techniques permits characterization of the growing film.

Among the numerous formation techniques available to produce oxide films, the chemical vapor deposition (CVD) method offers versatility and suitability for a range of systems. In metalorganic chemical vapor deposition (MOCVD) organic compounds are used as precursors to grow metal oxides. Alkoxide precursors used in MOCVD contain the metal and oxygen. The use of a second source of oxygen is

1

unnecessary. The processes which occur in CVD are of fundamental interest.

1.2   Statement of purpose

The *in situ* characterization of thin titanium dioxide films grown on sapphire(0001) by MOCVD from titanium isopropoxide precursor are discussed in this work. The films analyzed had thicknesses ranging from submonolayer to monolayers. Deposition and *in situ* analysis were conducted in an ultrahigh vacuum (UHV) chamber. Included in this study was development of a process for producing controlled submonolayer depositions of titanium dioxide.

The *in situ* analytical technique used was X-ray photoelectron spectroscopy (XPS). It is surface sensitive and typically provides elemental identification and chemical bonding information restricted to a few monolayers at the surface. The use of an UHV chamber provided a very clean environment for growth and analysis. Deposition and characterization were performed alternately which provided information with increasing film thickness. Few studies are conducted in which characterization takes place as the film is produced. *Ex situ* atomic force microscopy was conducted on thin films to produce a topographic image.

MOCVD from titanium isopropoxide is divided into two temperature regimes: deposition below and above the precursor pyrolysis temperature. The first part of the experimental work

determined the pyrolysis temperature, effects of dosing below and above the pyrolysis temperature, and effect of isothermal post-deposition annealing on depositions made below the pyrolysis temperature.

The pyrolysis temperature was determined by two methods. In one case, the substrate was dosed at a range of temperatures, and the depositions evaluated. In the second case, pyrolysis of precursor initially deposited on sapphire at low temperature was determined by post-deposition annealing. Decomposition was evaluated by monitoring the species on the surface. In most studies, decomposition of adsorbed molecules is determined by monitoring the desorbing by-products. Deposition below the pyrolysis temperature was evaluated as a function of dose time.

Although the main focus of this work was to investigate thin films, thick films were produced. They were *in situ* and *ex situ* characterized. A thick film was defined in this work to have a thickness such that the substrate was no longer detected by the *in situ* techniques. The *ex situ* techniques used were X-ray diffraction (XRD) and Rutherford backscattering spectroscopy (RBS). The thick films were used as comparisons to the thin films, to confirm the titanium isopropoxide precursor could produce stoichiometric films without a second oxygen source, and to determine the titanium dioxide structural phases formed as a function of temperature.

In the second part of the experimental work, the observations of the first part were applied to produce controlled submonolayer depositions. Stoichiometry and growth rate as a function of dose

temperature, annealing temperature, annealing time, and film thickness were investigated. Included in this section was a study of the effect of isothermal annealing at 700°C.

The last experimental part addressed the issues of interface reactions. XPS peak shapes and positions were evaluated as a function of increasing film thickness. Film thicknesses ranged from 0.1 to 2.7 nm. Evidence for reduction of the sapphire substrate by titanium dioxide and charge transfer at the interface was investigated. Observed XPS O $1s$ peak position shifts in thin films were compared with simulated peaks. Total shifts in thin and thick films were also compared.

1.3   Outline of dissertation

Chapter 2 provides relevant background information. In this chapter, different thin film formation techniques are discussed. The criteria for precursor selection for MOCVD are summarized. The chapter also includes a discussion of the applications and properties of titanium dioxide films.

Chapter 3 provides information regarding the materials relevant to this study. The physical constants and properties of the titanium isopropoxide precursor are given. The physical constants and crystallographic data for titanium dioxide and sapphire are provided. A summary of the reported epitaxial relationships between titanium dioxide and sapphire(0001) is provided.

Chapter 4 describes the UHV-MOCVD chamber. The *in situ* and

ex situ techniques utilized in this work are also described. The last sections of the chapter summarizes the procedures used for quantitative XPS analysis and error analysis.

Chapters 5, 6, and 7 describe and discuss the experimental observations. Chapter 5 explores depositions below and above the precursor pyrolysis temperature. The last two sections of this chapter evaluate the stoichiometry and titanium oxide phases in thick films.

Chapter 6 discusses the production of controlled submonolayer depositions. Included are the effects of annealing time and temperature. Chapter 7 discusses an investigation for evidence of interface reaction. Included in this chapter are evaluations of XPS peak shapes and binding energy positions with film thickness for thin films.

Chapter 8 summarizes the key experimental observations. Within this chapter are suggestions for future investigations. In Appendix 1, the flux emerging from the dosing tube is determined and compared to the chamber flux for a pressure of 1.0×10^{-8} Torr. A uniform overlayer model was used in Chapters 6 and 7 to determine film thickness from XPS photoelectron peak intensities. Appendix 2 evaluates the model by applying it to simulated films with island type growth. Appendix 3 describes the procedure for simulating the XPS O 1s peak position shift with increasing film thickness.

Chapter 2
Background

2.1   Introduction

Techniques for forming titanium oxide films are reviewed in
this chapter. Section 2.2 presents an overview of film formation
techniques. The chemical vapor deposition method is described in
greater detail in the next section. Included are descriptions of the types
of CVD, variety of activation reactions, and criteria for precursor
selection for metalorganic CVD. Section 2.4 reviews the methods by
which titanium dioxide films have been produced. Applications of
titanium dioxide films are also included. The last section describes three
thin film growth modes.

2.2   Film formation techniques

A film is generally taken to be the area near the surface which
possesses different properties than the bulk.[2.1-3] The film and bulk
compositions may be the same. Films are also referred to as overlayers
or coatings. A variety of techniques are available for forming films. They
include methods by which a film is deposited on a substrate or the
substrate itself is altered by mechanical or chemical methods to create a
film.

There are a number of definitions for classifying film formation

6

techniques. They may be grouped according to the environment the film is formed in (e.g., electrolysis, plasma), size of the reactants (e.g., atomistic, particulate), phase of the reactants (e.g., gas, liquid), or by physical versus chemical methods.[2.1-3] A particular film formation technique can fall into more than one category.

A classification by Scheugraf,[2.3] based on the reactant phase and physical versus chemical methods, divides techniques into four groups: evaporative (physical), glow-discharge (physical-chemical), liquid-phase (chemical), and gas-phase (chemical). Within the evaporative group are techniques such as molecular beam epitaxy and the various evaporation processes. Sputter, ion beam, and plasma techniques are classified as glow discharge methods. Electrolytic and sol-gel type spin on or spray on techniques fall within the liquid-phase group. The final group, gas-phase, includes chemical vapor deposition (CVD) and techniques which change the substrate by oxidation or nitridation.

Criteria for choosing a technique includes feasibility, possible damage to the substrate or film, the processing temperature, availability of reactants, type of by-products produced, reactor design, rate of film formation, need for additional post-deposition processing, and cost.[2.1,2]

2.3   Chemical vapor deposition

Chemical vapor deposition involves the deposition of solid material by the reaction of vaporous reactants close to or on the surface of a substrate or film.[2.1,3] The advantages of CVD include versatility,

suitability for a wide range of films, range of operating pressures, and uniform coverage since it is a non line of sight process. The disadvantages include the need to find suitable reactants, possible damage to the substrate due to the temperature or reactants used, need to remove possible toxic or corrosive by-products, and possible requirements for a special reactor design depending on the materials system.

CVD processes are applied for producing a variety of films, including elements, oxides, dielectrics, semiconductors, intermetallics, and silicides. CVD is used in several industries, i.e., solid state devices, semiconductor, and tool coatings.[2.2,3] The basic requirements of a reactor are provisions for handling or producing reactant gases and vapors, transport of the reactants to the substrate, producing the reaction to form the film, and exhaust of unspent reactants and by-products.[2.3]

2.3.1 Types

There are a number of film deposition processes which satisfy the basic definition of CVD, but differ in operating conditions. CVD processes may be classified according to the operating pressures, temperatures, type of precursors, type of reaction, or method of reaction activation.

CVD is performed in pressures ranging from atmospheric to low to ultrahigh vacuum, and are referred to as APCVD, LPCVD or

UHV-CVD, respectively. In terms of temperature, the two groups are known as low temperature (LTCVD) or high temperature (HTCVD) for processes below and above 500°C, respectively.[2.1] Precursors include gases, metalorganic compounds, and inorganic compounds. If a metalorganic reactant is used, the process is referred to as MOCVD. The reactions used include thermal decomposition (pyrolysis), hydrolysis, oxidation, reduction, and disproportionation.[2.1] The methods used to activate the reactants vary from thermal to plasma-enhanced (PECVD), photo-enhanced (PHCVD), laser-induced (LCVD), electron-enhanced, or ion-beam assisted (IBCVD).[2.1] The enhanced or assisted activated reactions typically occur at lower temperatures than pyrolysis. Spray pyrolysis is often considered as a CVD technique.[2.1] Films are formed by thermal decomposition of a spray of precursor in solution.

2.3.2 Heterogeneous and homogeneous reactions

CVD reactions may be of the heterogeneous or homogeneous type. Heterogeneous reactions take place on the substrate or film surface, whereas homogeneous reactions take place in the gas phase and the products diffuse to the substrate or growing surface.[2.1,4] Heterogeneous reactions are assumed to be catalyzed by the substrate or film surface.

CVD reactions are generally assumed to be heterogeneous, and according to Morosanu,[2.1] the reaction steps are "(1) transport of the reactant to the vicinity of the substrate; (2) diffusion of the reactants to

the substrate surface; (3) reactant adsorption on the substrate surface; (4) surface chemical reaction; (5) surface migration and lattice incorporation; (6) reaction product desorption; (7) diffusion of reaction products away from the substrate surface; and (8) transport of reaction products outside the deposition zone."

Homogeneous reactions are generally undesirable. Deposition of particles formed in the vapor tend to produce non-uniform films or powders. They are promoted by high concentrations, high temperatures, and small temperature differences between the reactant vapors and substrate.[2.1,4] Although CVD reactions are usually assumed to be heterogeneous, homogeneous reactions have been reported and may be crucial for materials systems where an intermediate must first form in the gas phase, then adsorb and react on the substrate surface.[2.2,5,6]

2.3.3 Metalorganic chemical vapor deposition

The precursors used in MOCVD are organic compounds. They may be metal alkyls (e.g., trimethyl gallium, $(CH_3)_3Ga$) or metal alkoxides (e.g., titanium isopropoxide, $Ti(C_3H_7)_4$). Metal alkyls are typically used in conjunction with hydrides to deposition III-V or II-VI compounds.[2.3] CVD reactions of metal alkoxides are used to form oxides. Alkoxides are represented as $M(OR)_x$ where M is the metal, R is an organic group, and x is the valence number.[2.7]

The alkoxide precursor selection criteria includes availability, purity, volatility, stability, and by-products produced. Volatility is a key

factor and is related to the tendency of the alkoxide to form oligomers. The degree of oligomer formation is characterized by n, the degree of polymerization (also referred to as the molecular complexity).[2.8] Oligomer formation reduces volatility and is affected by the R group structure and the metal.[2.7,8] Generally, the larger or bulkier the R group, the lower the tendency for formation. However, an R group that is too large produces a molecule with a high molecular weight, which can reduce volatility. The larger the metal atom, the lower the volatility because the R groups are less effective in preventing oligomer formation. Tabulations of volatilities and degrees of polymerization for various metal alkoxide families are available in the literature.[2.7,8]

Metal alkoxides can be used to form oxide films by thermal decomposition, hydrolysis or oxidation reactions, and with or without enhanced and assisted reactions, e.g., plasma.

2.4   Titanium dioxide film growth

Titanium dioxide has several properties making it a material of interest as a film. It has a high dielectric constant (180 parallel to the C-axis for rutile) stable to 300°C and gigacycle frequencies, high refractive index, is chemically inert in most environments, and provides good transmittance in the visible region.[2.5,9-14] Titanium dioxide has applications as antireflective coatings, dielectrics in integrated circuits, oxygen sensor, for MOS structures, solar energy conversion, and as a beam splitter for optical purposes.[2.5,6,13-20] Very thin films are useful for

ultra large scale integrated circuits, Josephson tunnel junctions, and high efficient optical filters.[2.20]

Titanium dioxide films have been formed by non-CVD and CVD methods. The physical non-CVD methods include evaporation (conventional, electron-beam, activated reactive), sputtering (ion-beam and RF diode), ion or plasma plating, molecular beam epitaxy, and oxidation of deposited titanium metal film.[2.21-25] These methods typically use titanium metal or titanium oxide reacted with oxygen. Use of titanium oxide as the evaporative source alone does not produce stoichiometric films.[2.21] Other non-CVD techniques used to produce titanium dioxide include dip and spin coating of colloidal solutions or sol gels.[2.26-29]

Titanium dioxide films have been produced by CVD from various precursors including titanium tetrachloride, titanium ethoxide, and titanium isopropoxide. Titanium tetrachloride was reacted with oxygen or water, or sprayed to produce the film.[2.9,10,14,15,20] Desu[2.20] produced the film by a method called successive layer-wise chemisorption in which titanium tetrachloride was alternately adsorbed on the substrate and then reacted with water to form the oxide. Depositions of 0.27 nm per cycle were produced. Titanium ethoxide was typically pyrolyzed or reacted with oxygen to form the oxide.[2.13,16,30,31]

Titanium isopropoxide is one of the more common precursors used. Among the titanium alkoxides, titanium isopropoxide has one of the highest volatilities.[2.7,8] It was used to form films by thermal decomposition, reaction with water or oxygen, and in a spray pyrolysis

system.[2.5,6,11-13,18-19,32-39] Use of water or oxygen are not necessary to form stoichiometric films. The presence of oxygen was observed to decrease the activation energy for reaction.[2.39] The thermal decomposition reaction for titanium isopropoxide has been reported as:[2.40]

$$Ti(OC_3H_7)_4 \rightarrow TiO_2 + 4CH_3 - CH = CH_2 + 2H_2O \qquad (2.1)$$

Films have been grown from titanium isopropoxide in pressures ranging from low to ultrahigh vacuum.

Thermal decomposition of titanium isopropoxide adsorbed on copper was studied by monitoring desorption products by temperature-programmed desorption (TPD).[2.5] Decomposition occurred at two temperatures, 177° and 347°C.

Studies of ultrahigh vacuum chemical vapor deposition of titanium oxide from the isopropoxide precursor have been reported for growth on silicon and characterization by XPS and AES,[2.12] and growth on strontium titanate and sapphire and characterization by AES and RHEED.[2.37,38] The study on silicon determined the stoichiometry of the film produced by pyrolysis of precursor to be TiO_2. The study on oxide substrates explored epitaxial relations between the substrate and film and the precursor decomposition reaction.

Studies of CVD titanium dioxide from titanium isopropoxide precursor have generally focused on characterization of thick films with thicknesses in the μm range. These studies determined the crystalline

phases formed, epitaxial relations, and properties as functions of processing conditions.

2.5   Thin film growth modes

There are three general types of thin film growth modes. They are known as Frank - van der Merwe, Stranski - Kranstanov, and Volmer - Weber growth.[2.41] The first mode is also known as layer - by - layer. In this mode, film growth is two dimensional. Growth proceeds as one monolayer at a time. In the Stranski - Kranstanov mode, the film first forms a monolayer in the substrate. Subsequent film growth is three dimensional and forms as islands on the initial monolayer. In the last mode, which is also known as islanding, the film grows as islands directly on the substrate. Knowledge of the film growth mode is of interest for many studies, including epitaxial investigations.

2.5   References for Chapter 2

2.1   C.E. Morosanu, *Thin Films by Chemical Vapor Deposition*; Ch. 1-3, and 5, pp. 19-90 and 101-16. Elsevier, Amsterdam, 1990.

2.2   R.F. Bunshah, J.M. Blocher, Jr., T.D. Bonifield, J.G. Fish, B.E. Jacobson, D.M. Mattox, G.E. McGuire, M. Schwartz, J.A. Thorton, and R.C. Tucker, Jr., *Deposition Techniques for Films and Coatings: Developments and Applications*; Ch. 1 and 8, pp. 1-18 and 335-62. Noyes Publications, Park Ridge, New Jersey, 1982.

2.3   *Handbook of Thin-Film Deposition Processes and Techniques: Principles, Methods, Equipment and Applications*; Ch. 1 and 7, pp. 1-25 and 234-69. Edited by K.K. Schuegraf. Noyes Publications, Park Ridge, New Jersey, 1988.

2.4   K.J. Sladek, "The Role of Homogeneous Reactions in Chemical Vapor Deposition," *J. Electrochem. Soc.*, **118** [4] 654-57 (1971).

2.5   K.L. Siefering and G.L. Griffin, "Kinetics of Low-Pressure Chemical Vapor Deposition of TiO_2 from Titanium Tetraisopropoxide," *J. Electrochem. Soc.*, **137** [3] 814-18 (1990).

2.6   K.L. Siefering and G.L. Griffin, "Growth Kinetics of CVD TiO_2: Influence of Carrier Gas," *J. Electrochem. Soc.*, **137** [4] 1206-1208 (1990).

2.7   D.C. Bradley, "Metal Alkoxides as Precursors for Electronic and Ceramic Materials," *Chem. Rev.*, **89**, 1317-22 (1989).

2.8   D.C. Bradley, R.C. Mehrotra, and D.P. Gaur, *Metal Alkoxides*; Ch. 3, pp. 42-147. Academic Press, London, 1978.

2.9   R.N. Ghostagore and A.J. Noreika, "Growth Characteristics of Rutile Film by Chemical Vapor Deposition," *J. Electrochem. Soc.*, **117** [10] 1310-14 (1970).

2.10   A. Turkovic, M. Ivanda, A. Drasner, V. Vranesa, and M. Persin, "Raman Spectroscopy of Thermally Annealed TiO_2 Thin Films," *Thin Solid Films*, **198**, 199-203 (1991).

2.11   T. Fuyuki and H. Matsunami, "Electronic Properties of the Interface Between Si and TiO_2 Deposited at Very Low Temperatures," *Jpn. J. Appl. Phys.*, **25** [9] 1288-91 (1986).

2.12   J.P. Lu and R. Raj, "Ultra-high Vacuum Chemical Vapor

Deposition and *In Situ* Characterization of Titanium Oxide Thin Films," *J. Mater. Res.*, **6** [9] 1913-18 (1991).

2.13   S.R. Kurtz and R.G. Gordon, "Chemical Vapor Deposition of Doped TiO_2 Thin Films," *Thin Solid Films*, **147**, 167-76 (1987).

2.14   A.E. Feuersanger, "Titanium-Dioxide Dielectric Films Prepared by Vapor Reaction," *Proceedings of the IEEE*, **52** [12] 1463-65 (1964).

2.15   S. Hayashi and T. Hirai, "Chemical Vapour Deposition of Rutile Films," *J. Crystal Growth*, **36**, 157-64 (1976).

2.16   Y. Takahashi, K. Tsuda and K. Sugiyama, "Chemical Vapour Deposition of TiO_2 Film Using an Organometallic Process and Its Photoelectrochemical Behavior," *J. Chem. Soc., Faraday Trans.*, **1** [77] 1051-57 (1981).

2.17   E.M. Logothetis and W.J. Kaiser, "TiO_2 Film Oxygen Sensors Made by Chemical Vapor Deposition From Organometallics," *Sensors and Actuators*, **4**, 333-40 (1983).

2.18   S. Sato, A. Sobczynski, J.M. White, A.J. Bard, A. Campion, M.A. Fox, T.E. Mallouk, and S.E. Webber, "Photochemical Properties of Ultrathin TiO_2 Films Prepared by Chemical Vapor Deposition," *J. Photochem. Photobio., A: Chem.*, **50**, 283-90 (1989).

2.19   M. Balog, M. Schieber, S. Patai, and M. Michman, "Thin Films of Metal Oxides on Silicon by Chemical Vapor Deposition with Organometallic Compounds. I," *J. Crystal Growth*, **17**, 298-301 (1972).

2.20   S.B. Desu, "Ultra-thin TiO_2 Film by a Novel Method," *Mater. Sci. Eng., B*, **13**, 299-303 (1992).

2.21   G. Hass, "Preparation, Properties and Optical Applications of Thin Films of Titanium Dioxide," *Vacuum*, **2** [4] 329-345 (1952).

2.22   J.M. Bennett, E. Pelletier, G. Albrand, J.P. Borgogno, B. Lazarides, C.K. Carniglia, R.A. Schmell, T.H. Allen, T. Tuttle-Hart, K.H. Guenther, and A. Saxer, "Comparison of the Properties of Titanium Dioxide Films Prepared by Various Techniques," *Applied Optics*, **28** [15] 3303-17 (1989).

2.23   L.S. Hsu and C.Y. She, "Real-Time Monitoring of Crystallization and Structural Transformation of Titania Films with Raman Spectroscopy," *Optics Letters*, **10** [12] 638-40 (1985).

2.24   M. Ghanashyam Krishna, K. Narasimha Rao, M. Adinarayana

Murthy, and S. Mohan, "Optical Properties of Activated Reactive Evaporated TiO_2 Films," *Mater. Sci. Eng., B*, **5**, 427-30 (1990).

2.25   K.B. Alexander, F.J. Walker, R.A. McKee, and F.A. List III, "TiO_x/Al_2O_3 Multilayer Ceramic Thin Films," *J. Am. Ceram. Soc.*, **73** [6] 1737-43 (1990).

2.26   P.A. Bertrand and P.D. Fleischauer, "Chemical Deposition of TiO_2 Layers on GaAs," *Thin Solid Films*, **103**, 167-75 (1983).

2.27   I.M. Thomas, "Single-Layer TiO_2 and Multilayer TiO_2-SiO_2 Optical Coatings Prepared From Colloidal Suspensions," *Applied Optics*, **26** [21] 4688-91 (1987).

2.28   J. Mugnier, B. Varrel, M. Bahtat, C. Bovier, and J. Serughetti, "Effect of Annealing Temperature on TiO_2 Monolayer Thin Films As Studied by Waveguide Raman Spectroscopy and Electron Microscopy," *J. Mater. Sci. Lett.*, **11**, 875-77 (1992).

2.29   G.J. Exarhos and N.J. Hess, "Spectroscopic Measurements of Stress Relaxation During Thermally Induced Crystallization of Amorphous Titania Films," *Thin Solid Films*, **220**, 254-60 (1992).

2.30   T.K. Won, S.G. Yoon, and H.G. Kim, "Compositional Analysis and Capacitance-Voltage Properties of TiO_2 Films by Low Pressure Metal-Organic Chemical Vapor Deposition," *J. Electrochem. Soc.*, **139** [11] 3284-88 (1992).

2.31   S. Sakurai, S. Watabe, and A. Morio, "A Capacitor of Titanium Dioxide Film Produced by Thermal Decomposition of Organic Titanium Compounds," *Rev. Elect. Comm. Lab.*, **11** [3-4] 178-91 (1963).

2.32   E.T. Fitzgibbons, K.J. Sladek, and W.H. Hartwig, "TiO_2 Film Properties as a Function of Processing Temperature," *J. Electrochem. Soc.*, **119** [6] 735-9 (1972).

2.33   H.J. Hovel, "TiO_2 Antireflection Coatings by a Low Temperature Spray Process," *J. Electrochem. Soc.*, **125** [6] 983-5 (1978).

2.34   Y. Takahashi, H. Suzuki, and M. Nasu, "Rutile Growth at the Surface of TiO_2 Films Deposited by Vapour-Phase Decomposition of Isopropyl Titanate," *J. Chem. Soc., Faraday Trans.*, **81**, 3177-25 (1985).

2.35   J.C. Parker, H.L.M. Chang, J.J. Xu, and D.J. Lam, "Characterization of MOCVD Grown Epitaxial Ceramic Oxide Thin Films," *Mater. Res. Soc. Symp. Proc.*, **167**, 337-41 (1990).

2.36   H.L.M. Chang, J.C. Parker, H. You, J.J. Xu, and D.J. Lam, "Preparation, Structure and Properties of VO_x and TiO_2 Thin Films by MOCVD," *Mater. Res. Soc. Symp. Proc.*, **168**, 343-49 (1990).

2.37   S. Chen, H.J. Gysling, G.R. Paz-Pujalt, T.N. Blanton, T. Castro, K.M. Chen, C.P. Fictorie, W.L. Gladfelter, A. Franciosi, P.I. Cohen, and J.F. Evans, "UHV-MOCVD Growth and *In Situ* Characterization of Epitaxial TiO_2 Films," *Mater. Res. Soc. Symp. Proc.*, **280**, 173-78 (1993).

2.38   S. Chen, M.G. Mason, H.J. Gysling, G.R. Paz-Pujalt, T.N. Blanton, T. Castro, K.M. Chen, C.P. Fictorie, W.L. Gladfelter, A. Franciosi, P.I. Cohen and J.F. Evans, "Ultrahigh Vacuum Metalorganic Chemical Vapor Deposition Growth and *In Situ* Characterization of Epitaxial TiO_2 Films," *J. Vac. Sci. Technol., A*, **11** [5] 2419-29 (1993).

2.39   M. Yokozawa, H. Iwasa, and Iwao Teramoto, "Vapor Deposition of TiO_2," *Jpn J. Appl. Phys.*, **7**, 96-97 (1968).

2.40   T. Kanai, H. Komiyama, and H. Inoue, "TiO_2 Particles by Chemical Vapor Deposition: Particle Formation Mechanism and Chemical Kinetics," *Kagatu Kogaku Ronbunshu*, **11**, 317-23 (1985).

2.41   L.C. Feldman and J.W. Mayer, *Fundamentals of Surface and Thin Film Analysis*; Ch. 6, pp. 25-153. North-Holland, New York, 1986.

Chapter 3
Relevant Materials

3.1   Introduction

Descriptions and physical constants of the titanium isopropoxide precursor, titanium dioxide (anatase and rutile structural phases), and sapphire(0001) are provided in Sections 3.2, 3.3 and 3.4, respectively. The structure and reconstruction of sapphire(0001) as a result of various treatments are described in Section 3.4. Crystallographic data for titanium dioxide and sapphire, and a summary of literature reports discussing epitaxial relationships between the two are also given in this chapter.

3.2   Titanium isopropoxide precursor

The factors to consider in choosing a chemical vapor deposition precursor include availability, ease of manufacture, purity, vapor pressure, stoichiometry of the resulting films, need for additional reactants, and decomposition by-products. Titanium oxide films can be produced by CVD from the reaction of titanium halides, and reaction or pyrolysis of titanium alkoxide.

Several titanium alkoxides can be used as precursors.They include titanium ethoxide, titanium isopropoxide and titanium t-butoxide. The isopropoxide form has the highest vapor pressure.[3.1] The

vapor pressure of titanium isopropoxide as a function of temperature is:[3.2]

$$\log_{10}(P_{eq}) = 9.837 - 3193.7/T \qquad (3.1)$$

where P_{eq} is in Torr and T in °K. At room temperature, 25°C, the vapor pressure is 0.13 Torr.

Most CVD processes use a carrier gas to assist in transporting the precursor vapor to the reaction zone. The deposition/analysis chamber used in this work does not utilize carrier gases. Precursor vapor is introduced directly into the chamber. Since the deposition chamber pressure is typically 1×10^{-8} Torr, titanium isopropoxide at room temperature has sufficient vapor pressure to deposit films.

The chemical formula of titanium isopropoxide is $Ti(OC_3H_7)_4$. Its chemical abstract number (CAS) is 546-68-9.[3.3] In the literature, this compound is referred to by various names, including $Ti(OPr^i)_4$, $Ti(O\text{-}i\text{-}Pr)_4$, tetra-isopropyl-titanate (TPT), and titanium tetraisopropoxide (TTIP).[3.2-6] The physical constants of titanium isopropoxide are summarized in Table 3.1.[3.3] Titanium isopropoxide is highly reactive with moisture and requires care in handling.

3.3   Titanium dioxide

Figure 3.1 shows the phase diagram for Ti-O.[3.7] The stoichiometry of interest in this work is TiO_2. It can form as three

Table 3.1. Physical Constants of Titanium Isopropoxide[3.3]

Physical Constant	Titanium Isopropoxide
Molecular weight, g/gmole	284.26
Specific gravity	0.955
Melting point,°C	18 - 20
Boiling point,°C	232
Appearance	white solid or colorless liquid
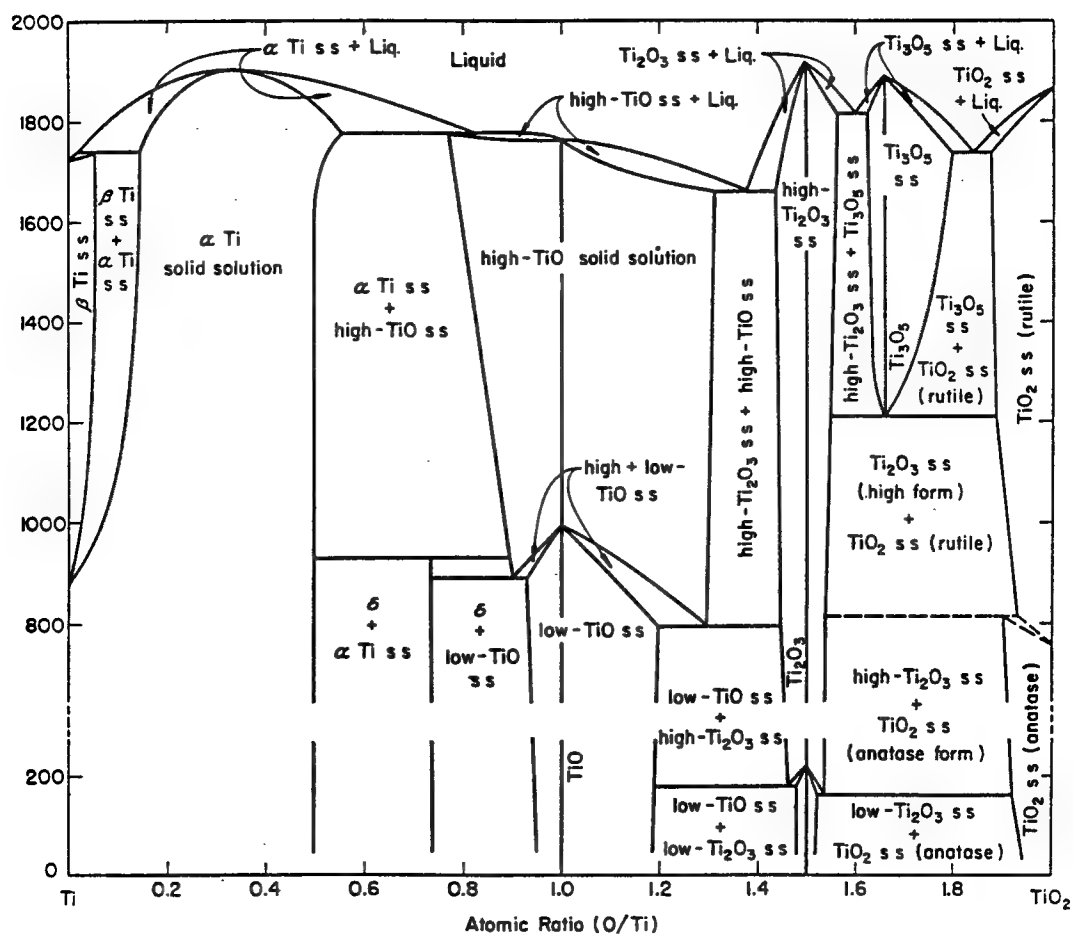
Figure 3.1. Phase diagram of the Ti - O system.[3.7]

structural phases, brookite, anatase and rutile.[3.8] For growth of TiO_2 by CVD, the phases typically investigated are anatase and rutile. According to the phase diagram, the transformation temperature between these two phases for bulk titanium dioxide is approximately 800°C. Physical constants and crystallographic data for these two phases are summarized in Tables 3.2[3.9] and 3.3,[10,11] respectively. The crystal system for both phases is tetragonal. Figures 3.2(a) and (b) show units cells of anatase and rutile, respectively. The band gap of rutile is 3 eV and in the literature, it has been referred to as a wide gap semiconductor and insulator.[3.6,12]

3.4   Sapphire

3.4.1   Structure

Single crystal aluminum oxide (sapphire), α-Al_2O_3, has a corundum crystal structure, trigonal crystal system, and is described in terms of a rhombohedral or hexagonal unit cell.[3.13-16] Physical constants and crystallographic data are given in Tables 3.4[3.9] and 3.5,[3.12,16] respectively. Sapphire is an insulator.

The sapphire structure has been reviewed in the literature.[3.13,16,17] It is simpler to visualize as a hexagonal structure. It consists of layers of aluminum ions and closed packed oxygen ions. The cations occupy octahedral interstitial sites between the anion layers. There is a one to one ratio of anions to interstitial sites. To achieve the

Table 3.2. Physical Constants of Anatase and Rutile[3.9]

| | Titanium Dioxide Phase | |
Physical Constants	Anatase	Rutile
Molecular weight, g/gmole	79.90	79.90
Density, g/cm^3	3.84	4.26
Melting Point, °C		1830 - 1850
Boiling point, °C		2500 - 3000

Table 3.3. Crystallographic Data for Anatase and Rutile[3.10,11]

Crystallographic Data	Titanium Dioxide Phase	
	Anatase	Rutile
System	tetragonal	tetragonal
Space Group	$I4_1/amd$ (141)	$P4_2/mnm$ (136)
Unit Cell Dimensions		
$a = b$	3.785	4.5937
c	9.514	2.9619
$\alpha = \beta = \gamma$	90°	90°
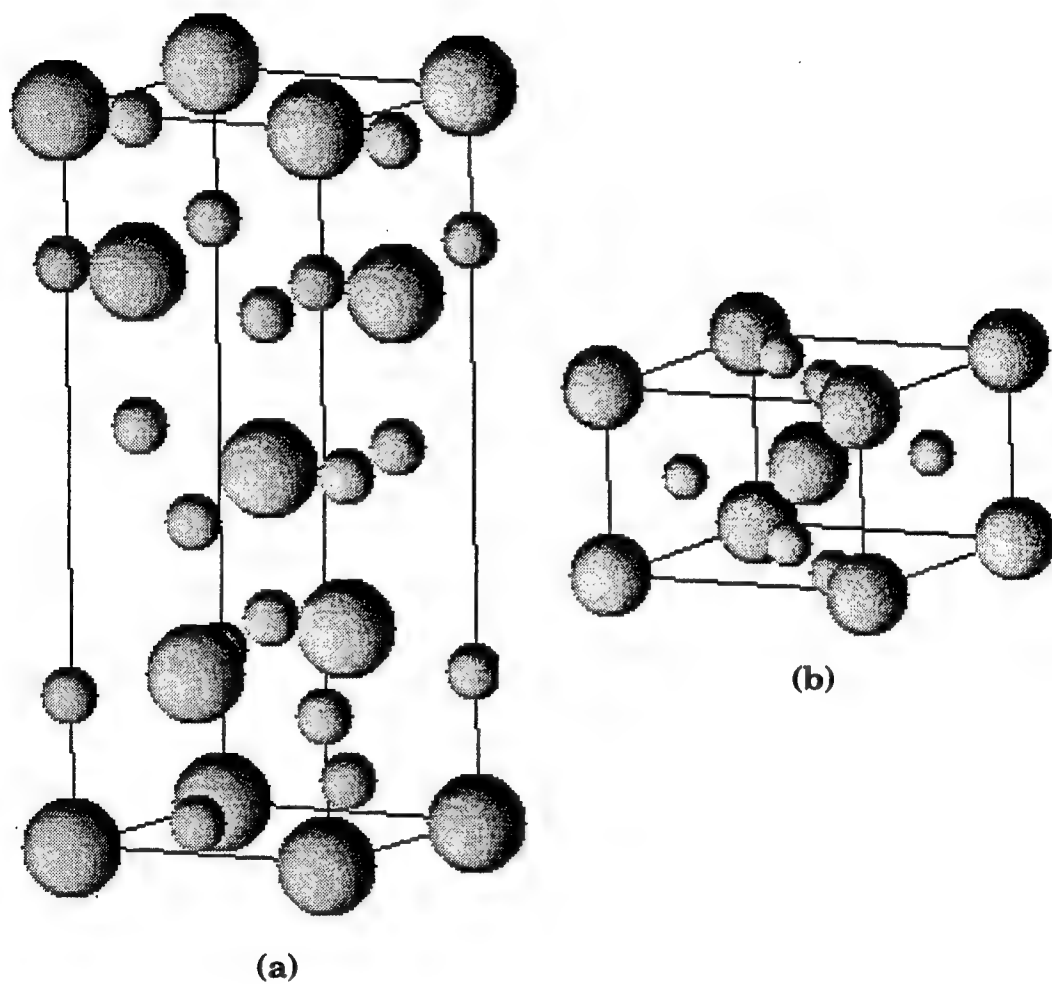
Figure 3.2. Units cells of the (a) anatase and (b) rutile phases of TiO_2. The large and small spheres represent the titanium and oxygen ions, respectively.

Table 3.4. Physical Constants of Sapphire[3.9]

Physical Constant	Sapphire
Molecular weight, g/gmole	101.96
Density, g/cm^3	3.97
Melting point, °C	2015 ± 15
Boiling point, °C	2980 ± 60

Table 3.5. Crystallographic Data for Sapphire[3.11,16]

Crystallographic Data	Unit Cell	
	Rhombohedral	Hexagonal
Unit Cell Dimensions		
a = b	5.12	4.75
c	5.12	12.97
$\alpha = \beta$	55.17°	90°
γ	55.17°	120°

correct stoichiometry for Al_2O_3, one third of the interstitial sites are unoccupied.

Figure 3.3[3.16] shows a schematic view of oxygen ion, aluminum ion, and interstitial positions in the (0001) plane, which is also referred to as the basal plane. Anions are represented by large empty circles, cations by small filled circles, and unoccupied interstitial sites by small empty circles. Every third site viewed along any row of cations is unoccupied. The figure also indicates lattice vectors relative to the unoccupied interstitial sites.[3.16]

The aluminum ions are not centered within their interstitial sites. They shift along the c-axis toward unoccupied sites either above or below them in the next cation layer.[3.16] The shifts decrease the distance between cations and unoccupied sites, and increase the distance between cations in successive layers. Within a cation layer, the aluminum ions are staggered up and down producing non-planar layers.

The cation positions may be distinguished as *A* (unoccupied), *B* or *C* sites. Interstitials in each cation layer are positioned above or below interstitials in the next cation layer. The arrangement of occupied and unoccupied sites within each layer is the same, but translated by one site along a row relative to the cation layer below it. The pattern of interstitial sites in successive layers is *A, B, C, A, B, C*, etc. This is also the pattern of cation layers. The pattern of anion layers in a hexagonal closed packed structure can be represented as *a, b, a, b*, etc. The resulting sapphire structure, as viewed along the c-axis, is a composite pattern of *a, A, b, B,*
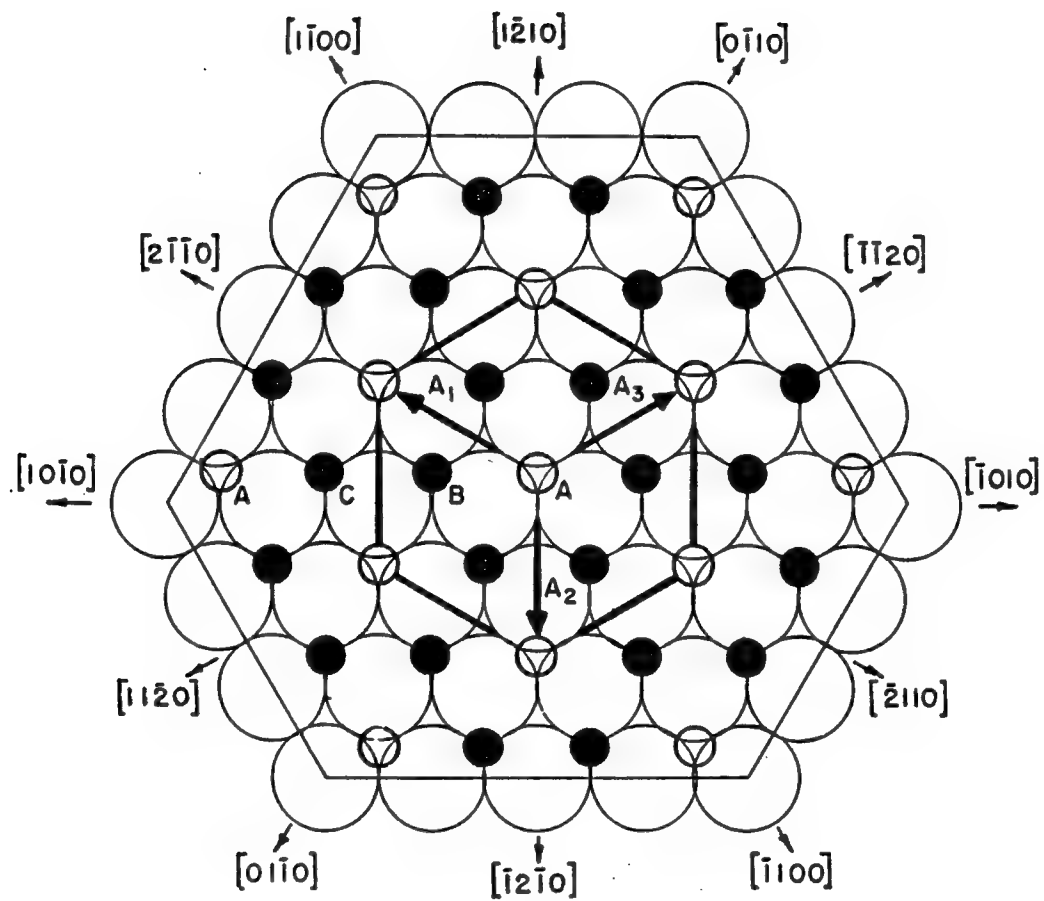
Figure 3.3. Schematic of sapphire(0001).[3.16] The large empty circles, small empty circles, and small filled circles represent oxygen ions, unfilled interstitial sites, and aluminum ions, respectively.

a, C, b, A, a, B, b, C layers. A hexagonal unit cell of sapphire is composed of six layers each of oxygen and aluminum ions.

3.4.2   Sapphire(0001) surface reconstruction

The sapphire(0001) surface structure has been reported to undergo transformations as the result of heating in vacuum or oxygen ambient, bombardment, or deposition of particular elements.[3.13,15,17-23] The surface structure was typically studied by low energy electron diffraction (LEED).

Sapphire(0001) should show a LEED (1 x 1) pattern which corresponds to a bulk-like structure of oxygen and aluminum ions at the surface. However, patterns corresponding to other surface structures, including a ($\sqrt{3}$ x $\sqrt{3}$) rotated 30°, (2 x 2), (3 $\sqrt{3}$ x 3 $\sqrt{3}$) rotated 30°, and ($\sqrt{31}$ x $\sqrt{31}$) rotated $\pm \tan^{-1}$ ($\sqrt{3}$/ 11) were observed after heating in vacuum.[3.17,19,22] Of these additional patterns, only the ($\sqrt{31}$ x $\sqrt{31}$) rotated $\pm \tan^{-1}$($\sqrt{3}$/ 11) (hereafter referred to as ($\sqrt{31}$ x $\sqrt{31}$)) was consistently produced from the (1 x 1) pattern and vice versa. Since the other patterns did not always appear and were not consistently reproducible with even the same sample, it was suggested they may be due to surface impurities.[3.19]

The (1 x 1) surface was shown to reconstruct to form the ($\sqrt{31}$ x $\sqrt{31}$) surface structure by several treatments. They include heating the sapphire in vacuum above ~1250°C, depositing aluminum above 800°C, and heating above 900°C after silicon deposition.[3.17,20] The (1 x 1) surface

is reproduced from the ($\sqrt{31}$ x $\sqrt{31}$) surface by annealing from 1000°-1200°C in oxygen at pressures of at least 10^{-4} Torr, annealing below 900°C after silicon deposition, and electron bombardment above 700°, but not 1000°C.[3.17,19,20]

AES analysis of the (1 x 1) and ($\sqrt{31}$ x $\sqrt{31}$) surfaces showed a lower quantity of oxygen present in the latter structure.[3.15] This analysis and the techniques applied to achieve either structure indicated the ($\sqrt{31}$ x $\sqrt{31}$) structure is oxygen deficient compared to the bulk-like (1 x 1) surface structure. It was proposed the ($\sqrt{31}$ x $\sqrt{31}$) structure is composed of a cubic overlayer on the bulk structure.[3.17] Identification of the sapphire surface structure should be conducted prior to film growth. In a study of copper on sapphire, the substrate surface structure was reported to influence the deposition.[3.23]

3.5   Titanium dioxide and sapphire(0001) system

Figure 3.4 shows the phase diagram for the TiO_2-Al_2O_3[3.24] system. Below approximately 1150°C, TiO_2 and Al_2O_3 coexist as two phases. Above this temperature, a new phase, Al_2TiO_5, forms from 50% TiO_2 and Al_2O_3.

The epitaxial relationships between TiO_2 and sapphire(0001) have been studied for overlayer growth by CVD of titanium isopropoxide and titanium tetrachloride, and molecular beam epitaxy (MBE) techniques.[3.5,25-31] Deposition of the film by oxidation or simply pyrolysis of titanium isopropoxide at 400°C and lower produces only anatase or
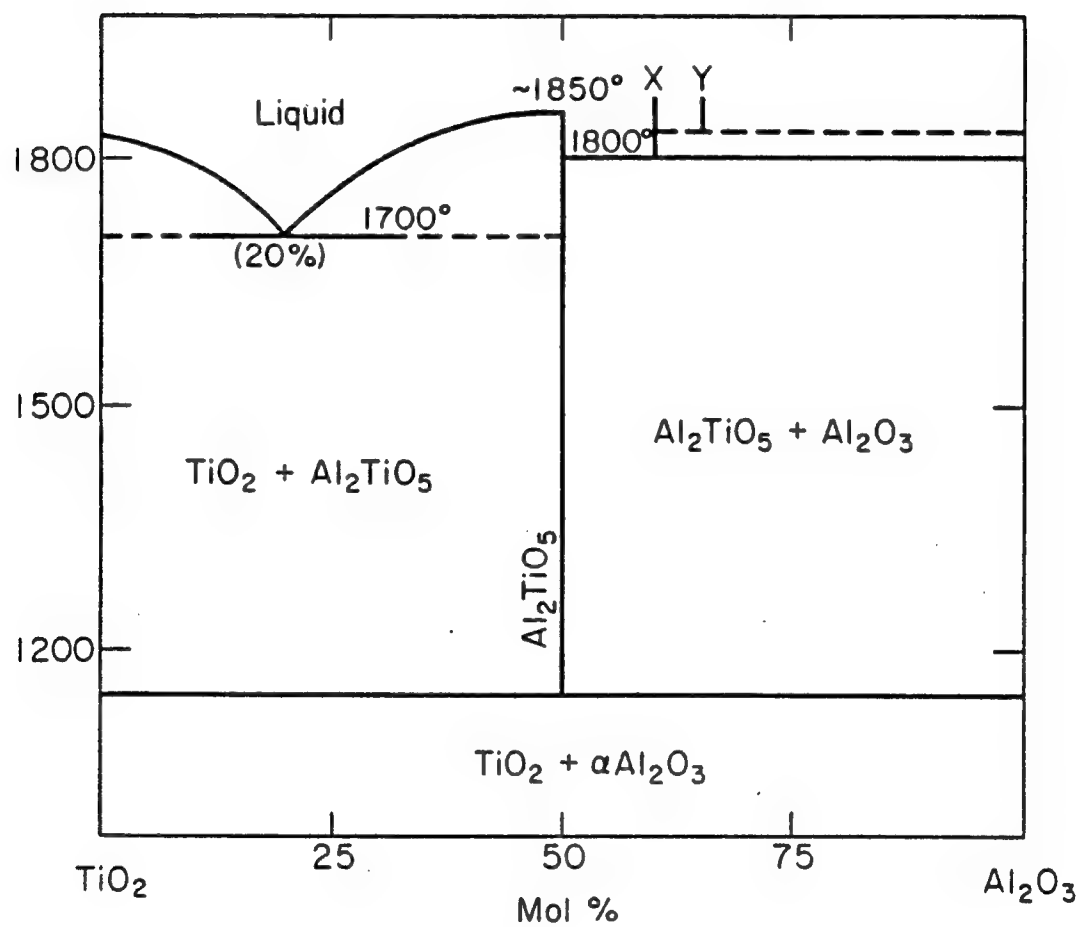
Figure 3.4. Phase diagram of the TiO_2 - Al_2O_3 system.[3.24]

predominately the anatase structural phase, with the other phase being rutile.[3.5,25-29] The orientation relationship between anatase and sapphire(0001) is:[3.5,25-29]

$$(112)\left[1\,\overline{0}\,1\right]_{\text{Anatase}} \parallel (0001)\left[\overline{1}\,100\right]_{\text{Sapphire}} \qquad (3.2)$$

Deposition of film by pyrolysis of titanium isopropoxide at 800°C, reaction of titanium tetrachloride and oxygen at 827°-932°C, and MBE technique produced only the rutile phase with the following orientation:[3.5,30,31]

$$(100)\left[001\right]_{\text{Rutile}} \parallel (0001)\left[10\,\overline{1}\,0\right]_{\text{Sapphire}} \qquad (3.3)$$

The lattice strains in the $[001]_{\text{rutile}}$ and $[010]_{\text{rutile}}$ directions are +8.03% and -3.59%, respectively.[3.5] Epitaxial rutile on sapphire(0001) has been characterized by RHEED and XRD.[3.5,31] The XRD rutile {110} pole figure and RHEED patterns both indicated the film grew as three variants oriented 120° from each other and the orientations consisted of rutile [001], [0-11], and [011] lining up with the sapphire [10-10].[3.5,31]

3.6   References for Chapter 3

3.1   D.C. Bradley, "Metal Alkoxides as Precursors for Electronic and Ceramic Materials," *Chem. Rev.*, **89**, 1317-22 (1989).

3.2   K.L. Siefering and G.L. Griffin, "Growth Kinetics of CVD TiO_2: Influence of Carrier Gas," *J. Electrochem. Soc.*, **137** [4] 1206-1208 (1990).

3.3   Aldrich Chemical Company, *Materials Safety Data Sheet: Titanium(IV) Isopropoxide, 97%*. Milwaukee, Wisconsin, 1992.

3.4   J.P. Lu and R. Raj, "Ultra-high Vacuum Chemical Vapor Deposition and In Situ Characterization of Titanium Oxide Thin Films," *J. Mater. Res.* **6** [9] 1913-18 (1991).

3.5   S. Chen, M.G. Mason, H.J. Gysling, G.R. Paz-Pujalt, T.N. Blanton, T. Castro, K.M. Chen, C.P. Fictorie, W.L. Gladfelter, A. Franciosi, P.I. Cohen, and J.F. Evans, "Ultrahigh Vacuum Metalorganic Chemical Vapor Deposition Growth and *In-Situ* Characterization of Epitaxial TiO_2 Films," *J. Vac. Sci. Technol. A*, **11** [5] 2419-29 (1993).

3.6   T. Fuyuki, T. Kobayashi, and H. Matsunami, "Effects of Small Amount of Water on Physical and Electrical Properties of TiO_2 Films Deposited by CVD Method," *J. Electrochem. Soc.*, **135** [1] 248-50 (1988).

3.7   E.M. Levin, C.R. Robbins, and H.F. McMurdie, *Phase Diagrams for Ceramists*; Fig. 22. The American Ceramics Society, Inc., Columbus, Ohio, 1964.

3.8   F.A. Grant, "Properties of Rutile (Titanium Dioxide)," *Rev. Mod. Phys.*, **31** [3] 646-74 (1959).

3.9   *CRC Handbook of Chemistry and Physics*, 64th Edition; pp. B-151-152. Edited by R.C. Weast, M.J. Astle, and W.H. Beyer. CRC Press, Inc.,Boca Raton, Florida, 1983.

3.10   W.B. Pearson, *A Handbook of Lattice Spacings and Structures of Metals and Alloys*. Pergamon Press, New York, 1958.

3.11   P. Villars and L.D. Calvert, *Pearson's Handbook of Crystallographic Data for Intermetallic Phases*, Vol. 1 and 3. American Society for Metals, Metals Park, Oh, 1985.

3.12   S. Munnix and M. Schmeits, "Electronic Structure of Ideal

TiO$_2$(110), TiO$_2$(001), and TiO$_2$(100) Surfaces," *Phys. Rev. B.*, **30** [4] 2202-11 (1984).

3.13   P.S.P. Wei and A.W. Smith, "Structure of the (0001) Surface of α-Alumina," *J. Vac. Sci. Technol.*, **9** [4] 1209-13 (1972).

3.14   J. Guo, H.L.M. Chang, and D.J. Lam, "Substrate Surface Step Effects on Microstructure of Epitaxial Films," *Appl. Phys. Lett.*, **61** [26] 3116-17 (1992).

3.15   C.C. Chang, "Silicon-on-Sapphire Epitaxy by Vacuum Sublimation: LEED-Auger Studies and Electronic Properties of the Films," *J. Vac. Sci. Technol.*, **8** [3] 500-11 (1971).

3.16   M.L. Kronberg, "Plastic Deformation of Single Crystals of Sapphire: Basal Slip and Twinning," *Acta Met.*, **5**, 507-24 (1956).

3.17   T.M. French and G.A. Somorjai, "Composition and Structure of the (0001) Face of α-Alumina by Low-Energy Electron Diffraction," *J. Phys. Chem.*, **74** [12] 2489-95 (1970).

3.18   J.M. Charig, "Low-energy Electron Diffraction of α-Alumina," *Appl. Phys. Lett.*, **10** [5] 139-40 (1967).

3.19   C.C. Chang, "LEED Studies of the (0001) Face of α-Alumina," *J. Appl. Phys.*, **39** [12] 5570-73 (1968).

3.20   J.M. Charig and D.K. Skinner, "The (0001) Surface of α-Alumina - LEED Observations,"; pp. 34 in *Proceedings of the Conference on the Structure and Chemistry of Solid Surfaces*. Edited by G.A. Somorjai. John Wiley & Sons, New York, 1969.

3.21   S. Baik, D.E. Fowler, J.M. Blakely, and R. Raj, "Segregation of Mg to the (0001) Surface of Doped Sapphire," *J. Am. Ceram. Soc.*, **68** [5] 281-86 (1985).

3.22   L. Pham Vam, M. Gautier, J.P. Durand, F. Gillet, and F. Jollet, "An XPS, EELS and LEED Study of Monocrystalline Al$_2$O$_3$(0001) Surface: Modifications by Heat Treatment of Ion Bombardment," *Surf. Int. Anal.*, **16**, 214-15 (1990).

3.23   M. Gautier, J.P. Durand, and L. Pham Van, "Influence of the Al$_2$O$_3$(0001) Surface Reconstruction in the Cu/Al$_2$O$_3$ Interface," *Surf. Sci. Lett.*, **249**, L237-32 (1991).

3.24   E. M. Levin and H. F. McMurdie, *Phase Diagram for Ceramists, 1975 Supplement*; Fig. 4376. The American Ceramic Society, Inc., Columbus, Ohio, 1975.

3.25   J.C. Parker, H.L.M. Chang, J.J. Xu, and D.J. Lam,
         "Characterization of MOCVD Grown Epitaxial Ceramic Oxide
         Thin Films," *Mater. Res. Soc. Symp. Proc.*, **167**, 337-41 (1990).

3.26   H.L.M. Chang, J.C. Parker, H. You, J.J. Xu, and D.J. Lam,
         "Preparation, Structure and Properties of VO_x and TiO_2 Thin
         Films by MOCVD," *Mater. Res. Soc. Symp. Proc.*, **168**, 343-49
         (1990).

3.27   H.L.M. Chang, H. You, J. Guo, and D.J. Lam, "Epitaxial TiO_2
         and VO_2 Films Prepared by MOCVD," *Appl. Surf. Sci.*, **48/49**,
         12-18 (1991).

3.28   H.L.M. Chang, Y. Gao, J. Guo, C.M. Foster, H. You, T.J.
         Zhang, and D.J. Lam, "Heteroepitaxial Growth of TiO_2, VO_2,
         and TiO_2/VO_2 Multilayers by MOCVD," *J. Phys. IV*, **1**, C2-953-60
         (1991).

3.29   J. Guo, H.L.M. Chang, H. Zhang, and D.J. Lam, "Substrate
         Surface Structure Effects on Microstructure of Epitaxial Films,"
         Mater. Res. Soc. Symp. Proc., **280**, 337-40 (1993).

3.30   R.N. Ghostagore and A.J. Noreika, "Growth Characteristics of
         Rutile Film by Chemical Vapor Deposition," *J. Electrochem.
         Soc.*, **117** [10] 1310-14 (1970).

3.31   K.B. Alexander, F.J. Walker, R.A. McKee, and F.A. List III,
         "TiO_x/Al_2O_3 Multilayer Ceramic Thin Films," *J. Am. Ceram.
         Soc.*, **73** [6] 1737-43 (1990).

Chapter 4
Experimental Techniques and Equipment

4.1   Introduction

The ultrahigh vacuum metalorganic chemical vapor deposition (UHV-MOCVD) chamber, *in situ* and *ex situ* analytical techniques, XPS data analysis, and error analysis are reviewed in this chapter. Section 4.2 describes the arrangement of the chamber. Descriptions of the dosing system and sample heating configuration are included in this section. The following section summarizes the three *in situ* surface analytical techniques available on the chamber. Section 4.4 describes the *ex situ* analytical techniques used in this work. The chapter concludes with a review of the procedures used in XPS data and error analysis.

4.2   UHV-MOCVD deposition and *in situ* analysis chamber

The benefits of an UHV growth and analysis chamber include the ability to *in situ* clean substrates prior to film growth, a clean environment in which to deposit films, *in situ* characterization which eliminates the possibility of surface contamination present with *ex situ* characterization, and the ability to use surface sensitive spectroscopic techniques which require vacuum systems for operation.[4.1,2]

The chamber used was a Perkin Elmer stainless steel

chamber. Figure 4.1 shows a schematic overhead view of the chamber. In a typical experiment, the sample mounted on the manipulator is alternately rotated to face the vapor doser for film growth or any of the various analytical techniques. The typical base pressure was 1×10^{-10} Torr. Chamber pressures were measured with an ionization gauge (Varian type UHV-24).

The chamber was pumped by a 300 l/s ion pump as the main pump, a 60 l/s turbomolecular secondary pump, and a titanium sublimator. The turbomolecular pump was used to pump the chamber following venting to atmosphere and to pump argon gas after sputtering. The chamber also has an liquid nitrogen cryopanel which can be used for additional pumping.

The *in situ* analytical techniques include X-ray photoelectron spectroscopy (XPS), Auger electron spectroscopy (AES), and low energy electron diffraction (LEED). The chamber was also equipped with a quadrupole mass spectrometer and a ion sputter gun system for cleaning purposes.

The sample was removed by venting the chamber to atmosphere. After sample replacement, the entire chamber was typically baked-out by heating to an elevated temperature over a two day period in order to reach UHV conditions. During this procedure, the outgassing rate from the walls was increased, resulting in a lower chamber pressure after cooling.[4.2,3]

The precursor vapor is introduced for deposition at the vapor doser which consists of a leak valve connected to a 3/8 inch tube
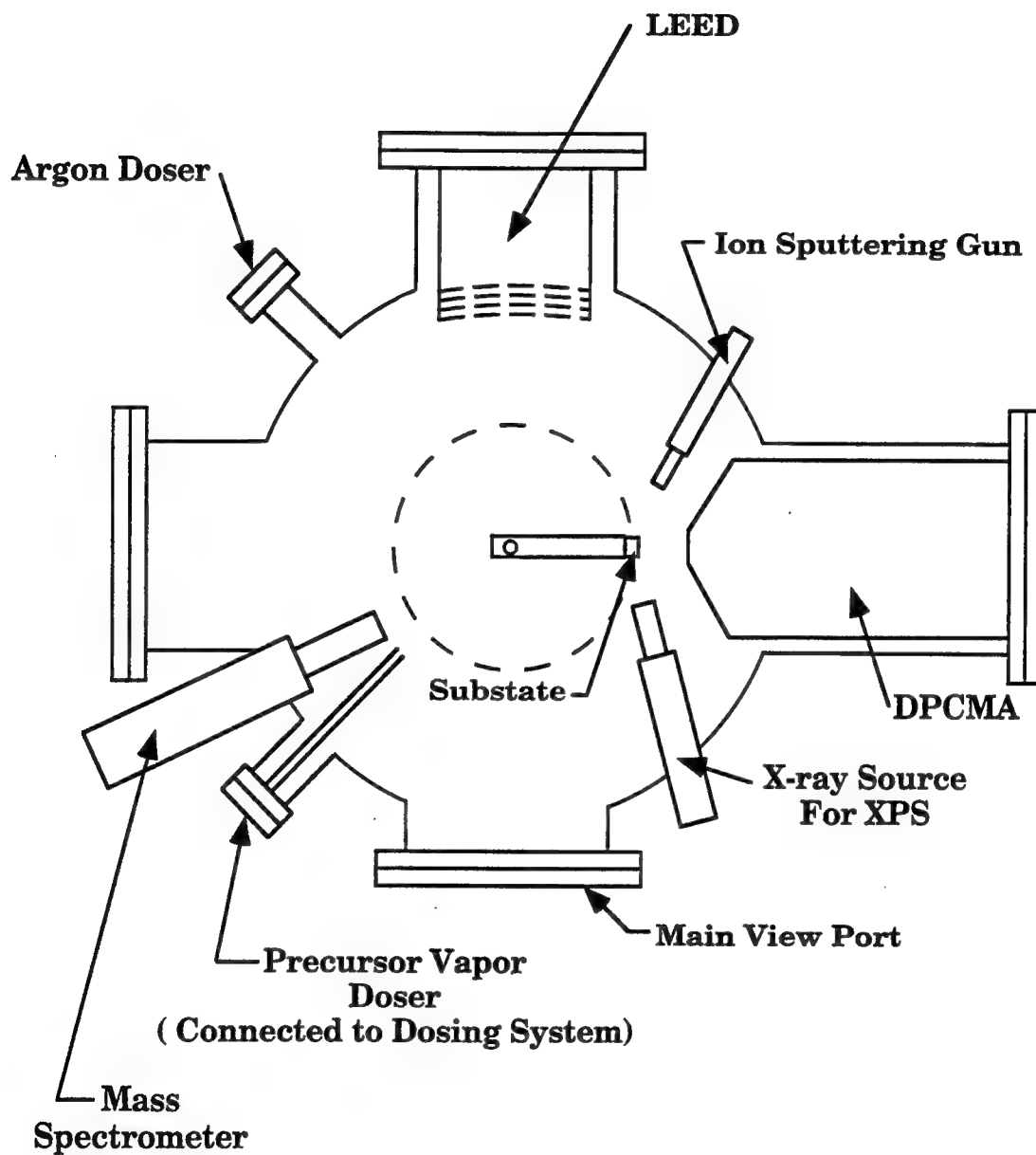
Figure 4.1. Schematic overhead view of the UHV-MOCVD chamber.

extending into the chamber. The sample is rotated to face the tube during deposition. An alternate method for depositing films involves filling the entire chamber with precursor vapor. The application of a dosing tube reduces or eliminates the potential for "(1) wall effects where impurities are displaced from the walls; (ii) gas interactions with hot filaments; and (iii) regurgitation effects in the ion pump."[4.4] Since CVD often utilizes reactant thermal decomposition to form films, precursor vapor reaction with hot filaments in the chamber is highly undesirable. The flux (molecules/m^2 sec) emerging from the dosing tube will be higher relative to the chamber.[4.4] In Appendix 1, the dosing tube flux is determined from experimental data and compared to the flux in the chamber for a chamber pressure of 1.0×10^{-8} Torr.

4.2.1   Dosing system

Figure 4.2 gives a schematic of the dosing system. It was attached to the main chamber at the vapor doser. The dosing system is composed of a main line connected through valves to vials. The valves permit vials to be filled with precursor in the inert atmosphere of a glove box and transported to the dosing line without exposing the contents to moisture or oxygen in the air. The vials were made of either stainless steel or Pyrex.

The dose line was connected on one end to a 60 l/s turbomolecular pump. The line is pumped before filling with precursor vapor. The turbomolecular pump is also used for precursor purification

42
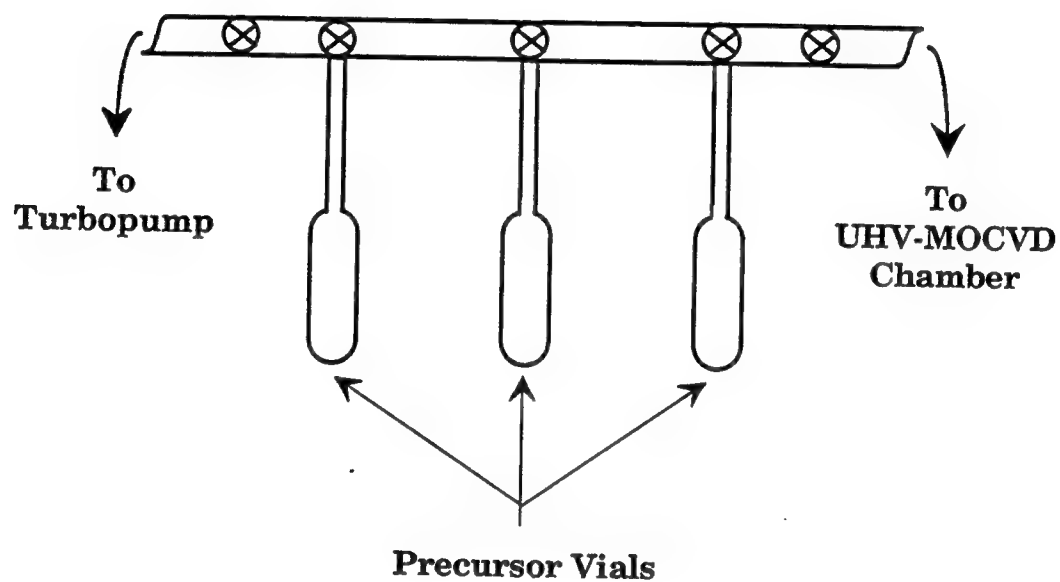
Figure 4.2. Schematic of the dosing system. It is connected to the UHV-MOCVD chamber at the vapor doser.

in H_2O freeze and thaw cycles. Precursors can be used at room temperature or heated.[4.5]

4.2.2 Manipulator and sample heating

The chamber manipulator provides X-Y-Z translations and rotation about the Z axis. Schematics of front and top views of the sapphire sample configuration are given in Figures 4.3(a) and (b), respectively. The sample heater was spot welded to tantalum supports on the manipulator.

The sample was mounted in a sandwich design which consisted of the sapphire to be deposited on, tantalum foil, and a piece of insulator the same size as the sapphire. The sandwich was held together by tantalum wire. The tantalum foil served as the heater by resistive heating with a d.c. power supply. The insulator component ensured the tantalum wires were not in electrical contact with the heater.

The tantalum heater was 0.001 inches thick. The tantalum wire was 0.01 inches in diameter. The insulator in the sandwich was either single or polycrystalline alumina. The sapphire substrate was backcoated with tantalum film. The insulator piece was also backcoated with tantalum film if single crystal alumina was used.

Sapphire is a difficult substrate to heat. Deposition of metallic films, such as tantalum, tungsten, titanium, tantalum nitride, or platinum on the back surface to assist in heating has been reported.[4.6-10] In a similar sandwich design, the metallic film has been used as the
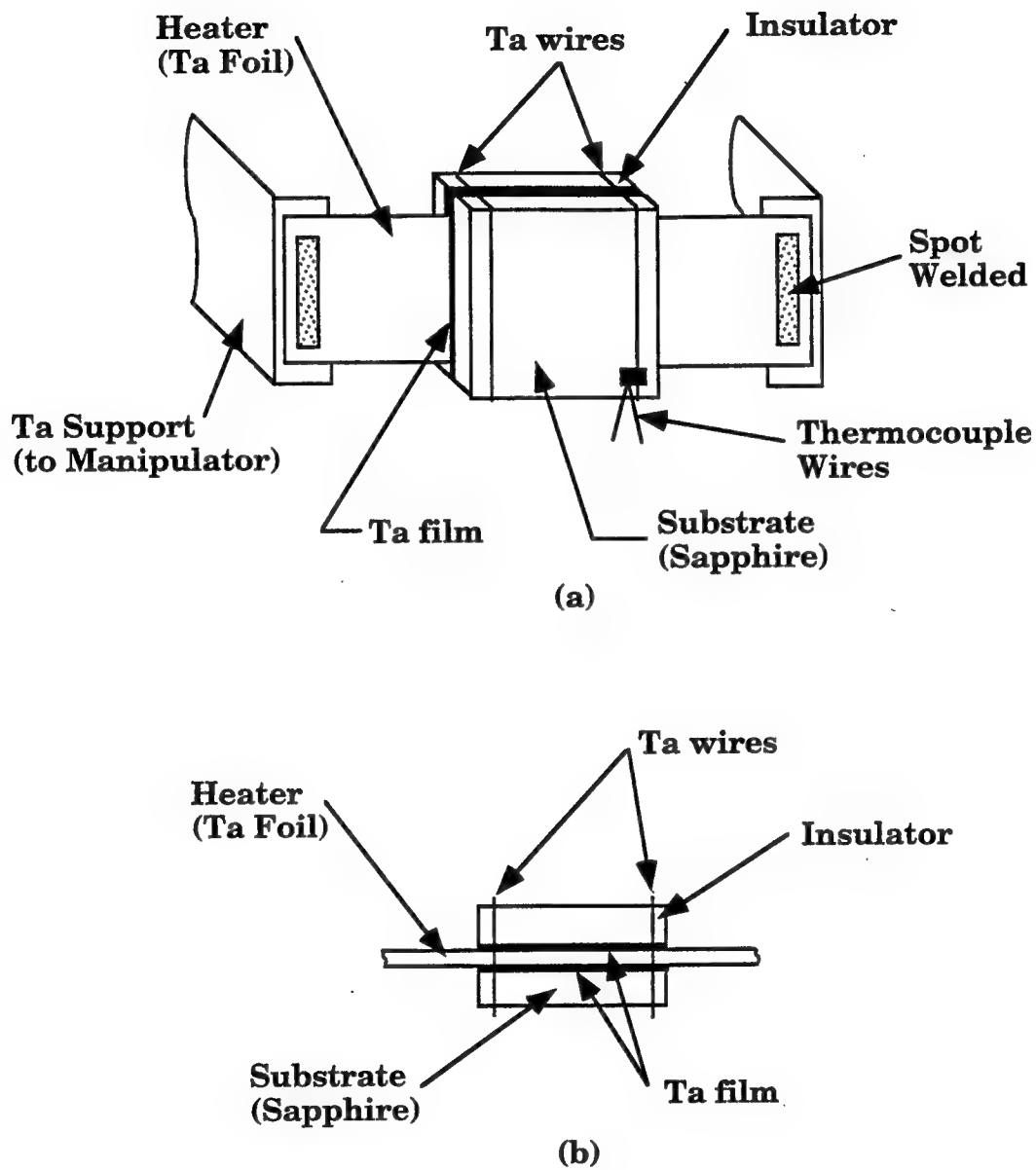
Figure 4.3. Schematics of the sapphire mounting configuration: (a) front view and (b) top view.

heater itself by resistive heating.[4.10] In this work, the tantalum film deposited on the back surface of the sapphire substrate acted as a heat susceptor.

The sapphire temperature was monitored by a K-type, chromel-alumel thermocouple. The thermocouple was spot welded to a small piece of tantalum foil and clamped under one of the tantalum wires holding the sample sandwich together. The thermocouple was in contact with the sapphire face. In another design, it was clamped in place using a small piece of Macor with a hole drilled through it. The hole was threaded through by one of the tantalum wires.

4.2.3   Ion sputtering gun

The ion sputtering gun (Perkin Elmer model 04-16) was used to produce argon ions. Substrate surfaces were cleaned prior to film deposition by Ar+ bombardment. The procedure involved setting the ion pump on stand-by, backfilling with argon gas (Matheson research purity), and then sputtering. After sputtering, the argon was initially pumped by the turbomolecular pump before switching to the ion pump.

4.2.4   Mass spectrometer

The quadrupole mass spectrometer was from Inficon, model Quadrex 200. It is capable of collecting species to a maximum 200 amu. The spectrometer was used to determine the composition of residue

gases after the bake-out procedure, and to detect the presence and location of any chamber leaks. It may also be used to evaluate the composition of precursor vapors introduced to the chamber and CVD decomposition products.

4.2.5   Low energy electron flood gun

The low energy electron flood gun was obtained from VG Microtech Limited, model LEG51. The flood gun was used in conjunction with XPS to compensate for charging which occurs with insulator materials.[4.11] A discussion of the charging phenomenon is presented in Section 4.3.2.

4.3   *In situ* characterization techniques

The three *in situ* characterization techniques available are Auger electron spectroscopy (AES), X-ray photoelectron spectroscopy (XPS), and low energy electron diffraction (LEED). XPS is also known as electron spectroscopy for chemical analysis (ESCA). In these techniques, a beam of electrons or photons are directed at the sample and the resulting emitted electrons collected. These techniques are surface analytical techniques. The information provided are restricted to the first few atomic layers at the surface of the material probed.[4.2,12] The surface sensitivity arises from the limited mean free path of the emitted electrons. Electrons with energies ranging from 10 to 500 eV have mean

free paths ranging from 4 to 20 Å, which are approximately a few atomic layers.[4.13]

Surface analytical techniques require vacuum systems for optimum operation. The presence of even a monolayer of carbon or other adsorbed impurity reduces their sensitivities to the surface of interest. Since one monolayer of gas is generally adsorbed in approximately one sec at 1 x 10^{-6} Torr, a pressure of 10^{-10} Torr is needed to minimize adsorption of impurity gases.[4.14] The emitted electrons can be scattered by gas molecules between the sample and analyzer. A vacuum of 10^{-5} to 10^{-6} Torr or better is generally needed to minimize such scattering.[4.2]

AES and XPS are complementary techniques. Both provide elemental identification with sensitivity of 0.1 -1 atomic%.[4.15] AES and XPS can provide information regarding the chemical environment. XPS has higher sensitivity to the chemical environment. AES has better spatial resolution and quicker data collection speed. It can produce damage to the sample analyzed.[4.15] LEED provides surface structural information.

A thorough review of AES and XPS was presented in a book edited by Briggs and Seah.[4.16] A thorough review of LEED was presented by Ertl and Küppers.[4.17]

4.3.1 Auger electron spectroscopy (AES)

In AES, atoms in a sample bombarded by a beam of electrons are ionized by losing electrons from core electron levels with energy E_K.

Another electron from a lower energy level, E_{L_1}, fills the created hole and the excess energy is released either with another emitted electron from a outer level, $E_{L_{2,3}}^*$, or as a X-ray photon (known as X-ray fluorescence). The second emitted electron is known as the Auger electron and its kinetic energy is given by the following equation:[4.18]

$$E_{KL_1L_{2,3}} = E_K - E_{L_1} - E_{L_{2,3}}^* \tag{4.1}$$

where $E_{L_{2,3}}^*$ represents an energy level in which an electron has already been removed.

The spectra are typically shown as a differential of the number of electrons collected, $E\mathrm{d}N(E)/\mathrm{d}E$, with kinetic energy (eV). AES spectra are unique for each element and consists of peaks located at specific energy positions (the position is traditionally defined as the high energy peak). Elements present at the surface are identified by comparing experimental and complied reference spectra.[4.19]

In this work, AES analysis was acquired with a double pass cylinder mirror analyzer (DPCMA) equipped with a coaxial electron gun for beam generation (Perkin Elmer model PHI 15-255G). It was typically used to check surface cleanliness. The direct data was collected with a V-f preamplifier (Perkin Elmer 96A) and the differentiation accomplished by a Savisky-Golay algorithm. An AST Premium 286 computer was used for data collection in conjunction with a Perkin Elmer 137 PC interface.[4.20]

4.3.2   X-ray photoelectron spectroscopy (XPS)

In XPS, the sample surface is irradiated with X-rays. Electrons are emitted by the photoelectric effect, with kinetic energy, E, given by the following equation:[4.21]

$$E = h\upsilon - E_{BE} - \phi_s \qquad\qquad (4.2)$$

where $h\upsilon$ is the photon energy, E_{BE} is the electron binding energy (eV), and ϕ_s is the spectrometer work function. XPS spectra are typically shown as intensity against decreasing binding energy or increasing kinetic energy. The spectra consists of peaks corresponding to the photoelectrons emitted. Auger peaks are also observed in XPS spectra.

Comparison of XPS experimental and handbook spectra[4.21] provides a determination of the elements present at the surface. XPS is also sensitive to the chemical environment of surface species which is reflected in photoelectron peak position shifts. A comparison of experimental and tabulated peak positions[4.21] provides chemical environment information.

The X-ray sources used typically produce Mg Kα (1253.6 eV energy, 0.7 eV FWHM) or Al Kα (1486.6 eV energy, 0.85 eV FWHM).[4.14] In addition to the major Kα, there are X-rays of lower intensities and higher kinetic energies present which produce peaks, called satellites, in the spectra. Table 4.1 shows the satellite positions and intensities for magnesium and aluminum anodes.[4.21] A monochromatized X-ray

Table 4.1. Satellites for Magnesium and Aluminum XPS Anodes[4.20]

Satellite	XPS Anode			
	Magnesium		Aluminum	
	Position relative to $\alpha_{1,2}$ (eV)	Height Relative to $\alpha_{1,2}$	Position relative to $\alpha_{1,2}$ (eV)	Height Relative to $\alpha_{1,2}$
$\alpha_{1,2}$	0	100	0	100
α_3	8.4	8.0	9.8	6.4
α_4	10.1	4.1	11.8	3.2
α_5	17.6	0.6	20.1	0.4
α_6	20.6	0.5	23.4	0.3
β	48.7	0.5	69.7	0.6

source will not have satellites or Bremsstrahlung radiation.[4.18]

In the XPS spectra, the peaks are located against a background which has gradual and steplike increases with increasing binding energy. The gradual background is due to the Bremsstrahlung radiation (absent in monochromatic X-ray sources), whereas the steplike increases are due to electrons which undergo inelastic interactions before emerging from the sample.[4.18]

XPS analysis of insulator materials present unique difficulties in data collection and analysis.[4.11,22,23] Insulators typically have charging effects producing peak energy shifts and width broadening. For non-severe uniform charging, the shift is the same for all peaks. In extreme cases, splitting of peaks is observed. For uniform shifting of all peaks, adventitious carbon or a film *in situ* deposited on the sample can be used as reference. An alternative is to use a species of known energy position present in the sample as the reference. Low energy electron flood guns are also used to compensate for charging.

XPS data was collected in this work using the same Perkin Elmer DPCMA, AST computer, and PC interface used for AES analysis. The water cooled X-ray source (Perkin Elmer 04-548) provides non-monochromatized Mg Kα and Al Kα.

The XPS energy scale was calibrated twice over the course of this work. The first calibration used the Cu $2p_{3/2}$ (932.4 eV), Cu L$_3$VV (334.9 eV), and Cu $3p_{3/2}$ (74.9 eV) binding energy peak positions.[4.24] The second calibration, performed after replacement of the electron multipler in the DPCMA, used the Cu $2p_{3/2}$ (932.4 eV) and Au $4f_{7/2}$ (83.8

eV) binding energy positions.[4.24] The energy scale was assumed to be linear in both calibrations.

In this work, XPS was used to determine film stoichiometry and thickness. Qualitative analysis gives elemental identification from the peak position. Quantitative analysis giving film thickness and peak shifts requires several steps including background removal, satellite subtraction, and curving fitting. The assumptions used and additional details regarding data analysis are reviewed in Section 4.5.

4.3.3 Low energy electron diffraction (LEED)

In LEED, a beam of electrons is directed perpendicular to a crystalline sample. Electrons elastically diffracted off the surface are intercepted by a fluorescent screen. The result is a pattern of diffraction spots giving information regarding the surface crystalline structure.

The surface sensitivity is due to the use of electrons (10 - 500 eV) with limited mean free paths and wavelengths comparable to typical atomic distances.[4.13] The electron energy, E (eV), and wavelength, λ (Å), are related by the de Broglie equation:[4.13,25]

$$\lambda = \sqrt{150 / E} \qquad\qquad (4.3)$$

The condition for constructive interference between scattered waves is given by the following equation (Bragg condition):[4.17,25]

$$n \, \lambda = a \sin \theta \qquad\qquad (4.4)$$

where a, n, and θ are the interatomic distance, diffraction order, and angle of diffraction relative to the surface normal, respectively.

There are different levels of LEED analysis. The pattern of spots is representative of the reciprocal lattice. Real lattice unit cell size and orientation, and crystalline order are obtained from the position, sharpness,and brightness of the spots.[4.13] On a more advanced level, atomic positions are determined from the spot intensities.

In this work, LEED was used to determine and confirm the degree of substrate surface crystalline order. The LEED apparatus is a four-grid system from Perkin Elmer, model 15-120.

4.4   *Ex situ* characterization techniques

Three *ex situ* analytical techniques were used for characterization. They were X-ray diffraction (XRD), Rutherford backscattering spectroscopy (RBS), and atomic force microscopy (AFM). The first two techniques were applied to characterize thick films. The AFM was used for thin films.

The XRD was performed on a SCINTAG Theta - Theta Diffractometer, model PADX. The radiation used was Cu $K\alpha_1$. XRD provides information regarding the crystalline phases and orientation of materials. Different types of diffraction scans can be collected. They include θ-2θ and rocking curve scans. The θ-2θ type provides

identification of crystalline phases present when spectra peak positions are compared to tabulated values. The rocking curve type gives information concerning in-plane alignment of films.

RBS is used to provide elemental identification, stoichiometry determination, and film thickness. Stoichiometry and film thickness are determined from comparisons of simulated and experimental spectra. Simulations in this work were performed using the RUMP software from Computer Graphic Service, Ltd.

AFM was performed on a Digital Instruments Nanoscope Scanning Probe Microscope. It provides a topographic image of the surface of the material probed.

4.5   XPS data analysis

Film thickness can be obtained from XPS photoelectron peak heights or areas. Peak area is less affected by changes in peak shape or width. Obtaining peak areas requires several steps which typically include background subtraction, satellite removal, and curve fitting. These steps were performed in this work following recommended procedures from the literature. After background subtraction, satellite removal (where necessary), and curve fitting was completed, peak areas were determined by integration of the resulting experimental or curve fitted (in the case of overlapping peaks) peak. Data analysis was performed using GENPLOT: A Data Analysis and Graphics Program for Scientists and Engineers from Computer Graphic Services, Ltd.

4.5.1 Background subtraction

Two types of background subtraction are typically used.[4.2,26-29] In the linear background subtraction method, the background is taken as a straight line drawn between two appropriate points on the high and low binding energy sides of the peak. There is no physical basis for this method. It appears sufficient for cases where the slope between the two end points is not very large. A study by Bishop[4.27] evaluated the use of linear backgrounds in such a case. The choice of endpoints produced variations in area measurements of the same Fe $2p_{3/2}$ photoelectron peak. It was also concluded that for overlapping or doublet peaks, background subtraction should be performed across both peaks.

The second method is known as the Shirley or integrated background method. It assumes with each electron of particular energy is a background to lower kinetic energy.[4.2,26-29] The background at any point is proportional to the integrated area to lower binding (higher kinetic) energy. The background subtraction in this work followed the procedure outlined by Procter and Sherwood.[4.29] Background subtraction was an iterative process performed with the GENPLOT software. The iterative process ended when the determined peak area remained unchanged within a relative difference of 1×10^{-4}.

4.5.2 Satellite subtraction

The XPS spectra in this work showed satellites at lower binding

energies from main photoelectron peaks due to the use of non-monochromatic X-ray sources. The only satellite which overlapped a main peak of interest was the Mg $K\alpha_3$ satellite from the Ti $2p_{1/2}$ peak overlapping with the Ti $2p_{3/2}$ peak. The satellite was removed after integrated background subtraction. The satellite intensity and position relative to the main peak generated by the Mg $K\alpha$ X-rays was given in Table 4.1.

4.5.3   Curve fitting

The purpose of curve fitting or synthesis is to fit created peaks to experimental ones in order to separate contributions from overlapping peaks or determine peak parameters.[4.2,26,30] The synthesized peaks are either Gaussian, Lorentzian or mixed Gaussian-Lorentzian functions. The peak parameters of interest include energy position, amplitude, full width at half maximum (FWHM), and the Gaussian-Lorentzian mixing factor.

A modified product of the Gaussian and Lorentzian function recommended by Evan[4.30] was used:

$$f(x) = \frac{\text{peak height}}{\left\{ \left(1 + Q\, m^{1/2} \right) \exp \left[\left(1 - m^{1/2} \right)^{\left(0.87 \, - \, 0.1855 \, m^{1/2} \right)} Q \ln 2 \right] \right\}} \tag{4.4}$$

Q is defined as:[4.30]

$$Q = \frac{\left(x - x_o \right)^2}{w^2} \qquad (4.5)$$

where x_o, w, and m are the peak center, half width at half maximum (FWHM/2), and mixing factor, respectively. The function given in equation 4.4 represents a pure Gaussian or Lorentzian when m is 0 or 1, respectively.

Equation 4.4 was used to curve fit single XPS peaks. For overlapped photoelectron peaks, the contribution of each peak was determined by curve fits to a sum of two functions given by equation 4.4. The fits were performed using macros in the GENPLOT program. The curve fit was completed when the program returned a relative unchanged chi-squared (χ^2) of less than 1 x 10^{-4}. The results of the curve fits are values and variances for the peak center, FWHM, peak height, and mixing factor for the mixed Gaussian-Lorentzian function which produces the best χ^2.

4.6   Error analysis

Uncertainties in data may be due to random statistical variations in data collection or systematic errors, i.e, due to equipment calibrations. XPS peak position, area and film thickness uncertainties are discussed in turn below. Evaluations of uncertainties was conducted

by following the procedures described in *An Introduction to Error Analysis* by J.R. Taylor.[4.31]

XPS peaks positions can have systematic error due to compression or extension of the energy scale. Since the XPS system used in this work was calibrated, such errors should be minimal. To determine the uncertainties arising from random errors, sets of repeated XPS scans of the Al $2p$ photoelectron peak were collected during the course of this work from clean substrates, substrates with varying film thicknesses, data collected with and without use of the low energy electron flood gun. Peak positions were determined by curve fitting. The standard deviation of the mean (SDOM) for each set of repeated spectra was determined. The number of repeats in each set, which totaled nine, was typically two. The average of the SDOM was 0.04 eV and was used as a measure of XPS peak position uncertainties for all photoelectron peaks. The uncertainties for all photoelectron peaks should be the same.

XPS peak areas can have systematic errors due to the collection system under or over counting the intensity, or from procedures used to obtain the area from the peaks. Systematic errors were minimized by the application of peak area ratios whenever possible in quantitative analysis. The random error was determined in a similar manner as in the case of peak positions. The average ratio of peak area to SDOM of nine sets of repeated scans of the Al $2p$ peak was 1.4%. This was taken as the uncertainties of all XPS peak areas.

There are three sources of error in the film thickness

determination. They are error from the peak area determination, the bulk standard area intensity ratio, $I_\infty^{Ti} / I_\infty^{Al}$,(discussed Section 5.3.4) and the graphical method used to determine the film thickness from the area (discussed in Section 6.3.1). The uncertainties for each are 1.4%, 0.05, and 0.01 ML, respectively. Of these, the error from the peak area determination and bulk intensity ratio propagated the largest uncertainties in film thickness. Propagation of error from these two sources produced film thickness uncertainties ranging from 0.01 ML for a film 0.3 ML thick to 0.1 for a film 8.2 ML thick.

4.6   References for Chapter 4

4.1   J.P. Lu and R. Raj, "Ultra-high Vacuum Chemical Vapor Deposition and *In situ* Characterization of Titanium Oxide Thin Films," *J. Mater. Res.*, **6** [9] 1913-18 (1991).

4.2   J.C. Rivière, *Surface Analytical Techniques*; Ch. 3, pp. 27-80, Ch. 1, pp. 1-4. Oxford University Press, New York, 1990.

4.3   J.F. O'Hanlon, *A User's Guide to Vacuum Technology*, 2nd Edition; Ch. 16, pp. 279-301. John Wiley & Sons, New York, 1989.

4.4   V.S. Smentkowski and J.T. Yates, Jr., "A Multipurpose Quadrupole Mass Spectrometer Detector for Surface Kinetic and Absolute Coverage Measurements," *J. Vac. Sci. Technol., A,* **7** [6] 3325-31 (1989).

4.5   J.P. Lu, R. Raj, and A. Wernberg, "Ultra-high Vacuum Metalorganic Chemical Vapor Deposition of GaAs Thin Films Onto Si(100) Using a Single-Source Precursor," *Thin Solid Films*, **205**, 236-40 (1991).

4.6   T.M. French and G.A. Somorjai, "Composition and Structure of the (0001) Face of α-Alumina by Low-Energy Electron Diffraction," *J. Phys. Chem.*, **74** [12] 2489-95 (1970).

4.7   M. Arbab, G. S. Chottiner, and R.W. Hoffman, "An ARXPS Investigation of the Initial Growth of Aluminum Films on the (0001) Face of Sapphire," *Mater. Res. Soc. Symp. Proc.*, **153**, 63-69 (1989).

4.8   A.C. Diebold, S.W. Steinhauser, R.P. Mariella, Jr., J. Marti, F. Reidinger, and R.F. Antrim, "Growth and Characterization of GaAs on Sapphire (0001) by Molecular Beam Epitaxy," *Surf. Interface Anal.*, **15**, 150-58 (1990).

4.9   C.C. Chang, "LEED Studies of the (0001) Face of α-Alumina," *J. Appl. Phys.*, **39** [12] 5570-73 (1968).

4.10   C.C. Chang, "Silicon-on-Sapphire Epitaxy by Vacuum Sublimation: LEED-Auger Studies and Electronic Properties of the Films," *J. Vac. Sci. Technol.*, **8** [3] 500-11 (1971).

4.11   P. Swift, D. Shuttleworth and M.P. Seah, "Appendix 2. Static Charge Referencing Techniques"; pp. 437-44 in *Practical Surface Analysis by Auger and X-ray Photoelectron Spectroscopy*. Edited by D. Briggs and M.P. Seah. John Wiley &

Sons, Chichester, 1983.

4.12   M.P. Seah and D. Briggs, "Chapter 1. A Perspective on the Analysis of Surfaces and Interfaces"; pp. 1-15 in *Practical Surface Analysis by Auger and X-ray Photoelectron Spectroscopy*. Edited by D. Briggs and M.P. Seah. John Wiley & Sons, Chichester, 1983.

4.13   G. A. Somorjai, *Chemistry in Two Dimensions: Surfaces*; Ch. 2, pp. 37-99. Cornell University Press, Ithaca, New York, 1981.

4.14   J.C. Rivière, "Chapter 2. Instrumentation"; pp. 17-85 in *Practical Surface Analysis by Auger and X-ray Photoelectron Spectroscopy*. Edited by D. Briggs and M.P. Seah. John Wiley & Sons, Chichester, 1983.

4.15   P.G. Harris and A.D. Trigg, "Surface Analysis Techniques and Their Application to Materials Characterization," *Materials Design*, **9** [3] 127-34 (1988).

4.16   *Practical Surface Analysis by Auger and X-ray Photoelectron Spectroscopy*. Edited by D. Briggs and M.P. Seah. John Wiley & Sons, Chichester, 1983.

4.17   G. Ertl and J. Küppers, *Low Energy Electrons and Surface Chemistry*. VCH Publishers, Deerfield Beach, Fl, 1985.

4.18   D. Briggs and J.C. Rivière, "Chapter 3. Spectral Interpretation"; pp. 87-139 in *Practical Surface Analysis by Auger and X-ray Photoelectron Spectroscopy*. Edited by D. Briggs and M.P. Seah. John Wiley & Sons, Chichester, 1983.

4.19   L.E. Davis, N.C. Macdonald, P.W. Palmberg, G.E. Riach, and R.E. Weber, *Handbook of Auger Electron Spectroscopy*. Perkin-Elmer Corporation, Eden Prairie, Minnesota, 1978.

4.20   J.P. Lu, P.W. Chu, and R. Raj, "Ultrahigh Vacuum Chemical Vapor Deposition of Rhodium Thin Films on Clean and TiO_2-Covered Si(111)," *Thin Solid Films*, **208**, 172-76, (1992).

4.21   J.F. Moulder, W.F. Stickle, P.E. Sobol, and K.D. Bomben, *Handbook of X-ray Photoelectron Spectroscopy*. Edited by J. Chastain. Perkin Elmer Corporation, Eden Prairie, Minnesota, 1992.

4.22   H.W. Werner and N. Warmoltz, "Beam Techniques for the Analysis of Poorly Conducting Materials," *J. Vac. Sci. Technol., A*, **2** [2] 726-31 (1984).

4.23   T.E. Madey, C.D. Wagner, and A. Joshi, "Surface Characterization of Catalysts Using Electron Spectroscopies: Results of a Round-Robin Sponsored by ASTM Committee D-32 on Catalysts," *J. Electron Spectrosc. Relat. Phenom.*, **10**, 359-88 (1977).

4.24   C.D. Wagner, W.M. Riggs, L.E. Davis, and J.F. Moulder, *Handbook of X-ray Photoelectron Spectroscopy*. Edited by G.E. Muilenberg. Perkin-Elmer Corporation, Eden Prairie, Minnesota, 1979.

4.25   L.C. Feldman and J.W. Mayer, *Fundamentals of Surface and Thin Film Analysis*; Ch. 7, pp. 161-67. North Holland, New York, New York, 1986.

4.26   P.M.A. Sherwood, "Appendix 3. Data Analysis in X-ray Photoelectron Spectroscopy"; pp. 445-475 in *Practical Surface Analysis by Auger and X-ray Photoelectron Spectroscopy*. Edited by D. Briggs and M.P. Seah. John Wiley& Sons, Chichester, 1983.

4.27   H.E. Bishop, "Practical Peak Area Measurements in X-ray Photoelectron Spectroscopy," *Surf. Interface Anal.*, **3** [6] 272-74 (1981).

4.28   D.A. Shirley, "High-Resolution X-ray Photoelectron Spectrum of the Valence Bands of Gold," *Phys. Rev. B*, **5** [12] 4709-14 (1972).

4.29   A. Procter and P.M.A. Sherwood, "Data Analysis Techniques in X-ray Photoelectron Spectroscopy," *Anal. Chem.*, **54,** 13-19 (1982).

4.30   S. Evans, "Curve Synthesis and Optimization Procedures for X-ray Photoelectron Spectroscopy," *Surf. Interface Anal.*, **17**, 85-93 (1991).

4.31   J.R. Taylor, *An Introduction to Error Analysis*. University Science Book, Mill Valley, CA, 1982.

Chapter 5
UHV-MOCVD of Titanium Dioxide from Titanium Isopropoxide Precursor

5.1   Introduction

Characterization of the chemical vapor deposition processes and parameters producing titanium oxide from titanium isopropoxide precursor establishes the conditions for optimized film growth. The issues of interest include the precursor thermal decomposition temperature, deposition below and above the thermal decomposition temperature, presence of impurity carbon, and film stoichiometry. The observations are applied in Chapters 6 and 7 to produce controlled submonolayer depositions of titanium dioxide and to study the interface between the film and substrate.

Growth of titanium oxide by MOCVD from titanium isopropoxide without the use of an additional oxygen or water source was reported for deposition pressures ranging from low pressure to ultrahigh vacuum.[5.1-8] Films were produced at substrate temperatures as low as 220°C on copper at 0.04 Torr,[5.4] 250°C on sapphire (0001) at 8 x 10^{-6} Torr,[5.6] and 300°C on sapphire at 1 x 10^{-8} Torr.[5.8]

Siefering and Griffin[5.4] studied the decomposition of titanium isopropoxide by temperature-programmed desorption (TPD). Copper substrates were dosed for 10-1000 L (1 L = 10^{-6} Torr sec) with precursor at 27°C. The substrate was then heated at a constant rate. By monitoring

desorption products as a function of temperature, it was concluded the titanium isopropoxide on copper decomposed in two reactions at 177° and 347°C.

In this work, the precursor pyrolysis temperature was determined by two methods. In the first case, depositions on sapphire at temperatures ranging from room temperature to 700°C were systematically evaluated. In the second case, pyrolysis of precursor initially adsorbed on sapphire at low temperatures was determined by characterizing the surface composition as a function of post-deposition annealing.

It has been reported that carbon residue in films produced from titanium isopropoxide decreased with increased film thickness.[5.7,8] In thick films, carbon was not detected within the limits of XPS or AES.[5.7,8] Carbon content was used in this chapter to track the decomposition of titanium isopropoxide adsorbed on the substrate.

From their TPD study, Siefering and Griffin[5.4] also proposed precursor adsorption should reach a saturation limit. In this work, the use of an ultrahigh vacuum growth chamber with *in situ* surface sensitive techniques provides the ability to produce and directly characterize the very thin depositions resulting from dosing below pyrolysis. Growth as a function of exposure was evaluated.

Two research groups have reported the growth of stoichiometric TiO_2 from titanium isopropoxide precursor without the addition of oxygen or water in ultrahigh vacuum chambers. Lu and Raj[5.8] reported the growth of stoichiometric TiO_2 on silicon as determined by XPS

analysis. Chen et al.,[5,6,7] reported the growth of stoichiometric TiO_2 on strontium titanate and sapphire as determined by AES analysis. XPS analysis is used in this chapter to confirm the stoichiometry of thick films grown on sapphire.

The relatively thick films produced for film stoichiometry analysis were also used as internal calibration standards for quantitative analysis in Chapters 6 and 7. Thick films were evaluated by *ex situ* X-ray diffraction (XRD) to determine the titanium dioxide phases, anatase or rutile, present as a function of deposition temperature. Observations are compared to XRD reports in the literature.

5.2   Experimental procedure

5.2.1   Sapphire preparation

The substrates used were single crystal aluminum oxide, sapphire, with the basal (0001) orientation. They were obtained from two sources, the Union Carbide Company and Commercial Crystal Laboratories, Incorporated. Specifications for the sapphire are summarized in Table 5.1. Treatment of the sapphire before introduction to the chamber included degreasing and backcoating with tantalum film. Received sapphire were degreased in baths of trichloroethylene, acetone, and isopropanol.

The sapphire was sputter coated with 1000 Å of tantalum on one of the polished sides or the nonpolished side to improve heating. This

Table 5.1. Specifications for Sapphire Substrates

Specification	Sapphire Company Source	
	Union Carbide Company	Commercial Crystal Lab., Inc.
Size	0.5 in. x 0.5 in.	0.5 in. x 0.5 in.
Thickness	0.025 in.	0.020 in.
Orientation	(0001)	(0001)
Off-axis	$\pm 0.5°$	$\pm 0.5°$
Finish	Polish both sides	Polish one side

metallic film was placed in direct contact with the heater. It acted as a heat receptor for the sapphire. After tantalum backcoating, the sapphire was again degreased using the same procedure for the as received sapphire, then mounted on the chamber manipulator.

Sapphire introduced into the chamber was *in situ* cleaned by cycles of Ar+ sputtering (beam energy of 0.5 KeV, current of 20 mA and argon pressure of 5.5 x 10^{-5} Torr) and annealing at 600°-700°C. According to AES analysis (electron beam energy of 3 KeV, filament current of 0.4 mA), sapphire introduced into the chamber showed only the presence of surface carbon impurity. This carbon was removed by sputtering and annealing. The presence of calcium was also observed after annealing. This calcium is due to surface segregation from the bulk. It has been previously reported[5.9-11] to occur after annealing single crystal and polycrystalline alumina. After repeated sputtering and annealing cycles, the presence of calcium was not detected again within the limits of AES or XPS.

The sapphire was also cleaned *in situ* between experiments. This permitted the use of the same substrate for multiple experiments. Prior to each experiment, the substrate was cleaned until titanium was not observed within the detection limit of AES or XPS. Unless noted, experiments were conducted on the same sample.

Depositions were conducted on sapphire showing the (1 x 1) LEED pattern (screen energies of 3-4 KeV, beam energy of 180-300 eV and filament current of 1 mA). Although this pattern could be reproduced after cleaning off previous depositions, the sharpest pattern

was seen with cleaned Union Carbide sapphire before any depositions.

Sputtering has been reported to alter the surface by creating structural and compositional changes.[5.12,13] Annealing repairs structural damage by surface diffusion, and composition changes by diffusion of deficient species from the bulk. Annealing restored the pattern, but may not completely repair all damage caused by the sputtering. The sputtering and annealing procedure for this work was developed by annealing until improvements in the LEED patterns were not observed.

5.2.2   Titanium isopropoxide dosing

The titanium isopropoxide precursor was purchased from Aldrich with a purity of 97%. Additional precursor specifications and physical constants are summarized in Table 3.1. The precursor was loaded into a Pyrex vial, mounted on the dosing line, then purified by cycles of H_2O ice bath freeze and thaw cycles.[5.8]

In a typical dosing experiment, the substrate was heated to the deposition temperature. Vapor from room temperature titanium isopropoxide was introduced to the chamber through the dosing tube and directed at the substrate facing the tube. During dosing, the chamber pressure was maintained at 1×10^{-8} Torr. The chamber base pressure was better than 1×10^{-10} Torr. After the substrate was dosed for a specified time period, the vapor leak valve was closed. The chamber was pumped down. For the experiments described in this chapter, the

substrate faced the dosing tube when vapor was first introduced into the chamber. Deposition timing began when the chamber pressure reached 1×10^{-8} Torr. After dosing, the sample was cooled down and turned to face the DPCMA for analysis.

The dosing pressure reported was the pressure in the chamber. Since a dosing tube was used in introducing precursor vapor to the chamber, the flux (molecules/m^2 sec) emerging from the tube is expected to be higher than in the chamber. In Appendix 1 the flux from the tube is determined and compared to the flux within the chamber for a pressure of 1.0×10^{-8} Torr.

The film stoichiometry was determined by XPS of relatively thick films on different substrate samples. The use of thick films ensured the XPS analysis depth was limited to bulk titanium oxide and did not include the film to substrate interface or oxygen from the sapphire substrate. Possible interactions at the interface or inclusion of oxygen from sapphire would give erroneous photoelectron peak positions or areas. The issues of interface reaction and O $1s$ peak position with film thickness are addressed in Chapter 7.

For the thick films used in stoichiometry determination, titanium oxide was deposited until the presence of an Al $2p$ peak was not detected by XPS. Using the model proposed by Seah and Dench,[5.14] the inelastic mean free path (IMFP) of Al $2p$ photoelectrons through the film was calculated to be longer than O $1s$. Since the Al $2p$ photoelectrons IMFP are longer, the lack of Al $2p$ in the XPS scans ensures signals from the interface and substrate are not included. The IMFP of Al $2p$

through anatase and rutile were calculated as 2.65 and 2.51 nm, respectively. The IMFP of O $1s$ through anatase and rutile were calculated as 2.07 and 1.96 nm, respectively.

5.2.3 Post-deposition annealing

Post-deposition annealing was conducted on samples in which the substrate, at 22° or 200°C, was first dosed with precursor vapor for a total of 26.7 minutes. After dosing, the sample was annealed at temperatures ranging from 100° to 700°C, in increments of 100°C, for 10 minutes each. XPS analysis was performed after each anneal to characterize the effects of annealing.

5.2.4 AES analysis

AES analysis was used to characterize the sapphire surface after sputter cleaning and before a dosing experiment. The AES operating conditions were a beam energy and current of 3 KeV and 0.4 mA, respectively. It was not used to characterize deposited film for two reasons. The use of AES with an insulator substrate can produce charging effects which cannot easily be compensated for.[5.15,16] Spectra of thick titanium oxide films on sapphire were often distorted due to the charging. The second reason is due to beam effects which was summarized by Pantano and Madey.[5.17] A beam effect was observed for the deposition of titanium isopropoxide below its pyrolysis temperature.

5.2.4   XPS analysis

XPS analysis was conducted before and after dosing, and after post - deposition annealing. The Mg anode at 300 watts and 15 KeV was used. Care was taken to reset the sample at the same dosing and analysis positions to ensure reproducible results. Two types of XPS scans were taken, survey and narrow scans. Survey scans produced spectra of all peaks present at binding energies of 1000 to -5 eV. They were collected at pass energies of 100 eV, in increments of 1 eV/step, 50 ms/step, and averaged over ten sweeps. Narrow scans produced spectra of individual peaks within a range of 10 to 20 eV. They were collected at pass energies of 50 eV, in increments of 0.05 eV/step, 100 ms/step, and averaged over twenty sweeps.

At the start of each experiment, survey and narrow spectra of O 1s, Al 2p, Ti 2p (includes $2p_{1/2}$ and $2p_{3/2}$), and C 1s photoelectron peaks were collected. The Ti 2p peak was taken to check for the presence of titanium from previous experiments. After dosing or post-deposition annealing, survey and narrow scans of the same peaks were collected.

Photoelectron peak areas and positions were determined by subtracting backgrounds using the integrated Shirley method,[5.18,19] subtracting the Mg anode satellite,[5.20] and fitting to mixed Gaussian-Lorentzian peaks.[5.21] Contributions from the overlapping $2p_{3/2}$ and $2p_{1/2}$ peaks to the Ti 2p peak [5.20] were separated by curve fitting to two mixed Gaussian-Lorentzian peaks. It was assumed the mixing factor for the two peaks were the same. Additional details regarding XPS data

analysis were provided in Section 4.5.

The use of XPS to analyze insulator materials can produce charging effects. They include shifting of photoelectron peaks or in extreme cases, additional peaks.[5.22] Charging due to the sapphire substrate produced shifts in the XPS binding energies. For thin depositions, it was assumed charging was uniform and all peaks shifted by the same amount.[5.22] Due to this charging, absolute photoelectron binding energy positions were not determined. Peak positions are given as differences between two photoelectron peaks, i.e., O $1s$ and Ti $2p_{3/2}$.

In some relatively thick films, the charging was severe enough to produce peak splitting. In this chapter, the low energy electron flood gun was used during XPS analysis of thick films grown at 300°C. The flood gun was used at an emission current of 2.6 A, filament current of 0.7 mA, and electron voltage of 14 volts.

5.2.5 *Ex situ* analysis of thick films

XRD was used to determine the crystalline phases of TiO_2 present in thick films deposited at 300° and 700°C. For the 300°C film, only a θ–2θ scan was collected. For the higher temperature film, in addition to the θ–2θ scan, rocking curve analysis was also performed to evaluate the film in-plane alignment.

RBS was used to determine the film thicknesses. Spectra were collected with He^{2+} ions with 2.4 MeV energy at an angle of 30° to the surface normal. Film thicknesses were determined from RUMP

simulations. The films were assumed to have the density of anatase. The densities of anatase and rutile are 0.868×10^{23} and 0.963×10^{23} atoms/cm^3, respectively. The choice of density did not produce a significant difference in the RUMP simulations.

5.3   Results and discussions

5.3.1   Pyrolysis temperature

The pyrolysis temperature of titanium isopropoxide precursor was determined by dosing sapphire at substrate temperatures of 22° (room temperature, R.T.), 200°, 300°, 400°, and 700°C. XPS survey scans for each temperature are shown in Figure 5.1. All depositions were made with a total dose time of 3.3 minutes. These films were made on the same sapphire substrate sputter cleaned between experiments.

The key peaks of interest are O 1s, Al 2p, Ti 2p, and C 1s. A comparison of the scans shows at R.T. and 200°C, the Ti 2p peak is relatively small compared to the Al 2p peak. At 300°C and higher, the Ti 2p peak is much larger indicating a thicker deposition. This suggests precursor thermal decomposition has occurred. A small C 1s peak was observed at all substrate temperatures. Since growth and analysis was conducted in a vacuum chamber on sapphire initially showing no carbon, the carbon was introduced in the precursor molecule. At R.T. and 200°C, the carbon detected was due to carbon in the non-decomposed precursor on the sapphire surface. At 300°C and higher, the C 1s peaks
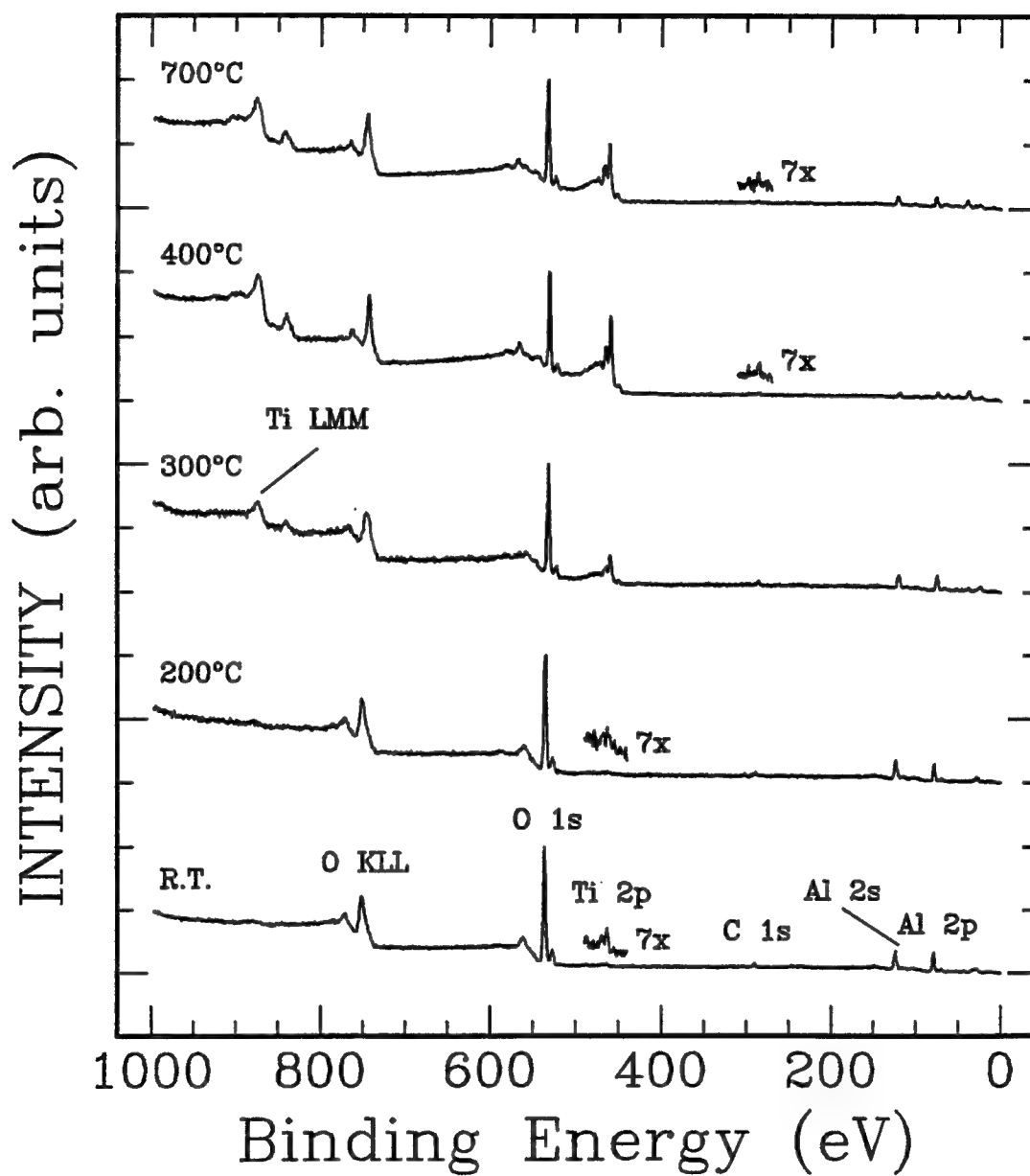
Figure 5.1. XPS survey scans of depositions on sapphire made at room temperature, 200°, 300°, 400°, and 700°C. The total dose time for each temperature was 3.3 minutes.

are relatively small compared to the Ti $2p$ peaks and can be explained as due to carbon trapped in the growing film.

The XPS survey scans indicate pyrolysis of titanium isopropoxide precursor occurs above 300°C. Continued dosing at substrate temperatures above this temperature produced continued attenuation and increase of the Al $2p$ and Ti $2p$ peaks, respectively. This indicates thicker films were grown. Dosing below the pyrolysis temperature was studied in greater detail in the next two sections.

5.3.2 Deposition below pyrolysis temperature

Deposition below the pyrolysis temperature was conducted to evaluate growth with increased deposition time. Figures 5.2 and 5.3 show the XPS peak areas of the Al $2p$ and Ti $2p_{3/2}$ photoelectrons as a function of deposition time for substrate temperatures of 22° and 200°C, respectively. Lines in the figures were drawn to indicate trends in the data. At both temperatures, uptake of titanium isopropoxide precursor occurs initially. This is indicated by the increase in Ti $2p_{3/2}$ peak area and attenuation of the Al $2p$ peak area. After approximately 15 minutes of dosing, increase and decrease of the Ti $2p_{3/2}$ and Al $2p$ peak areas, respectively, tapers off.

Similar growth behavior has been reported for the systems of oxygen on rhodium[5.23] and nitrogen on iron[5.24] In those systems, the depositing material adsorbed on the substrate until a saturation level was reached. Due to the low amount of deposition, a quantitative
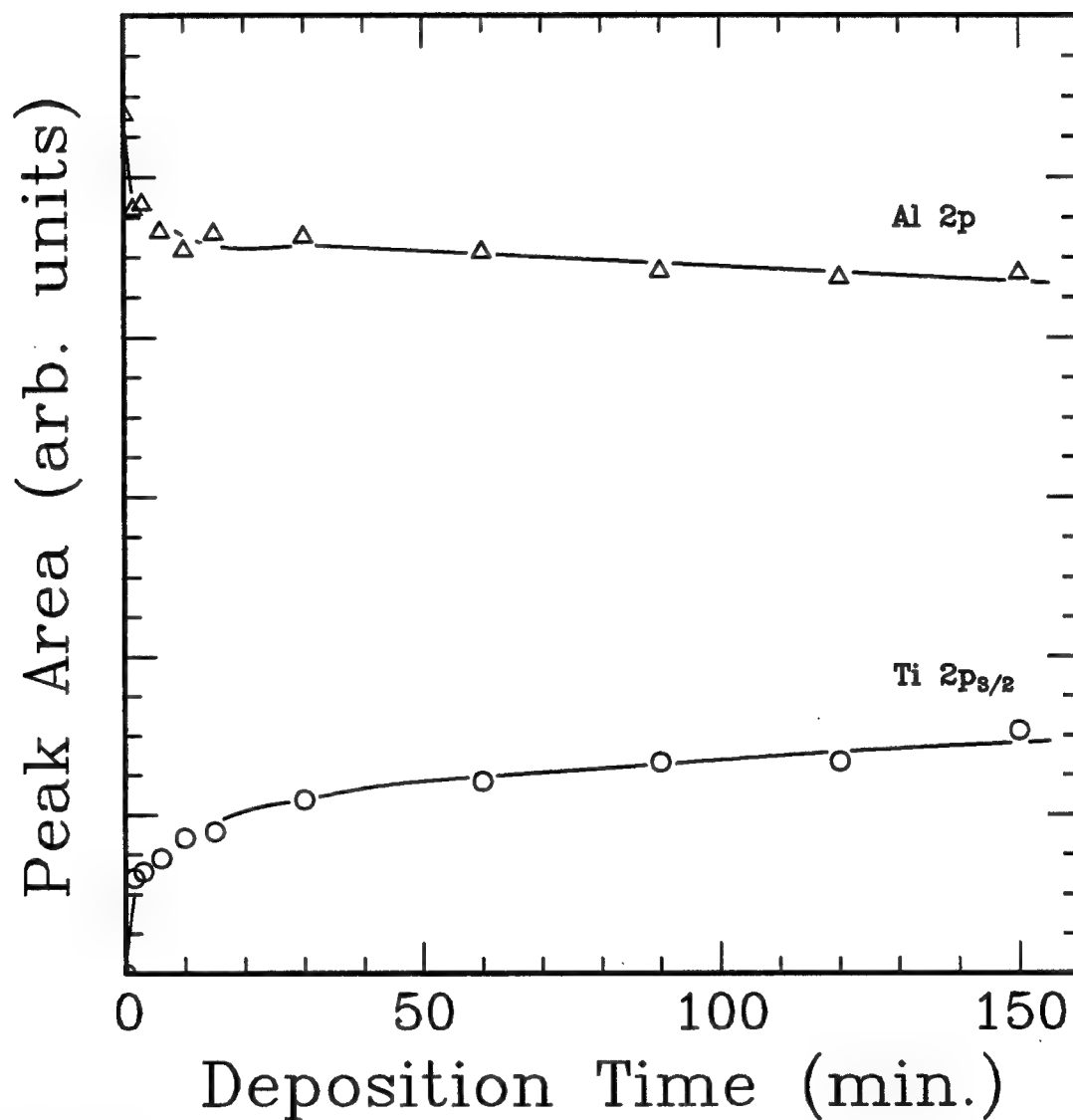
Figure 5.2. XPS Ti $2p_{3/2}$ and Al $2p$ photoelectron peak areas as a function of deposition time. The substrate deposition temperature was 22°C. The lines were drawn to show trends in the data.
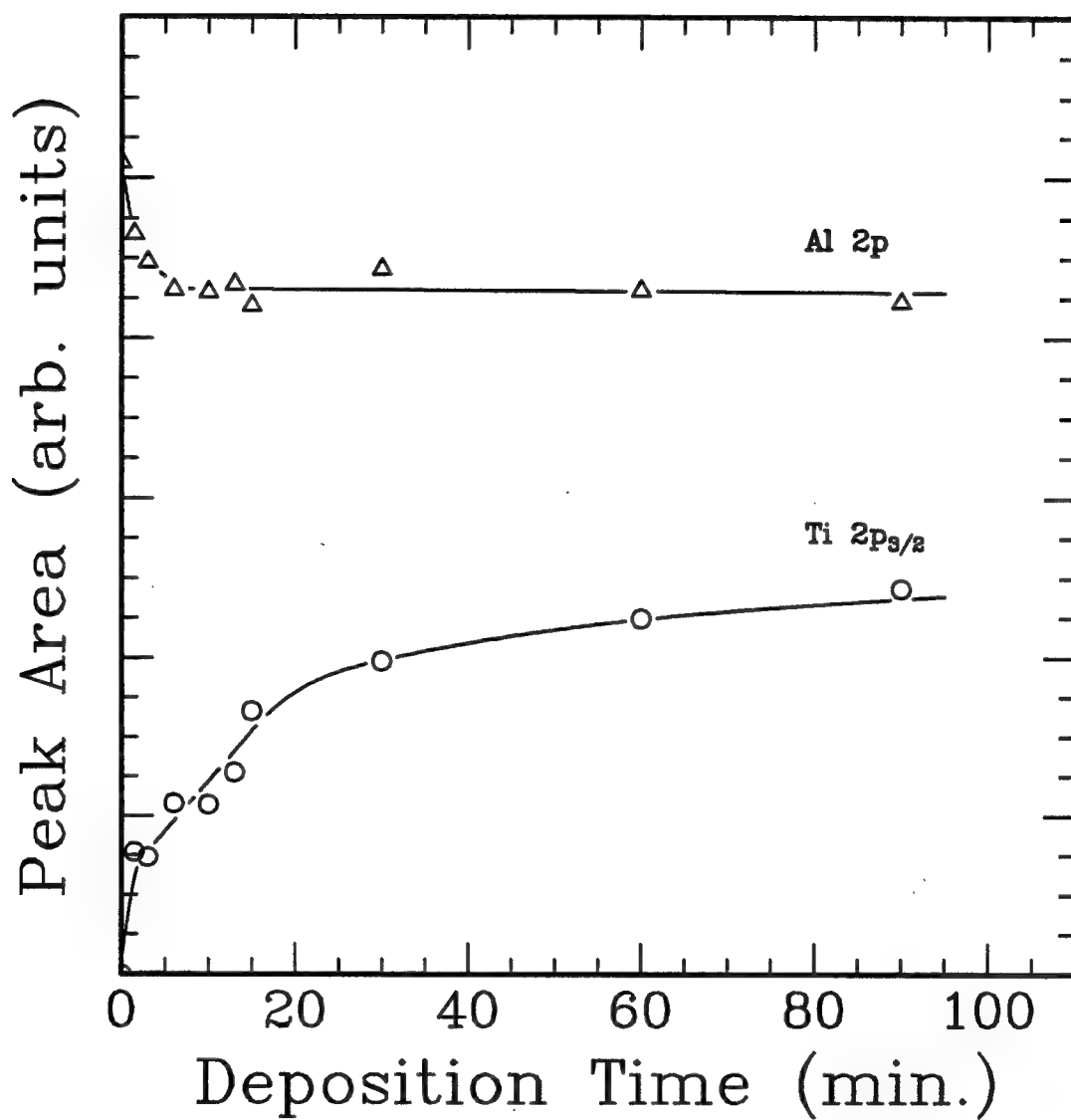
Figure 5.3. XPS Ti $2p_{3/2}$ and Al $2p$ photoelectron peak areas as a function of deposition time. The substrate deposition temperature was 200°C. The lines were drawn to show trends in the data.

analysis was not attempted from the peak intensities shown in Figures 5.2 and 5.3. The amount of titanium isopropoxide deposited below the pyrolysis temperature is evaluated in Chapter 6.

5.3.3   Post-deposition annealing of low temperature films

The decomposition temperature of the titanium isopropoxide molecules deposited on sapphire below the pyrolysis temperature was determined in post-deposition annealing experiments. XPS C $1s$ and Ti $2p$ peaks as a function of annealing temperature, are shown in Figures 5.4 and 5.5, respectively, for an initial deposition at 22°C. The spectra shown are after the initial deposition and annealing at 200°, 300°, and 400°. Ti $2p$ spectra after annealing at 700°C was also included. Although not shown, the sample was also annealed at intermediate temperatures of 500° and 600°C.

The C $1s$ peak was used to track the decomposition of the titanium isopropoxide. The Ti $2p$ peaks was collected to determine if a corresponding loss of titanium occurs with the carbon. Loss of both would indicate desorption and not only pyrolysis of the titanium isopropoxide occurred. Figures 5.4 shows carbon leaves the surface with post-deposition annealing at 300°C. The Ti $2p$ peaks do not show a corresponding attenuation. They exhibited a slight sharpening which could be atttributed to loss of carbon. In Figure 5.4, the lower intensity observed for C $1s$ at 100°C is an artifact. As shown in Figure 5.5,
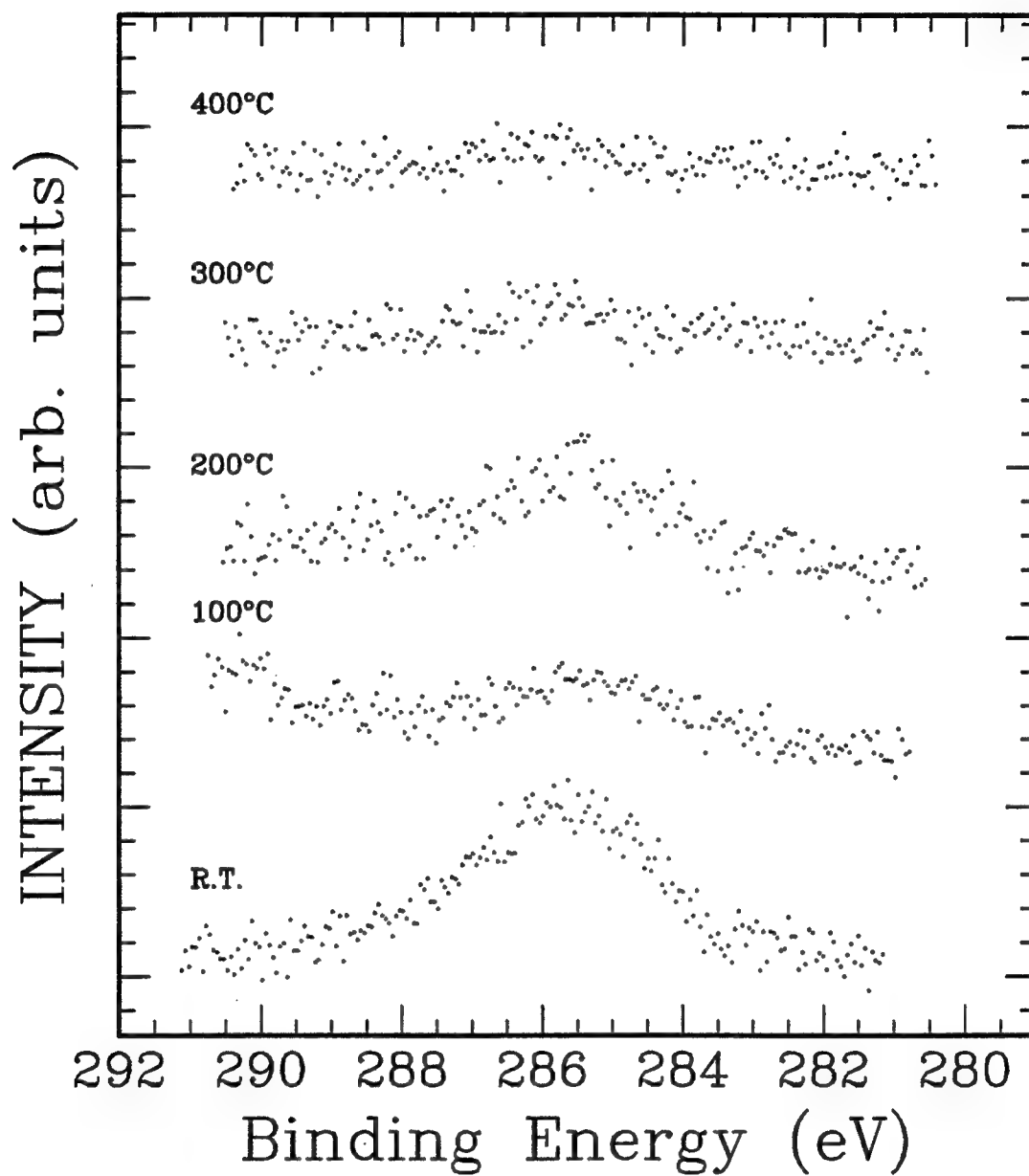
Figure 5.4. XPS C 1s spectra after post-deposition annealing for 10 minutes each at 100°, 200°, 300°, and 400°C. The initial deposition was made at 22°C.
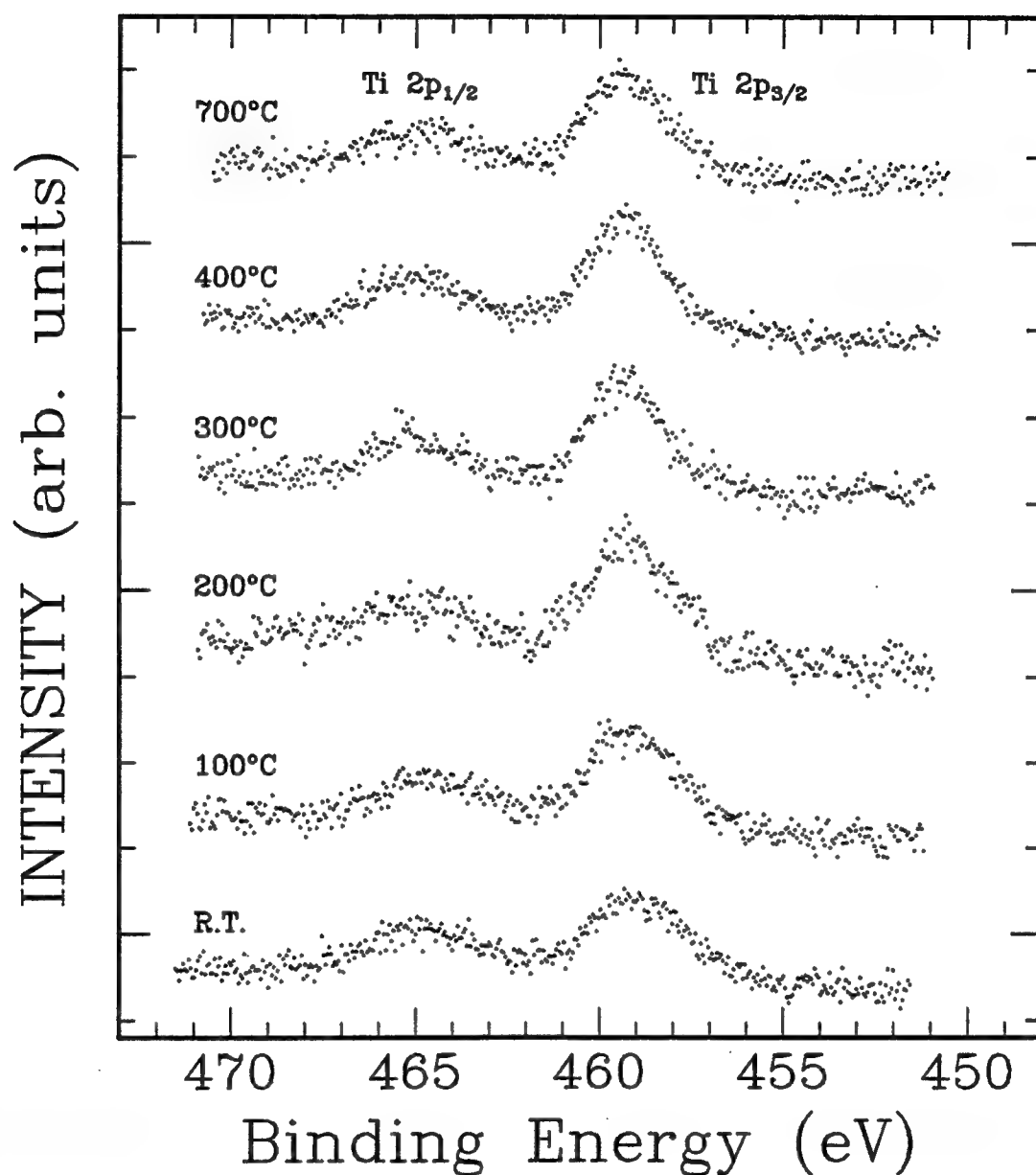
Figure 5.5. XPS Ti 2p spectra after post-deposition annealing for 10 minutes each at 100°, 200°, 300°, 400°, and 700°C. The initial deposition was made at 22°C. The sample was also post-deposition annealed at 500° and 600°C.

continued post-deposition annealing to 700°C did not produce decreases in the Ti $2p$ peak intensities within the sensitivity of XPS.

The post-deposition annealing experiments and the experiments described in Section 5.3.1 both show thermal decomposition of titanium isopropoxide precursor occurs above 300°C.

5.3.4 Stoichiometry of thick films

Thick films were grown at substrate temperatures of 300° and 400°C to determine stoichiometry, and obtain XPS peak intensities from bulk titanium oxide. These intensities are used as standards in Chapters 6 and 7 for quantitative analysis. Stoichiometries and intensities were obtained from XPS spectra collected after 15, 30, and 210 minutes of deposition for the 300°C film, and after 10 and 15 minutes of deposition for the 400°C film. The XPS spectra did not show the presence of the Al $2p$ peak. The 300°C film was analyzed by RBS after 210 minutes. The spectra is shown in Figure 5.6. The solid line is the RUMP simulation for a thickness of 1000 Å.

The Ti $2p_{3/2}$ and $2p_{1/2}$ photoelectron binding energies show distinct positions for different valence states. This includes titanium in TiO_2, Ti_2O_3, TiO, and Ti metal. Film stoichiometry was determined from O $1s$ - Ti $2p_{3/2}$ and Ti $2p_{3/2}$ - Ti $2p_{1/2}$ binding energy differences. A comparison of literature and experimental values are summarized in Table 5.2.[5.20,25-27] The experimental O $1s$ - Ti $2p_{3/2}$ and Ti $2p_{1/2}$ - Ti $2p_{3/2}$ differences (uncertainties of $\pm$ 0.06 eV) from the 300° and 400°C films

Figure 5.6. RBS spectrum of a thick film deposited at 300°C. The line is a RUMP simulation for a thickness of 1500 Å.

Table 5.2. Comparison of Literature and Experimental XPS
Binding Energy Differences (eV)

	XPS Binding Energy Differences (eV)		
	O $1s$ - Ti $2p_{3/2}$	Ti $2p_{1/2}$ - Ti $2p_{3/2}$	Ref.
Compound			
TiO$_2$	71.3, 71.5	5.4, 5.5, 5.7	5.20, 25-27
Ti$_2$O$_3$	73.4	5.2	5.25, 26
TiO	75.0, 75.6	5.6	5.25, 26
Ti	77	6.2	5.20, 26
Measured Exp. Values			
Substrate T. = 300°C	71.34	5.64	
Substrate T. = 400°C	71.38	5.65	

agree with the literature values for a TiO_2 stoichiometry.

The peak area ratio of the Ti $2p$ doublet should be 2:1 for Ti $2p_{3/2}$: Ti $2p_{1/2}$. The area ratio from the 300° and 400° C films were 2.07 ± 0.02 which agrees with the expected value. Assuming the same mixing factor in the mixed Gaussian Lorentzian curve fitting routine did not appear to significantly affect the curve fits.

XPS intensities from bulk standards are available as tabulations in the literature.[5.20] They are often given referenced to a single element such as F $1s$, and referred to as sensitivity factors. Photoelectron signals vary from spectrometer system to system. For quantitative purposes, photoelectrons signals from bulk standards should be collected on the same system and with the same conditions as the data to be analyzed. The value needed is the ratio of area intensities of Ti $2p_{3/2}$ from bulk TiO_2 to Al $2p$ from clean sapphire. This ratio was determined experimentally from the thick films as 3.43 ± 0.05.

5.3.5 XRD of thick films

The titanium dioxide phases present in thick films made by continuous depositions at 300° and 700°C were *ex situ* determined by X-ray diffraction. These temperatures were chosen because they span the range above pyrolysis temperature studied in this work. The films were produced on different substrate pieces. The RBS spectrum for the 300°C film was shown in Figure 5.6. The RBS spectrum from the 700°C film is shown in Figure 5.7. The solid line is a RUMP simulation for a
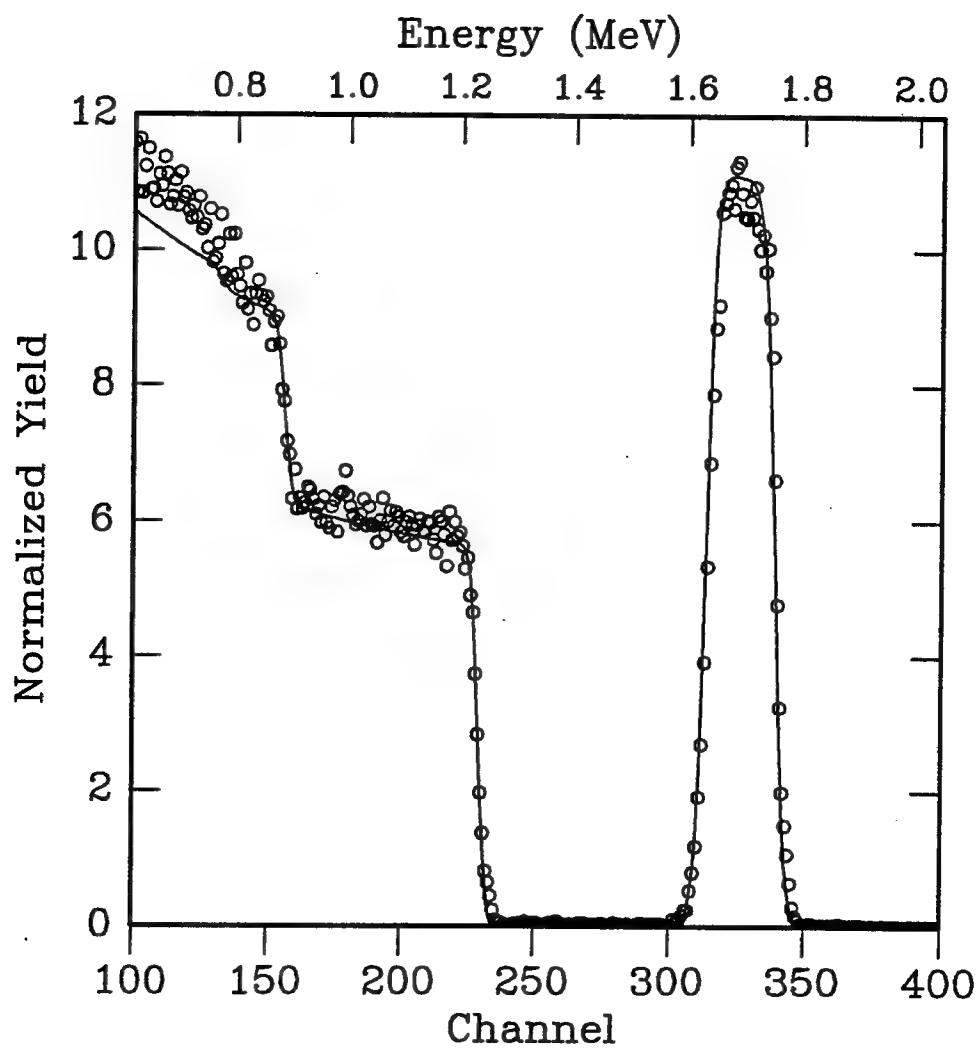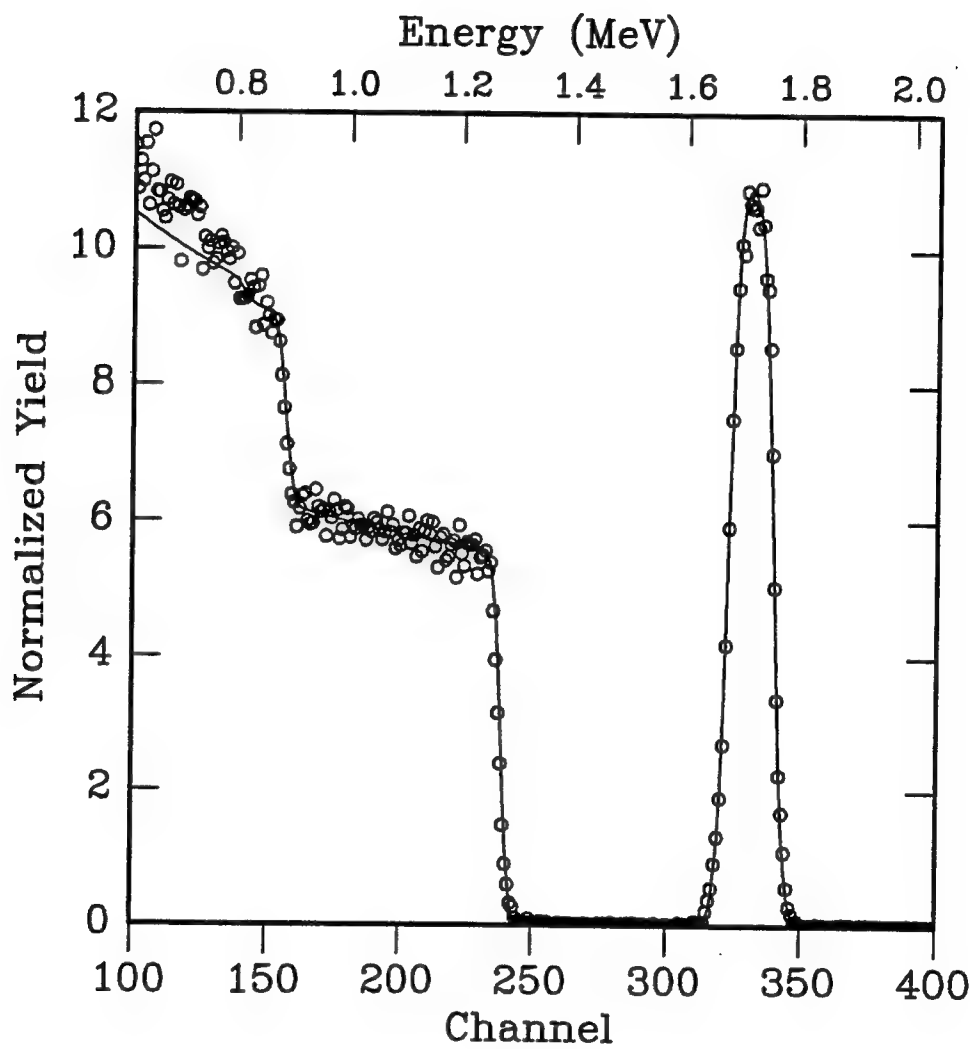
Figure 5.7. RBS spectrum of a thick film deposited at 700°C. The line is a RUMP simulation for a thickness of 1000 Å.

thickness of 1000 Å. The higher temperature film was not used for film stoichiometry in Section 5.3.4 because it showed the presence of a small amount of Al $2p$ signal in the XPS analysis which may be due to pinholes in the film.

Figures 5.8 and 5.9 show the X-ray θ-2θ spectra for the 300° and 700°C films, respectively. The inset in Figure 5.9 is a rocking curve scan of the rutile (200) peak from the higher temperature film. Although not shown, a θ-2θ diffraction scan was also collected for bare sapphire. The θ-2θ spectra indicate deposition at 300°C produced a film with anatase and rutile phases. The signals between 2θ of 35° to 38° were due to the sapphire.

Deposition at 700°C produced a film with only the rutile phase. The weak broad peak at 35° was due to the sapphire substrate. The rocking curve FWHM of 0.18 indicated the film had a high degree of in - plane alignment. The lowest FWHM measurable by the SCINTAG Diffractometer under optimum conditions, which include choice of slits and calibration, is 0.05°.

These XRD observations were made from thick films and are not necessarily applicable to the thin films produced in Chapters 6 and 7. The thin films could have different phases due to differences in deposition processing conditions or strain at the sapphire to film interface.

The phases determined as a function of deposition temperature qualitatively agrees with the observations of Chen, et al.[5.7] They reported the presence of anatase and rutile in films deposited on sapphire(0001) at
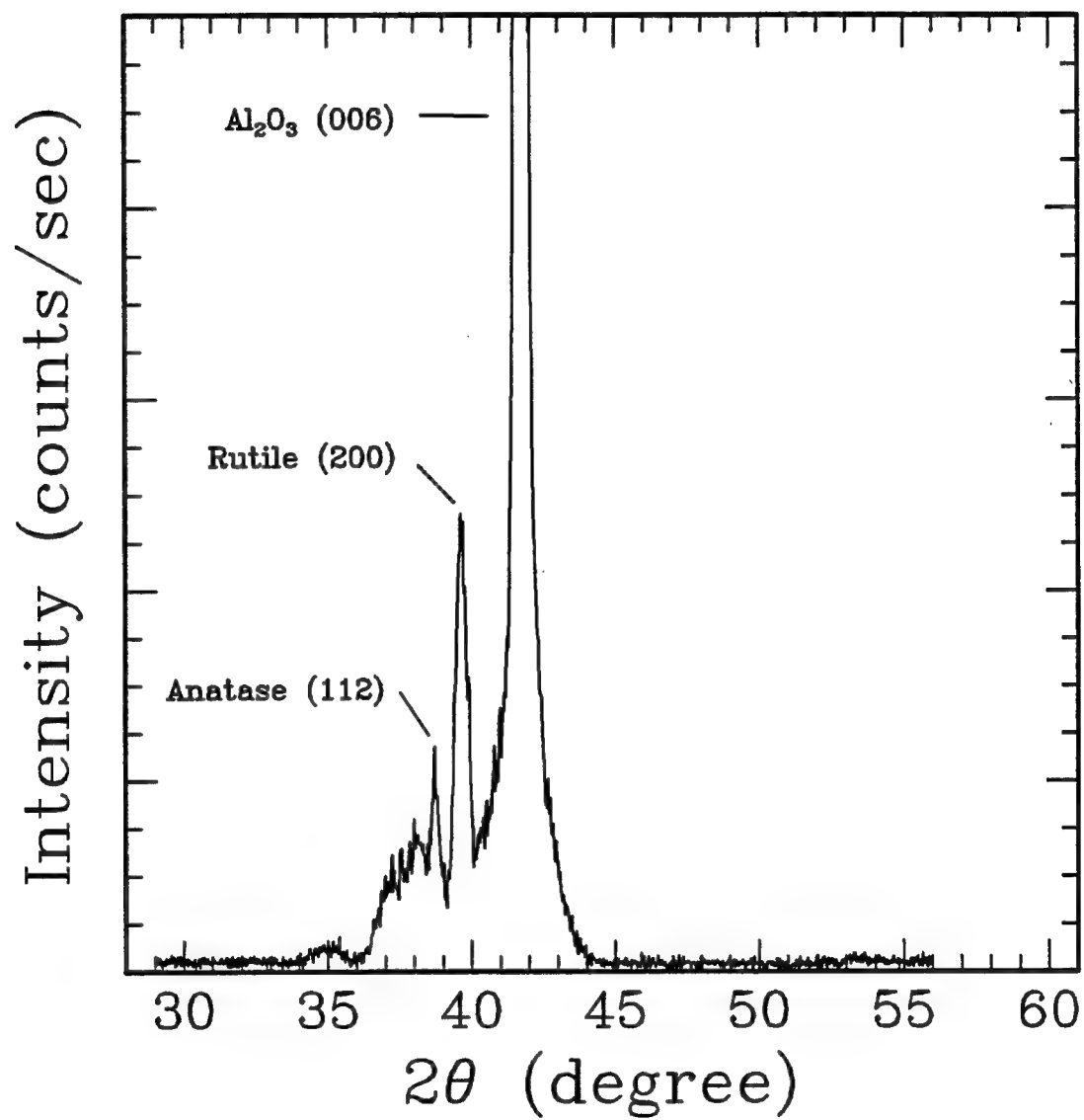
Figure 5.8. X-ray diffraction θ-2θ scan of a thick film deposited at 300°C.
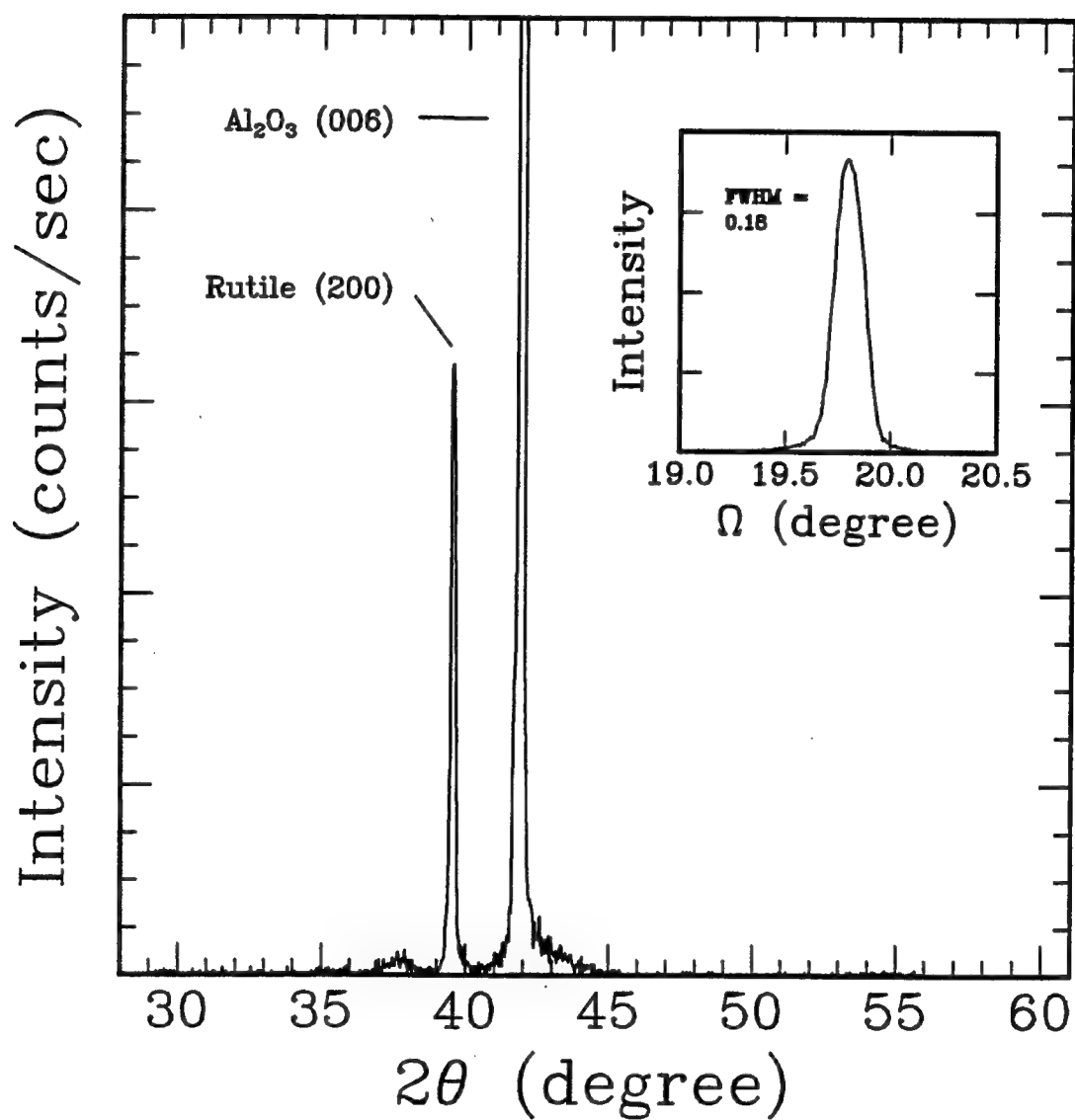
Figure 5.9. X-ray diffraction θ-2θ scan of a thick film deposited at 700°C. The inset is a rocking curve analysis of the rutile (200) film peak with a FWHM of 0.18°.

temperatures ranging from 250° to 650°C, and only the presence of rutile in a film produced at 800°C. They also reported film orientation improved with such surface treatments as removal of carbon and annealing.

5.4 Conclusions

Pyrolysis of titanium isopropoxide precursor was observed to occur above 300°C for as deposited films and in the case of precursor first adsorbed on the substrate, then decomposed by post-deposition annealing. Growth below the pyrolysis temperature shows initial absorption of titanium isopropoxide molecules, then saturation with continued dosing. The stoichiometry of thick films (1000 to 1500 Å) was confirmed to be TiO_2 by XPS. These observations are applied in Chapter 6 to produce controlled submonolayer depositions of TiO_2 on sapphire.

XRD of thick films indicated both anatase and rutile phases present in a film produced at 300°C. In a thick film grown at 700°C, only a rutile film peak was observed. Rocking curve analysis of the film deposited at 700°C gave a peak with a FWHM of 0.18°. The XRD observations agreed with those reported by Chen, et al.[5.7]

5.5 References for Chapter 5

5.1 M. Yokozawa, H. Iwasa, and I. Teramoto, "Vapor Deposition of TiO$_2$," *Jpn. J. Appl. Phys.*, **7**, 96-97 (1968).

5.2 J.P. Lu, J. Wang, and R. Raj, "Solution Precursor Chemical Vapor Deposition of Titanium Oxide Thin Films," *Thin Solid Films*, **204**, L13 -17 (1991).

5.3 S.R. Kurtz and R. G. Gordon, "Chemical Vapor Deposition of Doped TiO$_2$ Thin Films, *Thin Solid Films*, **147**, 167-76 (1987).

5.4 K.L. Siefering and G.L. Griffin, "Kinetics of Low Pressure Chemical Vapor Deposition of TiO$_2$ from Titanium Isopropoxide," *J. Electrochem. Soc.*, **137** [3] 814-18 (1990).

5.5 K.L. Siefering and G.L. Griffin, "Kinetics of CVD Growth of TiO$_2$ Via Decomposition of Tetraisopropyl Orthotitanate"; pp. 219-31 in *Ceramic Transactions: Ceramic Thin and Thick Films*; Vol 11. Edited by B.V. Hiremath. The American Ceramic Society, Inc., Westerville, OH, 1990.

5.6 S. Chen, H.J. Gysling, G.R. Paz-Pujalt, T.N. Blanton, T. Castro, K.M. Chen, C.P. Fictorie, W.L. Gladfelter, A. Franciosi, P.I. Cohen, and J.F. Evans, "UHV-MOCVD Growth and *In Situ* Characterization of Epitaxial TiO$_2$ Films," *Mater. Res. Soc. Symp. Proc.*, **280**, 173-78 (1993).

5.7 S. Chen, M.G. Mason, H.J. Gysling, G.R. Paz Pujalt, T.N. Blanton, T. Castro, K.M. Chen, C.P. Fictorie, W.L. Gladfelter, A. Franciosi, P.I. Cohen and J.F. Evans, "Ultrahigh Vacuum Metalorganic Chemical Vapor Deposition Growth and *In Situ* Characterization of Epitaxial TiO$_2$ Films," *J. Vac. Sci. Technol., A*, **11** [5] 2419-29 (1993).

5.8 J.P. Lu and R. Raj, "Ultra-high Vacuum Chemical Vapor Deposition and *In situ* Characterization of Titanium Oxide Thin Films," *J. Mater. Res.*, **6** [9] 1913-18 (1991).

5.9 S. Baik, D.E. Fowler, J.M. Blakely, and R. Raj, "Segregation of Mg to the (0001) Surface of Doped Sapphire," *J. Am. Ceram. Soc.*, **68** [5] 281-86 (1985).

5.10 S. Baik, "Segregation of Mg to the (0001) Surface of Single Crystal Alumina: Quantification of AES Results," *J. Am. Ceram. Soc.*, **69** [5] C- 101-103 (1986).

5.11   R.C. Sundahl, "Relationship Between Substrate Surface Chemistry and Adhesion of Thin Films," *J. Vac. Sci. Technol.*, **9** [1] 181-85 (1972).

5.12   G.A. Somorjai, *Chemistry in Two Dimensions*; Ch. 2, pp. 39. Cornell University Press, Ithaca, New York, 1981.

5.13   F.S. Ohuchi and M. Kohyama, "Electronic Structure and Chemical Reactions at Metal Alumina and Metal Aluminum Nitride Interfaces," *J. Am. Ceram. Soc.*, **74** [6] 1163-87 (1991).

5.14   M.P. Seah and W.A. Dench, "Quantitative Electron Spectroscopy of Surfaces: a Standard Data Base for Electron Inelastic Mean Free Paths in Solids," *Surf. Interface Anal.*, **1** [1] 2-10 (1979).

5.15   S. Ichimura, H.E. Bauer, H. Seiler and S. Hofmann, "Reduction of Charging in Surface Analysis of Insulating Materials by AES," *Surf. Interface Anal.*, **14**, 250-56 (1989).

5.16   W. Wei, "Reduction of Charging Effects in Auger Electron Spectroscopy," *J. Vac. Sci. Technol., A.*, **6** [4], 2576-81 (1988).

5.17   C.G. Pantano and T.E. Madey, "Electron Beam Damage in Auger Electron Spectroscopy," *Appl. Surf. Sci.*, **7**, 115-41 (1981).

5.18   D.A. Shirley, "High Resolution X ray Photoemission Spectrum of the Valence Bands of Gold," *Phys. Rev. B*, **5** [12] 4709-14 (1972).

5.19   A. Proctor and P.M.A. Sherwood, "Data Analysis Techniques in X-ray Photoelectron Spectroscopy," *Anal. Chem.*, **54**, 13-19 (1982).

5.20   J.F. Moulder, W.F. Stickle, P.E. Sobol and K.D. Bomben, *Handbook of X- ray Photoelectron Spectroscopy.* Edited by J. Chastain. Perkin Elmer Corporation, Eden Prairie, Minnesota, 1992.

5.21   S. Evans, "Curve Synthesis and Optimization Procedures for X-ray Photoelectron Spectroscopy," *Surf. Interface Anal.*, **17**, 85-93 (1991).

5.22   P. Swift, D. Shuttleworth and M.P. Seah, "Appendix 2. Static Charge Referencing Techniques"; pp. 437-44 in *Practical Surface Analysis by Auger and X-ray Photoelectron Spectroscopy.* Edited by D. Briggs and M.P. Seah. John Wiley & Sons, Chichester, 1983.

5.23   J.T. Yates, Jr., P.A. Thiel, and W.H. Weinberg, "The Catalytic Reaction Between Adsorbed Oxygen and Hydrogen on Rh(111),"

Surf. Sci., **82**, 45-68 (1979).

5.24   F. Bozso, G. Ertl, M. Grunze, and M. Weiss, "Interaction of Nitrogen with Iron Surfaces: I. Fe(100) and Fe(111)," *J. Catalysis.*, **49**, 18-41 (1977).

5.25   D. Gonbeam, C. Guimon, G. Pfister Guillouzo, A. Levasseur, G. Meunier, and R. Dornoy, "XPS Study of Thin Films of Titanium Oxysulfides," *Surf. Sci.*, **254**, 81-89 (1991).

5.26   C.N. Sayers and N.R. Armstrong, "X-ray Photoelectron Spectroscopy of TiO_2 and Other Titanate Electrodes and Various Standard Titanium Oxide Materials: Surface Compositional Changes of the TiO_2 Electrode During Photoelectrolysis," *Surf. Sci.*, **77**, 301-20 (1978).

5.27   M.E. Levin, M. Salmeron, A.T. Bell, and G.A. Somorjai, "The Characterization of Ti and Al Oxide Overlayers on Rhodium and Gold By XPS," *Surf. Sci.*, **195**, 429-42 (1988).

Chapter 6
Controlled Submonolayer Depositions of Titanium Dioxide

6.1   Introduction

The ability to produce controlled submonolayer depositions of titanium oxide permits the production of films ranging in thickness from as thin as a submonolayer to monolayers. According to Desu,[6.1] such thin films are useful in ultra large scale integrated devices, Josephson tunnel junctions and high efficient optical filters. The observations from Chapter 5 are applied in this chapter to produce submonolayer growths of TiO_2 from titanium isopropoxide. Molecular monolayer thicknesses of anatase and rutile are defined as 0.33 and 0.31 nm, respectively, in Section 6.3.1.

Desu[5.1] reported the production of TiO_2 films in increments of 0.27 nm by a method called successive layer-wise chemisorption (SLC). Titanium dioxide was produced by cycles of adsorbing $TiCl_4$ on the substrate, followed by reaction with water. The substrates studied were silica and silicon.

The CVD processes producing film growth include precursor adsorption, decomposition and desorption of decomposition products. The observations of Chapter 5 showed these processes can be produced in a distinct stepwise manner by adsorbing titanium isopropoxide on a substrate below the pyrolysis temperature, then post-deposition

annealing above the pyrolysis temperature to decompose the precursor molecules. Decomposition was not observed to be accompanied by desorption of titanium oxide within the detection limits of XPS.

In this chapter, repeated cycles of dosing below and annealing above the pyrolysis temperature were conducted to build up the film thickness. The amount of titanium isopropoxide adsorbed below the pyrolysis temperature was related to a titanium dioxide growth rate per cycle and compared to a theoretical rate. *Ex situ* atomic force microscopy provided topographic images of the thin films produced.

6.2   Experimental procedure

6.2.1   Dose and anneal cycles

The procedures for sapphire preparation and dosing were described in Sections 5.2.1 and 5.2.2, respectively. Film growth in this chapter was produced by heating the substrate to a temperature below the pyrolysis temperature, dosing with titanium isopropoxide for 15 minutes, followed by annealing above the pyrolysis temperature for 10 or 30 minutes. The chamber pressure was maintained at 1×10^{-8} Torr during dosing. A cycle was defined as one dose period followed by one annealing period. The chamber was pumped down between cycles.

Two dose and anneal temperatures were studied. Films were grown by repeated cycles of 60°C doses and 460°C anneals, and 200°C doses and 700°C anneals. The film used to study the effect of isothermal

annealing at 700°C was produced by cycles of 200°C doses and 460°C anneals. Unless noted, experiments in this chapter were conducted on different sapphire pieces.

The substrates used for film growth by 60°C dose and 460°C anneal cycles, and the 700°C annealing experiment showed the presence of tantalum initially by XPS. The substrate used for the film produced by 200°C dose and 700°C anneal cycles (to 208 cycles) initially showed nickel by XPS. The amount of tantalum and nickel were just at the detection limit of the XPS analysis in survey scans. They were due to inadvertent sputtering of the support wires and thermocouple, respectively, during substrate cleaning. Cycle depositions on substrates clean of any surface impurities within the detection limit of XPS showed similar growth rates.

Tables of XPS sensitivity factors are available in the literature. Although such factors should be determined for each spectrometer system, tabulated values provide qualitative trends. According to a table of sensitivity factors,[6.2] the sensitivity of XPS to tantalum and nickel is higher than titanium, oxygen or aluminum. The amount of tantalum or nickel should be very low.

6.2.2 XPS analysis

XPS was performed periodically after several cycles to characterize the deposition. The low energy flood gun was used for the film grown by 60°C dose and 460°C cycles and the film annealed at

700°C. XPS and low energy electron flood gun conditions were described in Section 5.2.5.

Film thicknesses were determined from the XPS Al $2p$ and Ti $2p_{3/2}$ photoelectron peak areas. The terminology used in XPS and AES analysis are not consistently applied in the literature and are briefly discussed here.

The surface sensitivity of electron spectroscopy techniques such as XPS and AES are due to the limited escape depth of emitted electrons. Three terms are used to define this depth. They are inelastic mean free path (IMFP), electron attenuation length (AL), and electron escape depth. Although they have distinct definitions, they are often used interchangeably. These definitions are referred to in Section 6.3.1.

According to the American Society of Testing and Materials (standard E673), the IMFP is "the average distance (in nanometers) that an electron with a given energy travels between successive inelastic collisions."[6.3] The attenuation length is "the average distance that an electron with a given energy travels between successive collisions as derived from a particular model in which elastic scattering is assumed insignificant. With this model, electrons are assumed to be scattered only elastically and predominantly in the forward direction."[6.3] The electron escape depth is "the distance (in nanometers) normal to the surface at which the probability of an electron escaping without significant energy loss due to inelastic scattering processes drops to e-1 (36.8%) of its original value."[6.3]

The IMFP are usually theoretically calculated values. The AL,

typically used in quantitative analysis, are usually determined by experimental techniques in which photoelectron intensity attenuations are determined as a function of overlayer film thickness.[6.4-6] The relation between IMFP and AL are not clearly defined. The AL and escape depth are related by the following relation:

$$escape\ depth = AL\ cos\ \theta \qquad (6.1)$$

where θ is the angle to the surface normal.[6.7]

6.2.3   AFM analysis

Atomic force microscopy was used to produce topographic images of thin films grown by the cycling method. The head used was the D type with a scanning travel range of 15 μm. This head was not calibrated in the z-direction. Quantitative distances in this direction cannot be obtained from the images.

6.3   Results and discussions

6.3.1   Growth by 60°C dose and 460°C anneal cycles

The XPS Al 2p and Ti 2$p_{3/2}$ photoelectron peak areas as a function of number of 60°C dose and 460°C anneal cycles are shown in Figure 6.1. The attenuation and increase in Al 2p and Ti 2$p_{3/2}$ areas,
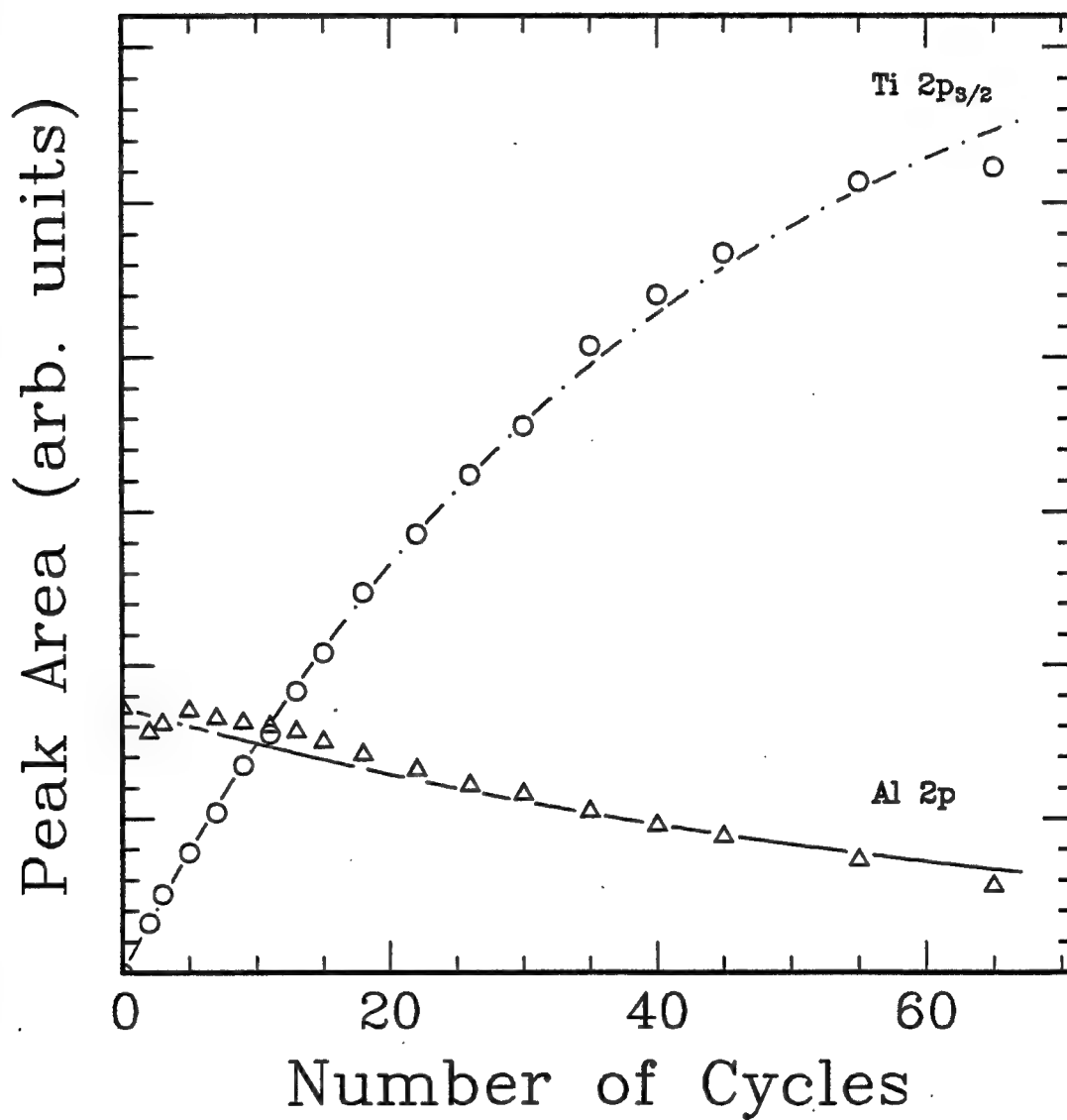
Figure 6.1. XPS Ti $2p_{3/2}$ and Al $2p$ peak areas as a function of number of 60°C dose and 460°C anneal cycles. The lines are non-linear least squares fits to equations from a uniform overlayer model described in the text.

respectively, with increasing number of cycles, indicate titanium oxide was deposited by this method. The annealing segment of the cycles were for 10 minutes.

Film thickness was determined from photoelectron peak areas following the analysis described by Seah and Dench[6.7] and Seah.[6.8,9] The analysis utilizes IMFP of XPS Al $2p$ and Ti $2p_{3/2}$ photoelectrons through a titanium dioxide film, and peak areas from pure bulk standards.

In their analysis, Seah and Dench[6.7] complied what they referred to as experimentally determined IMFP for various electron energies through different matrices. Their work[6.5,6] has been referred to as a compilation of attenuation lengths. The experimentally determined IMFP are actually attenuation lengths according to the ASTM definition. In this work, the term IMFP is used in accordance with Seah and Dench.[6.7]

The IMFP were grouped by elements, organic, and inorganic compounds. Log-log plots of the IMFP as a function of electron energy for each grouping produced so called "universal curves". The plots were generated with the IMFP given in units of nanometers, monolayers, and milligrams per square meter. IMFP in units of monolayers produced less scatter about an empirical fit.

The relation between IMFP, λ_{am} (in atomic monolayer), and electron energy, E (eV), for inorganic compounds is:[6.7]

$$\lambda_{am} = \frac{2170}{E^2} + 0.72 \left(a_{am}E\right)^{1/2} \qquad (6.2)$$

where a_{am} is the atomic monolayer thickness in nanometers. It is determined as follows:[6.7]

$$a_{am}^3 = \frac{A}{\rho \, n \, N} \times 10^{24} \qquad (6.3)$$

where A, ρ, n, and N are the atomic or molecular weight, density (kg/m^3), number of atoms in the molecule, and Avogadro's number. Equation (6.3) defines a monolayer as a thickness equivalent to one atomic layer without structure considerations. Electron energy, E (eV), is determined using the following equation:[6.2]

$$E = h\upsilon - E_{BE} - \phi_s \qquad (6.4)$$

where $h\upsilon$, E_{BE}, and ϕ_s are the photon energy (1253.6 eV for Mg Kα), electron binding energy (eV), and spectrometer work function (5.848 eV), respectively. The E_{BE} of O $1s$, Al $2p$ and Ti $2p_{3/2}$ were taken as 531.0 eV, 74.4 eV and 458.8 eV,[6.2] respectively.

Equation 6.2 is an empirical fit to experimental data and assumes there is insignificant or no elastic scattering.[6.5,6] By grouping the IMFP by elements, organic, and inorganic compounds, it is also assumed there is no energy dependence on the material within each grouping.[6.10]

Table 6.1 shows the IMFP calculated from Equations 6.2 and 6.3, for the XPS O 1s, Al $2p$ and Ti $2p_{3/2}$ photoelectrons through overlayer films with the anatase and rutile phases. The differences between the

Table 6.1. Inelastic Mean Free Paths of Al $2p$, Ti $2p_{3/2}$, and O $1s$ Through Anatase and Rutile[6.7]

IMFP, λ_{am}*	Titanium Dioxide Phase	
	Anatase	Rutile
$\lambda_{am}^{TiO_2}\left(E_{Al\,2p}\right)$	11.7	11.5
$\lambda_{am}^{TiO_2}\left(E_{Ti\,2p_{3/2}}\right)$	9.6	9.4
$\lambda_{am}^{TiO_2}\left(E_{O\,1s}\right)$	9.2	9.0

* IMFP are given in units of atomic monolayers. $E_{Al\,2p}$, $E_{Ti\,2p3/2}$ and $E_{O\,1s}$ refer to the electron energies for Al $2p$, O $1s$ and Ti $2p_{3/2}$ photoelectrons, respectively.

two phases are greatest (2.2%) for the O $1s$ IMFP, and smallest (1.7%)

for the Al $2p$ IMFP. Overall, the differences are not very large.

Converting XPS photoelectron peak areas to film thickness also

requires intensities from bulk standards. Determination of bulk

standard peak areas were described in Section 5.3.4. The intensity of Al

$2p$ was determined from clean sapphire and is referred to as I_∞^{Al}.

Intensity of Ti $2p_{3/2}$ was determined from a thick film of TiO_2 and is

referred to as I_∞^{Ti}. The ratio of I_∞^{Ti} to I_∞^{Al} is 3.43 ± 0.05.

Film thickness can be determined from the following

equations:[6.7]

$$I^{Al} = I_\infty^{Al} \exp\left(\frac{-d_{am} \sec\theta}{\lambda_{am}^{TiO_2}\left(E_{Al\,2p}\right)}\right) \qquad (6.5)$$

$$I^{Ti} = I_\infty^{Ti} \left\{ 1 - \exp\left(\frac{-d_{am} \sec\theta}{\lambda_{am}^{TiO_2}\left(E_{Ti\,2p_{3/2}}\right)}\right)\right\} \qquad (6.6)$$

where I^{Al} and I^{Ti} are the Al $2p$ and Ti $2p_{3/2}$ photoelectron peak areas

respectively, $\lambda_{am}^{TiO_2}\left(E_{Al\,2p}\right)$ and $\lambda_{am}^{TiO_2}\left(E_{Ti\,2p_{3/2}}\right)$ are the IMFP for the Al $2p$ and

Ti $2p_{3/2}$ photoelectrons, respectively, and d_{am} is the overlayer film

thickness in atomic monolayers. Sec θ is taken as $1/\cos\theta = 1/0.74$ for a

CMA analyzer normal to the surface.[6.7] These equations assume a

uniform overlayer of film.

Equations 6.5 and 6.6 can be used individually to determine d_{am}.

They can also be used in conjunction with each other to eliminate

systematic errors in the XPS data collection. The resulting equation is:

$$\frac{\left(\frac{I^{Al}}{I^{Al}_{\infty}}\right)}{\left(\frac{I^{Ti}}{I^{Ti}_{\infty}}\right)} = \frac{\exp\left(\frac{-d_{am}\ \sec\theta}{\lambda^{TiO_2}_{am}\left(E_{Al\ 2p}\right)}\right)}{1 - \exp\left(\frac{-d_{am}\ \sec\theta}{\lambda^{TiO_2}_{am}\left(E_{Ti\ 2p_{3/2}}\right)}\right)} \qquad (6.7)$$

Film thickness is determined from equation 6.7 graphically using the GENPLOT program. For a particular number of dose and anneal cycles, the left hand side (fixed by I^{Al} and I^{Ti}) minus the right hand side (varies with d_{am}) is plotted against d_{am} in increments of 0.02 ranging from 0.1 to 30. The value of d_{am} producing the closest zero value between the left and right side of equation 6.7 is returned as the thickness for a given number of cycles.

Seah and Dench[6.7] defined a monolayer as the thickness of one atomic layer according to equation 6.3. In this work, it is more convenient to define a monolayer as a thickness equivalent to one molecular layer of TiO_2. This is symbolized by a to distinguish it from the atomic monolayer, a_{am}. The molecular monolayer thickness was calculated from equation 6.3 by setting $n=1$ instead of $n=3$. For anatase, a and a_{am} are 0.33 and 0.23 nm, respectively. For rutile, a and a_{am} are 0.31 and 0.22 nm, respectively.

The film thickness, d_{am}, in units of atomic monolayer (aML) is converted to a thickness, d, in units of molecular monolayer (ML) by the following relation:

$$d = d_{\mathrm{am}} \, a_{am} / a \tag{6.8}$$

For a constant growth rate per cycle, Δd_{c}, the film thickness is related to the number of completed cycles, n_{c}, by the following equation:

$$d = \Delta d_{\mathrm{c}} \, n_{\mathrm{c}} \tag{6.9}$$

Film thickness was determined from equations 6.5, 6.6, and 6.7. Figure 6.1 shows nonlinear least squares fits of equations 6.5 and 6.6 drawn over the XPS Al $2p$ and Ti $2p_{3/2}$ data points, respectively. For the Al $2p$ data, the bulk intensity was taken as 8611.5. This was the clean sapphire intensity for the experiment. The Δd_{c} was varied to produce the lowest χ^2. It was determined as 0.09 ML/cycle. The I_{∞}, and Δd_{c} for the Ti $2p_{3/2}$ were varied to produce the lowest χ^2. They were determined to be 34359 and 0.12 ML/cycle. An anatase phase was assumed.

For both XPS photoelectron peaks, the fits from the model proposed by Seah and Dench[6.7] agree well with the experimental data. In Appendix 2, XPS peak intensities are simulated for uniform and island type films for increasing number of cycles and compared. Included is a discussion of the results of applying a uniform model to non-uniform films. An non-uniform film would not follow the attenuations and increases of equations 6.5 and 6.6, respectively. The assumption of a uniform overlayer for the film grown by 60°C dose and 460°C anneal cycles appears to be satisfied.

The average growth rate using equations 6.5 and 6.6 separately

was 0.11 ML/cycle. The Ti $2p_{3/2}$ bulk intensity for the film was unknown. Although bulk intensities were obtained from thick films, they should be used as a ratio to eliminate systematic errors in XPS data collection. The bulk intensity for Ti $2p_{3/2}$ could be higher in one film than another due to changes in XPS operating conditions, i.e., increase in spectrometer electron multiplier voltage.

For the 60°C dose and 460°C anneal cycles, the XPS Al $2p$ and Ti $2p_{3/2}$ photoelectron peak areas were also converted to film thicknesses using equation 6.7. It was assumed the film phase was anatase. The assumption of anatase versus rutile produced small differences in the film thickness. The difference increased with increasing film thickness. The largest difference was 1.7% or 0.13 ML for a 7.47 ML thick anatase film (for 65 cycles). The graphical method used to solve equation 6.7 produced absolute differences between the left and right hand side ranging from 5 x 10-4 to 0.1 and averaging 1.4 x 10-2 ± 2.6 x 10-2.

Film thickness, d, as determined from equation 6.7 is plotted against the number of cycles in Figure 6.2. The thickness ranged from 0.1 to 2.4 nm. A linear least squares fit to the data points produced a slope of 0.11 ± 6 x 10-4 ML/cycle, y-intercept of 0.07 ± 0.02 ML and correlation factor of 0.9998. The linear fit is shown in Figure 6.2 as a line overlaid on the experimental points. The agreement of the determined film thickness with a linear fit indicated the growth satisfied the assumption of uniform overlayer. As discussed in Appendix 2, a non-uniform film is expected to give a poor linear fit.

The experimental growth rate per cycle can be compared to a
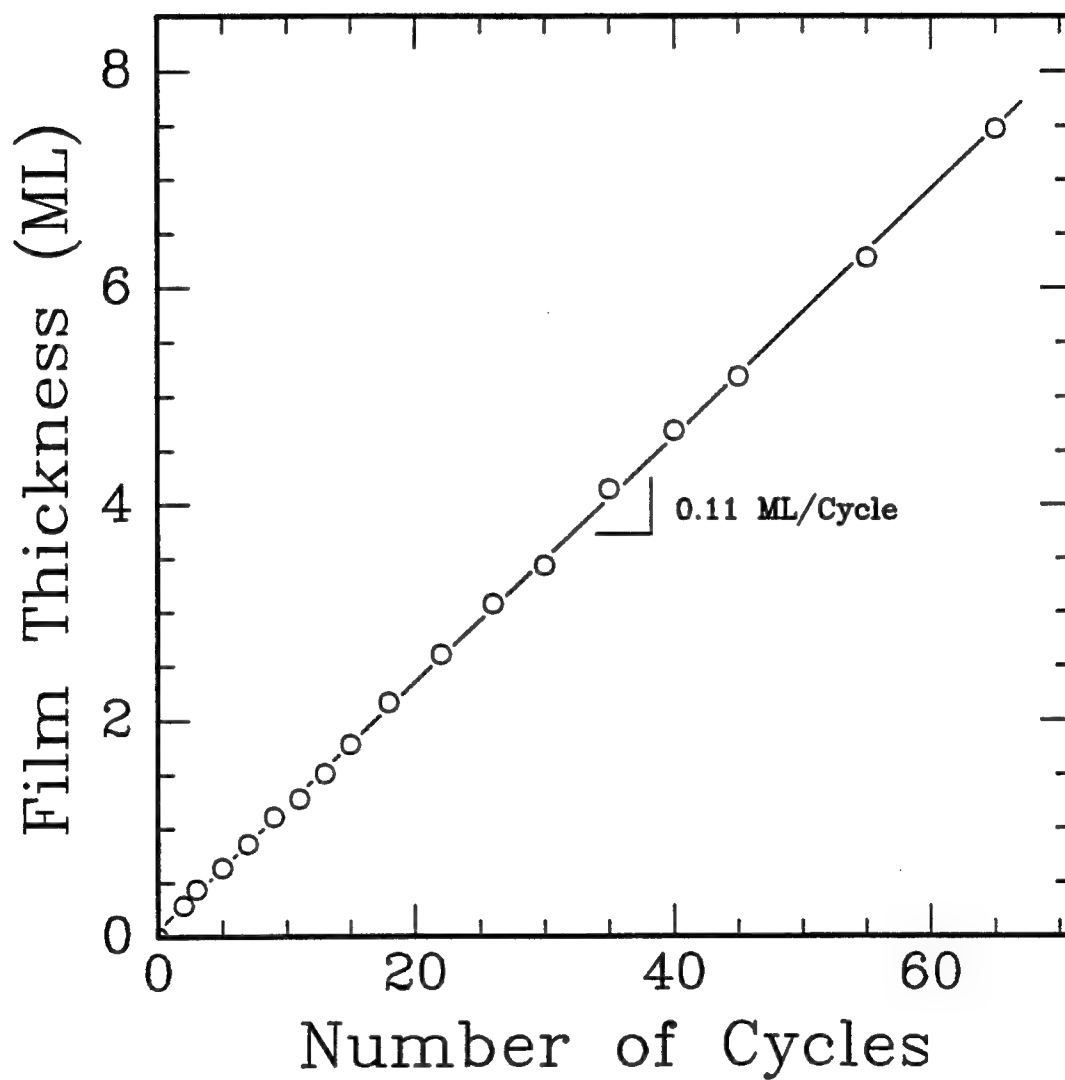
Figure 6.2. Film thickness as a function of number of 60°C dose and 460°C anneal cycles.

theoretical rate. In Chapter 5, it was observed that deposition below the precursor pyrolysis temperature initially showed absorption. If adsorption below pyrolysis during the dose segment of the cycle is limited to one monolayer of titanium isopropoxide molecules, and each molecule of precursor decomposes to one molecule of titanium dioxide, then titanium dioxide growth per cycle can be related to a monolayer adsorption of precursor. This relation is determined from the areal densities of titanium isopropoxide and TiO_2 (rutile and anatase phases).

Areal densities, ρ_A, (Å²/molecule), are given by the following equation:

$$\rho_A = (A / \rho N)^{2/3} \qquad (6.10)$$

where A, ρ, and N were defined earlier for equation 6.3. The molecular weights and bulk densities for titanium isopropoxide and TiO_2 were given in Tables 3.1 and 3.2, respectively. For the precursor, the areal density was estimated using the liquid density.

The areal densities are 62.64 Å²/molecule for titanium isopropoxide, 10.61 Å²/molecule for anatase, and 9.90 Å²/molecule for rutile. A decomposed monolayer of titanium isopropoxide would produce 0.169 or 0.158 monolayers of anatase or rutile, respectively. This calculation is based on ideal packing of titanium isopropoxide molecules and gives an upper limit to the titanium oxide cycle growth rate. The experimentally observed cycle growth rate is below these upper limits.

In Section 5.3.4, the stoichiometry of continuously deposited

thick titanium oxide films were confirmed to be TiO_2. For the thin film grown by 60°C dose and 460°C anneal cycles, the O 1s peak will contain oxygen from sapphire and the interface. The O 1s position for sapphire and TiO_2 are evaluated in Chapter 7. Use of this peak will provide an approximation of the O 1s position for oxygen in the film. Determination of stoichiometry from the separation between Ti $2p_{1/2}$ and Ti $2p_{3/2}$ photoelectron peaks is insufficient. As shown in Table 5.2, TiO_2 and TiO have similar separations. The difference between the Ti $2p$ doublet and the O 1s - Ti $2p_{3/2}$ are 5.62 ± 0.06 eV and 71.98 ± 0.06 eV, respectively. They agree with a stoichiometry of TiO_2.

The film density was not measured directly. However, growth by adsorbing and decomposing one monolayer of titanium isopropoxide at a time, should produce films of higher density than for continuous chemical vapor deposition above the pyrolysis temperature. Sladek and Herron[6.11] reported that desorption of organic groups during decomposition of titanium isopropoxide in continuous depositions produced gaps leading to low density films. Density was increased by annealing.

After 65 dose and anneal cycles, the sample was removed from the chamber. The film thickness was 7.5 ML. *Ex situ* AFM was performed to obtain a topographic image. The picture is shown in Figure 6.3. It shows uniform features with dimensions of approximately 19 nm. These features appear to be grains. This image is compared to a film produced at higher cycle annealing temperature in Section 6.3.2.
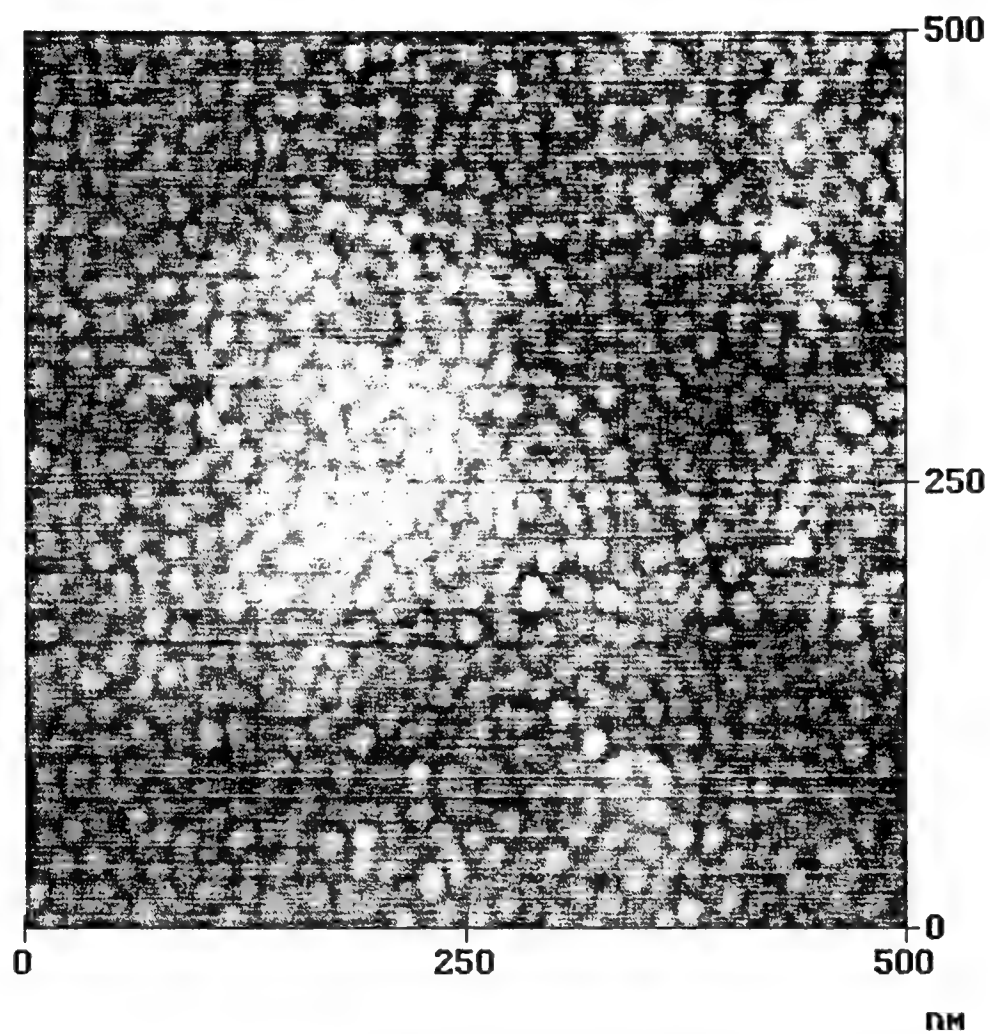
Figure 6.3. AFM of a titanium dioxide film after 65 cycles of 60°C doses and 460°C anneals.

6.3.2   Growth by 200°C dose and 700°C anneal cycles

Growth of titanium oxide was also produced by 200°C dose and
700°C anneal cycles. Figure 6.4 shows the film thickness (ML) as a
function of the number of cycles to 48 cycles. The annealing segment
was 30 minutes per cycle. Film thickness was determined from equation
6.7. An anatase phase was assumed. The increase in film thickness
with cycles indicated film growth by the cycle method. The film
thickness ranged from 0.1 to 2.7 nm.

Growth up to 15 cycles follows a linear relation. A linear least
squares fit from 0 to 15 cycles produced a fit with a slope of 0.15 ± 0.01
ML/cycle, y-intercept of -0.02 ± 0.06 ML and correlation factor of 0.9958.
The fit is shown as a line in Figure 6.4 overlaid on the experimental
points. The growth rate per cycle is below the upper theoretical limits for
anatase and rutile. The experimental and theoretical rates agree within
the uncertainties.

The growth rate per cycle appeared to decrease after 15 cycles
(2.3 ML). The reduction in growth rate cannot be due to reduced
precursor adsorption. If adsorption of precursor changed with film
thickness, it would have been observed in the film grown by 60°C dose
and 460°C anneal cycles. The affect of the annealing step was evaluated
by decreasing the duration from 30 to 10 minutes per cycle. Dose and
anneal cycles were continued until a total of 208 cycles were completed.

Figure 6.5 shows film thickness as a function of number of
cycles with the additional cycles. With the decrease in annealing time,

Figure 6.4. Film thickness as a function of number of 200°C dose and 700°C anneal cycles to 48 cycles. Annealing time was 30 minutes per cycle.
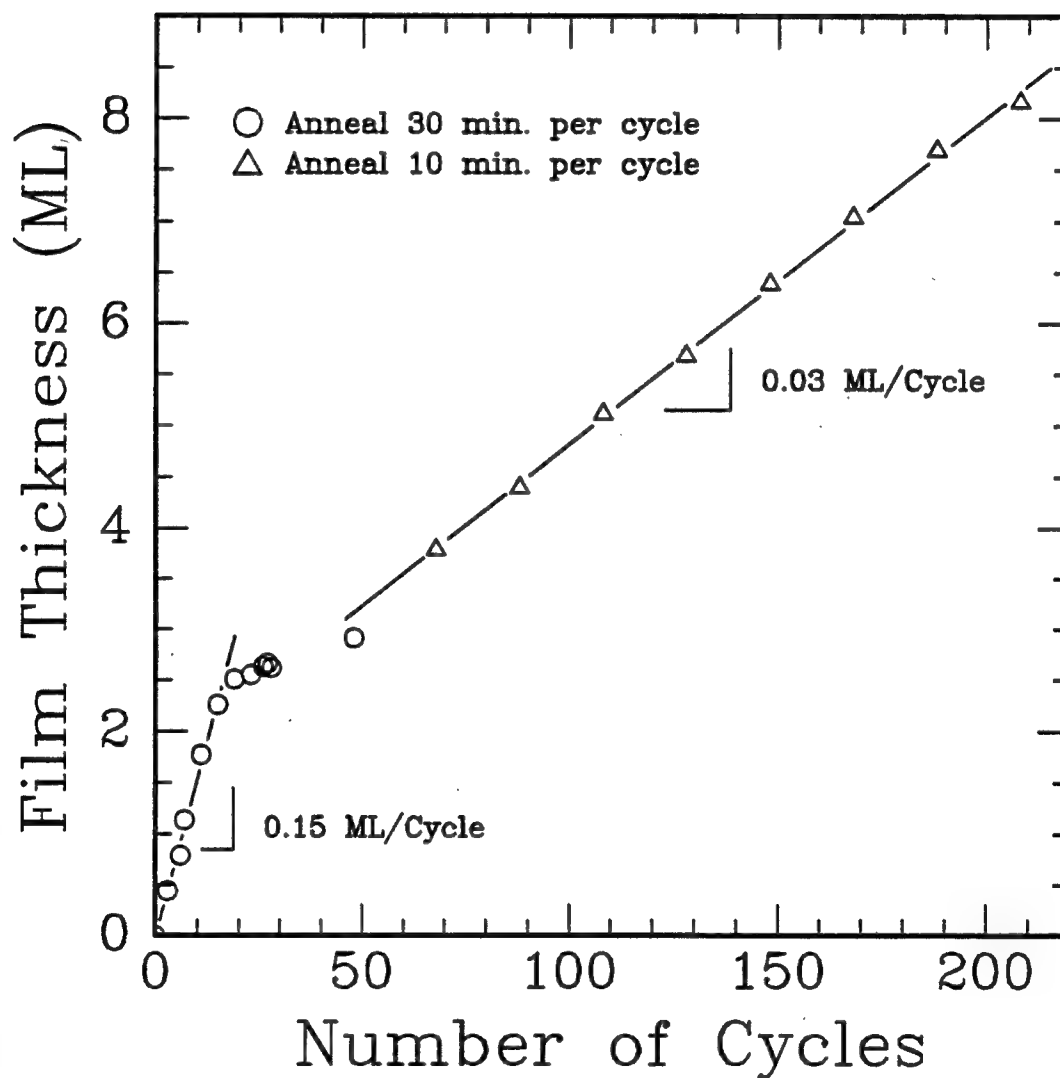
Figure 6.5. Film thickness as a function of number of 200°C dose and 700°C anneal cycles to 208 cycles. Annealing time was 30 minutes per cycle to 48 cycles and 10 minutes per cycle from 49 to 208 cycles.

the growth rate increased and followed a linear relation again. A linear least squares fit from 48 to 208 cycles produced a fit with a slope of $0.03 \pm 5 \times 10^{-4}$ ML/cycle and correlation factor of 0.9993. The fit is shown in Figure 6.5 overlaid on the experimental points.

The affect of annealing time below 15 cycles was evaluated by conducting 200°C dose and 700°C anneal cycles on two other samples. The annealing duration was 10 minutes per cycle. Ten and fourteen cycles were completed. No impurities were initially observed on the substrates within the XPS detection limit. Figure 6.6 shows film thickness as a function of number of cycles (below 48 cycles) for all three experimental runs.

A growth rate of $0.15 \pm 3 \times 10^{-3}$ ML/cycle, y-intercept of $-7 \times 10^{-3} \pm 0.02$ ML and correlation factor of 0.9989 was obtained by a linear least squares fit for the run to 10 cycles. For the run to 14 cycles, a growth rate of 0.17 ± 0.01 ML/cycle, y-intercept of 0.10 ± 0.07 ML and correlation factor of 0.9948 was obtained by a linear least squares fit. Both growth rates agrees within the uncertainties with the rate observed with the 30 minute annealing time (to 15 cycles).

The annealing time per cycle does not affect the growth rate per cycle below approximately 2.5 ML. The affect of annealing at 700°C is further evaluated in Chapter 6.3.3 in an isothermal annealing experiment.

O 1s peaks from the film made by 200°C dose and 700°C anneal cycles (to 208 cycles) contains oxygen from sapphire and film. It is used to approximate the binding energy position of oxygen in the film. The
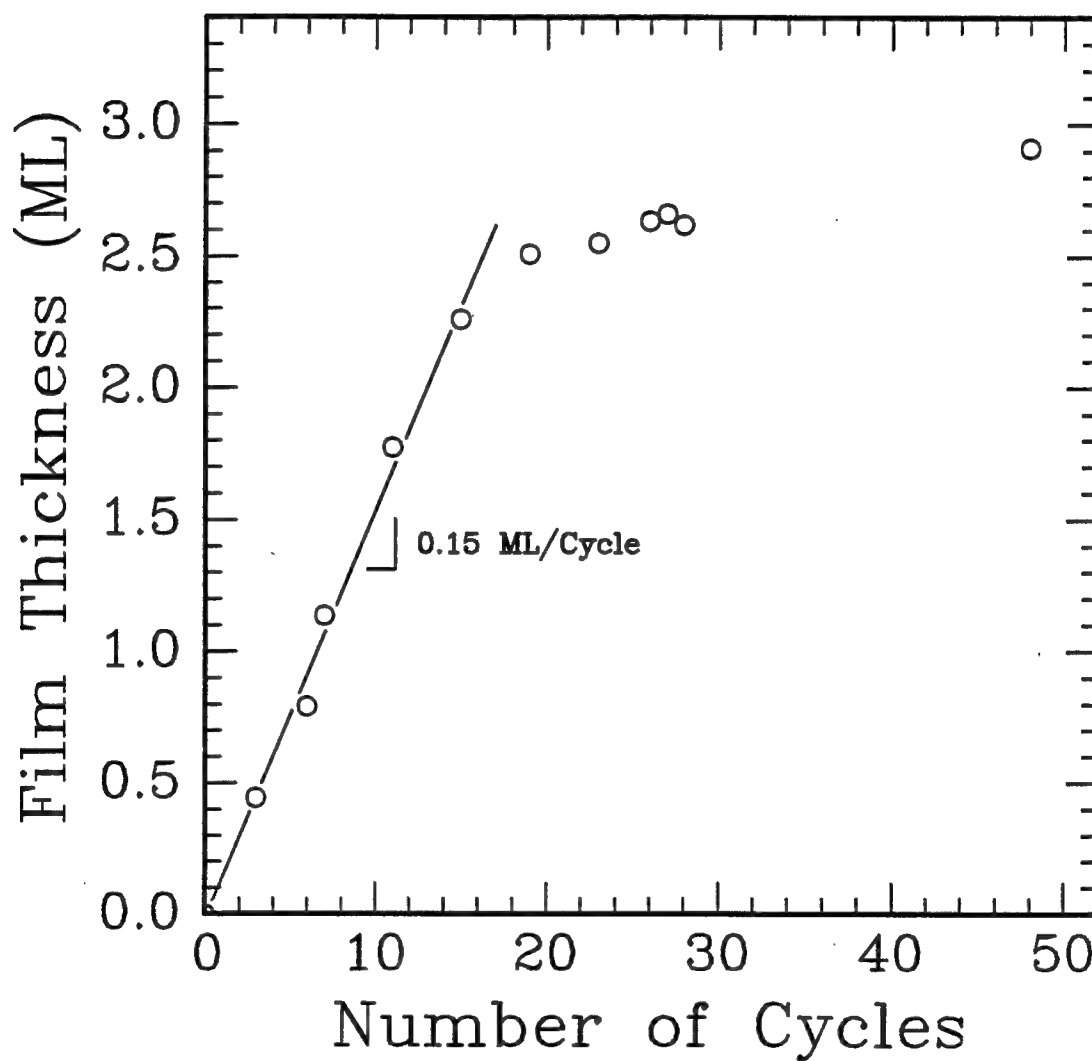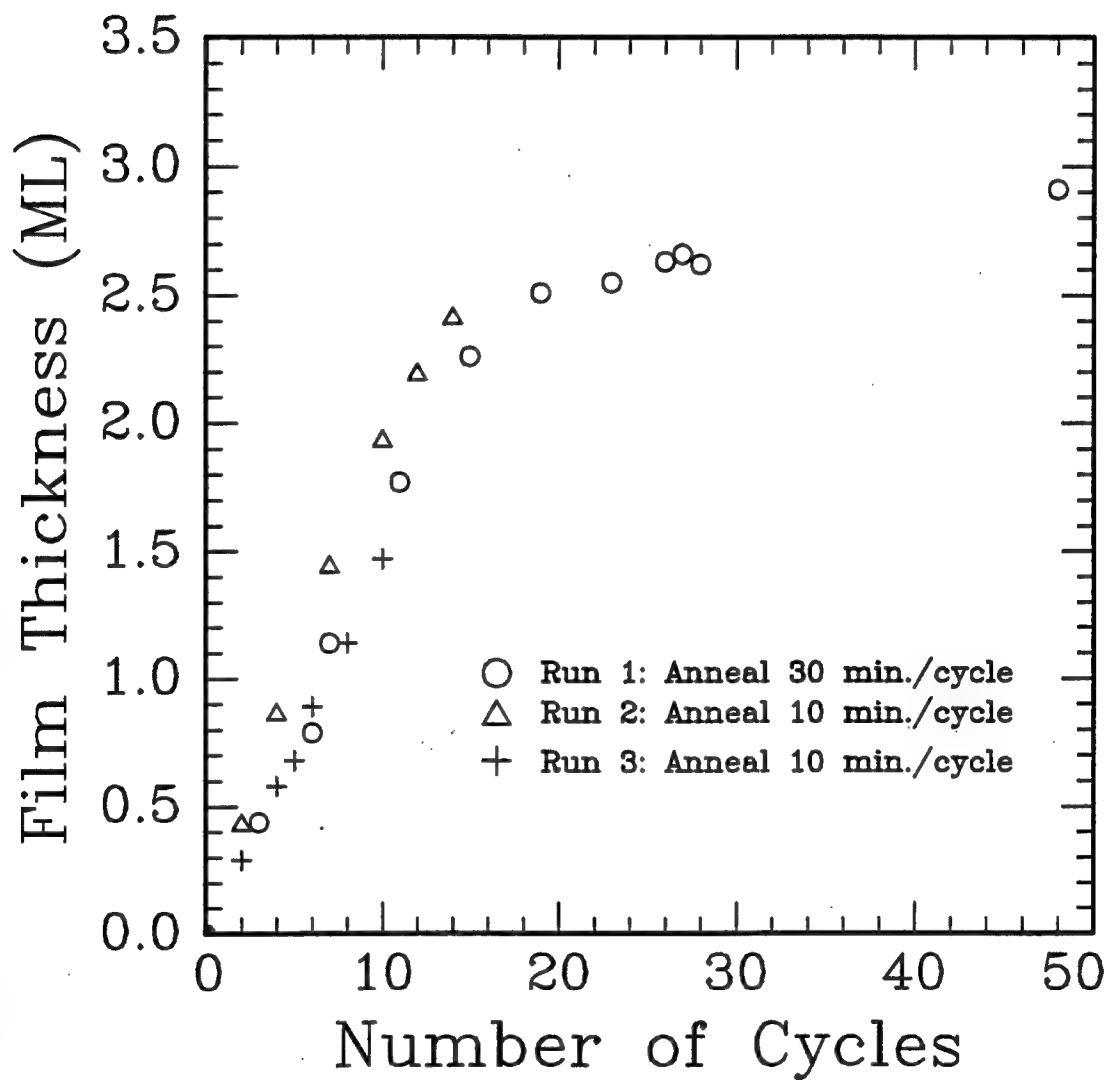
Figure 6.6. Film thickness as a function of number of 200°C dose and 700°C anneal cycles to 48 cycles. Annealing times were 10 and 30 minutes per cycle.

difference between Ti $2p_{1/2}$ - Ti $2p_{3/2}$ and O $1s$ -Ti $2p_{3/2}$ are 5.65 ± 0.06 eV and 72.07 ± 0.06 eV, respectively. These values agree with a stoichiometry of TiO_2.

Figure 6.7 shows an *ex situ* AFM picture taken after 208 cycles of 200°C doses and 700°C anneals were completed. The film thickness is 8.2 ML. The features are uniform and approximately 100 nm in size. These grains are larger than those observed from the 60°C dose and 460°C anneal cycles. The total film thicknesses differ by 0.7 ML.

The linear fits to the film grown by 60°C dose and 460°C anneal cycles, and 200°C dose and 700°C anneal cycles (from 48 to 208 cycles) indicated the films satisfy the assumption of uniform overlayer. However, the AFM images show grain structure. For the case of rutile on sapphire(0001), it has been reported the film forms epitaxially as a mosaic of three variants.[6.12,13] This conclusion was reached after analysis of X-ray diffraction pole figures and RHEED.

If titanium dioxide films form as grains with different orientations, such grains could appear in the AFM images. It is possible for the rutile phase to form by the cycling method used. The predominance of rutile over anatase increases with increased deposition temperature.[6.12] It should also increase with increasing annealing temperature and time. To conclusively determine if the grains are indeed due to orientation variants in the film, transmission electron microscopy (TEM) should be performed to image a cross-sectional view.

Grain size as a function of substrate temperature was reported by Hayashi and Hirai[6.14] for deposition of TiO_2 by CVD of $TiCl_4$ and H_2O.
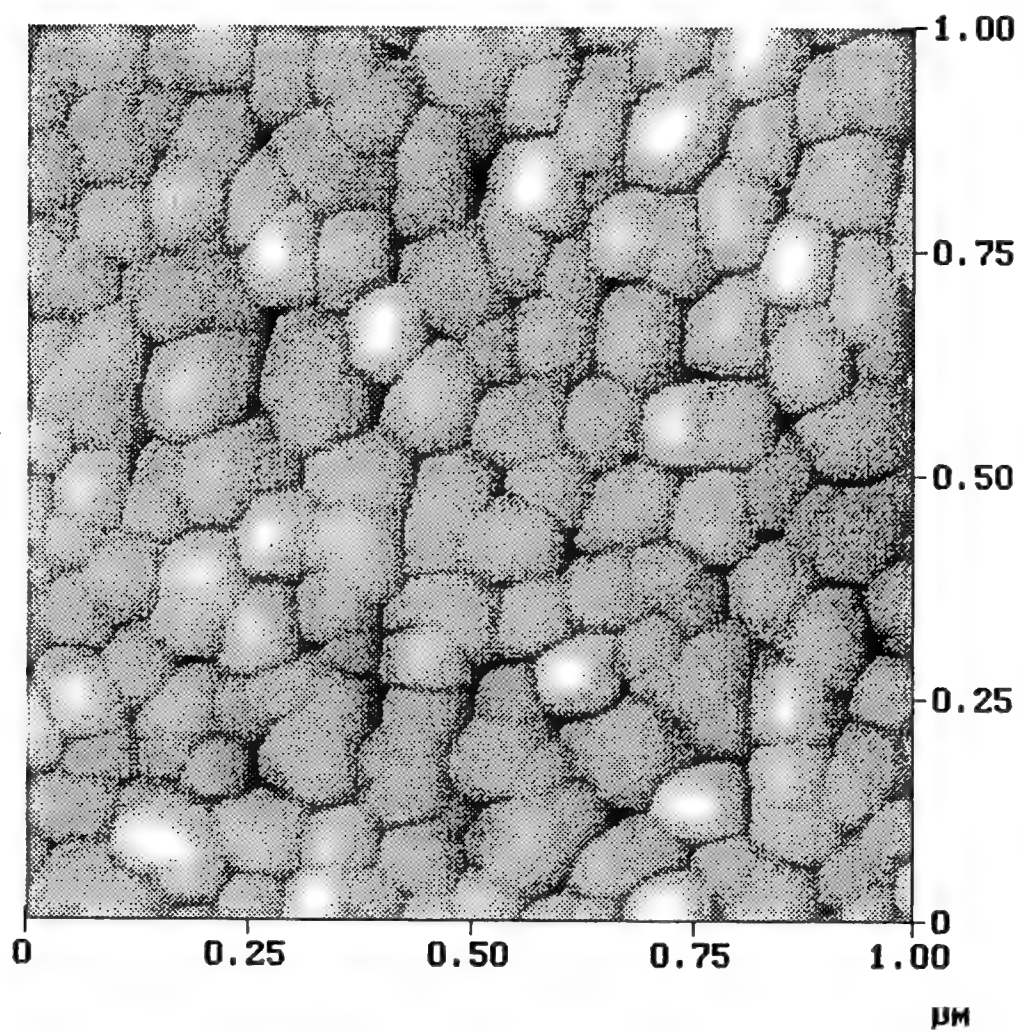
Figure 6.7. AFM of a titanium dioxide film after 208 cycles of 200°C doses and 700°C anneals.

TiO_2 grown at a substrate temperature of 400°C gave grains less than 10 μm. Films grown at 900°C produced 5 μm small grains on 50 μm large grains. It is not clear why there were small grains on larger grains in the 900°C films. Although their grain sizes are much larger than in this work, the larger grain size with higher temperature is consistent. The scale difference may be due to differences in film preparation.

6.3.3   Annealing at 700°C

The effect of isothermal annealing was conducted on a sample in which the film was first deposited by 200°C dose and 460°C anneal cycles to a thickness of 6.1 ML. Two additional cycles of 200°C dose and 700°C anneal cycles were then completed. Annealing duration for all cycles were 10 minutes. The film thickness decreased to 4.0 ML after the two additional cycles. The significant attenuation may be attributed to desorption of film and changes in morphology. Isothermal annealing of the film was then conducted.

Figure 6.8 shows film thickness (ML) as a function of annealing time at 700°C. Film thickness was determined from equation 6.7.[6.7] Up to an annealing time of 160 minutes or 2.91 ML, the film thickness decreased. A linear least squares fit from 0 to 160 minutes gave a slope of $-7.0 \times 10^{-3} \pm 5 \times 10^{-4}$ ML/minute and correlation of 0.9858. The average film thickness from 160 to 370 minutes was 2.97 ± 0.02 ML. The Ti $2p_{1/2}$ - Ti $2p_{3/2}$ and O $1s$ - Ti $2p_{1/2}$ binding energy differences agreed with a stoichiometry of TiO_2 for all thicknesses. The average differences
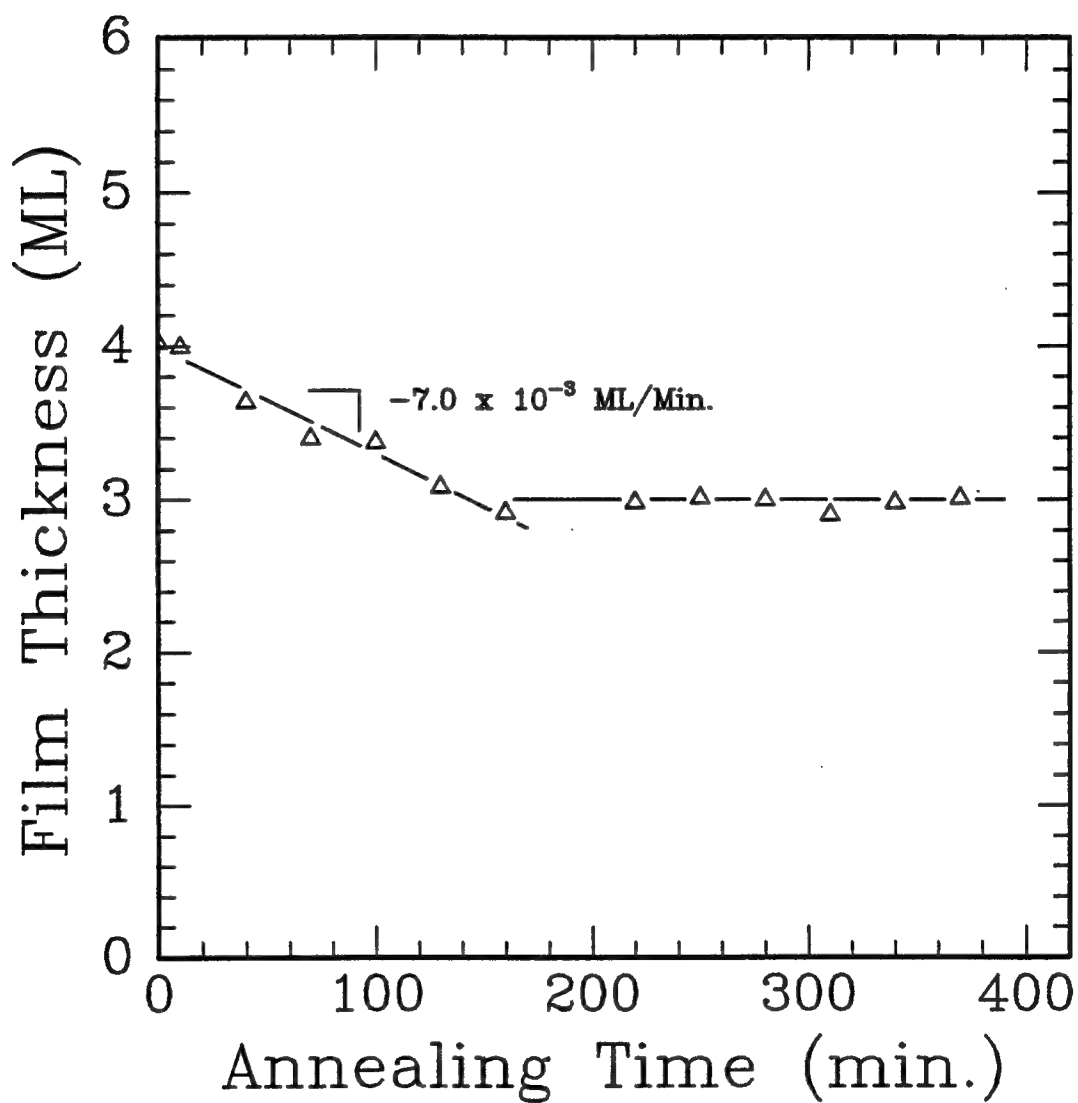
Figure 6.8.   Film thickness as a function of annealing time at 700°C.

was 5.63 ± 0.06 eV and 72.01 ± 0.06, respectively.

The decrease in film thickness to 160 minutes could be explained as due to desorption. It would also confirm and explain the annealing time effect observed with the 200°C dose and 700°C anneal cycles in Section 6.3.2.

Figure 6.9 shows on the same plot, film thickness as a function of annealing time at 700°C, and 200°C dose and 700°C anneal cycles to 48 cycles. If film desorption only occurs above approximately 3 ML, isothermal annealing at 700°C should show thickness loss until 3 ML is reached. In the cycle method of growth, the growth rate should decrease at approximately 3 ML because the annealing segment is now decomposing titanium isopropoxide and desorbing the titanium oxide. In Figure 6.9, the film thickness with number of cycles asymptotically approaches 3 ML. The stable film thickness appears to be approximately 2.5 to 3 monolayers. This suggests bonding of the initial monolayers of film is stronger to sapphire than to itself.

Another possible explanation for the affect of annealing at 700°C is that the film thickness only apparently changes due to changes in film morphology. After 15 cycles, growth by 200°C doses and 700°C anneals occurs in a non-uniform manner. A non-uniform film is promoted by increased annealing time. However, this explanation is not consistent with the observations from isothermal annealing alone. If the apparent decrease in film thickness with annealing is due to island formation, a linear decay is not expected because the model used to determine film thickness assumes a uniform overlayer. The observation
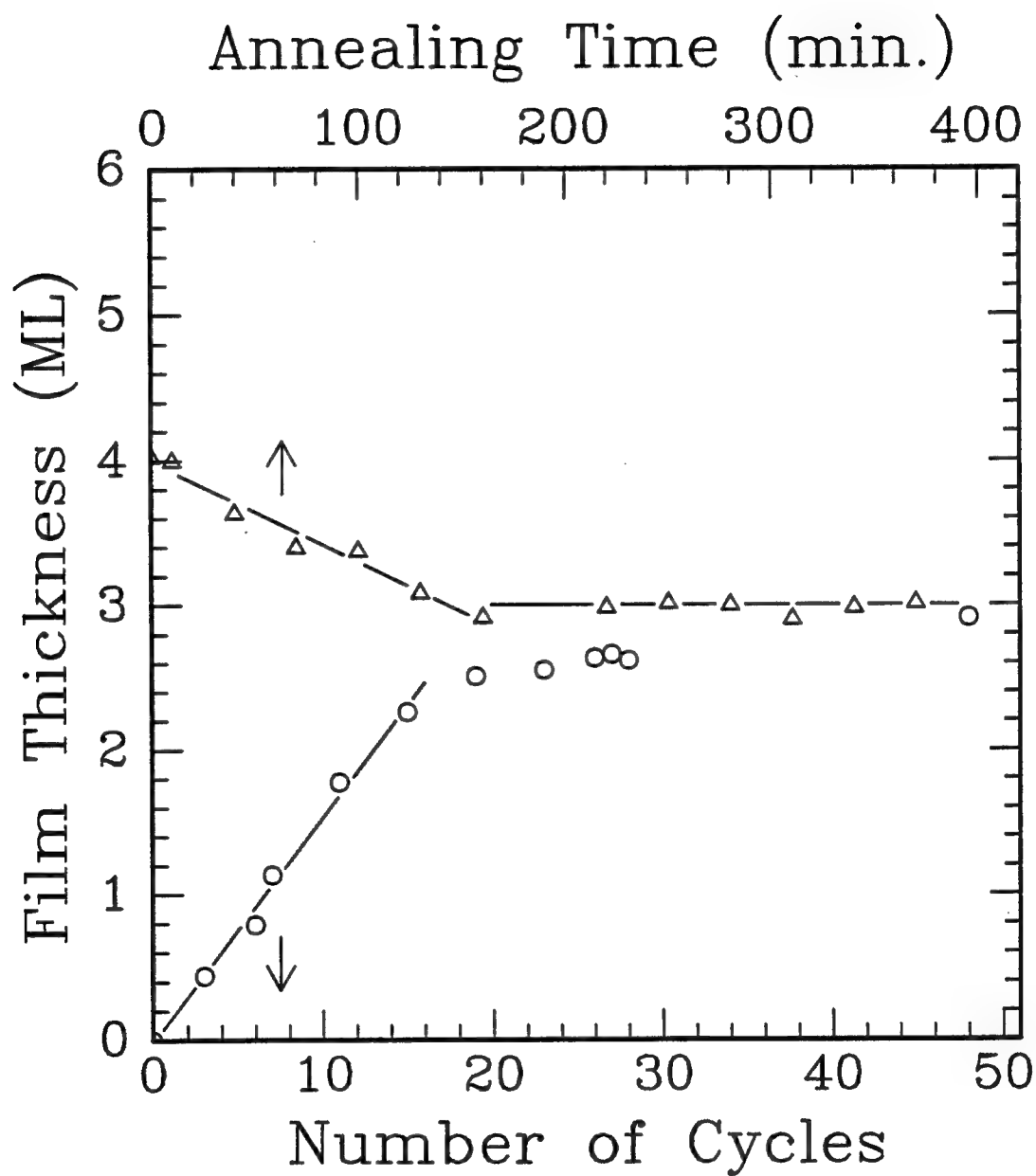
Figure 6.9. Film thickness as a function of annealing time at 700°C, and number of 200°C dose and 700°C anneal cycles to 48 cycles.

of a stable film thickness at 2.5-3 ML for both cycle growth and isothermal annealing is also coincidental if the decrease in film thickness is due to changes in morphology. Film desorption with annealing appears to be the more likely explanation.

The vapor pressure over solid TiO_2 can be calculated from thermochemical considerations. TiO_2 is assumed to sublimate without decomposition according to the following reaction:

$$TiO_2(s) \rightarrow TiO_2(g) \tag{6.11}$$

TiO_2 decomposition due to heating in the 1550° to 1740° C range in molybdenum ovens was reported by Groves, et al.[6.15] However, Berkowitz, et al.[6.16] reported the observed decomposition products can be attributed to reduction of TiO_2 by tantalum crucibles or molybdenum in the experimental setup.

The free energy of formation for the reaction, ΔG_f, is given by:

$$\Delta G_f = \Delta G_f(g) - \Delta G_f(s) \tag{6.12}$$

where $\Delta G_f(g)$ and $\Delta G_f(s)$ are the free energies of formation for gaseous and solid TiO_2, respectively. The vapor pressure is determined from ΔG_f using the following equation:[6.17]

$$\ln P^g = \frac{-\Delta G_f}{RT} \tag{6.13}$$

where P_g, R, and T are the vapor pressure over the solid, gas constant, and temperature, respectively.

The ΔG_f for solid anatase, solid rutile, and gaseous TiO_2 at 700°C are -761.133, -767.182, and -324.673 KJ/mole, respectively.[6.18] The vapor pressures over anatase and rutile at 700°C were calculated to be 2.93×10^{-21} and 1.39×10^{-21} Torr, respectively. These pressures are lower than the chamber base pressure. However, they are vapor pressures for ideal crystals. The presence of dislocations or other defects on the surface would be expected to decrease ΔG_f by decreasing ΔG_f (g) or increasing ΔG_f (s). An decrease in ΔG_f would increase the vapor pressure.

A film growing in a pseudomorphic mode would have dislocations present. In pseudomorphic growth, the initial monolayers of film are strained to match the lattice spacings of the underlying substrate.[6.17] At a particular critical thickness, the film relaxes by the presence of misfit dislocations. The upper misfit limit to pseudomorphic growth has been suggested as 14%.[6.17] As discussed in Section 3.5, the rutile to sapphire misfit is below this limit.

Direct evidence for pseudomorphic growth of TiO_2 on sapphire was not obtained in this work. This type of growth would agree with the observations from annealing at 700°C. Desorption would occur above 3 monolayers if the film forms with misfit dislocations above this thickness and the dislocations promote desorption. A TEM cross-sectional image of the film was not produced and is suggested for future work. The picture would indicate if pseudomorphic growth occurred by

providing information concerning the atom arrangements in the film, and structural relationships between the film and substrate.

6.4   Conclusions

Controlled submonolayers of TiO_2 were produced by dosing the substrate with titanium isopropoxide below the pyrolysis temperature, followed by annealing above the pyrolysis temperature. A growth rate of 0.11 ML/cycle was observed for growth by 60°C dose and 460°C anneal cycles. The experimental growth rate compares well with a theoretical rate. The upper limit growth rate was calculated to be 0.169 and 0.158 ML/cycle for anatase and rutile, respectively. The theoretical calculation assumed adsorption of precursor below the pyrolysis temperature is limited to one monolayer. Each precursor molecule decomposes to form one molecule of titanium dioxide. The final film thickness is determined by the number of cycles completed.

Growth by 200°C dose and 700°C anneal cycles showed below approximately 2.5 ML, the growth rate is unaffected by the annealing time and is 0.15 ML/cycle. Above approximately 2.5 ML, a change in annealing time affected the growth rate. Continuous isothermal annealing of a titanium dioxide film at 700°C produced a decrease in film thickness with annealing time until 3 ML was reached. The changes in growth rate for the film grown by 200°C dose and 700°C anneal cycles, and loss of film with the 700°C continuous annealing can both explained by desorption. This occurs only when the film thickness

is above approximately 2.5 to 3 monolayers.

The stoichiometry of thin films ranging from 0.1 to 2.7 nm was determined to be TiO_2. Isothermal annealing at 700°C was not observed to affect film stoichiometry.

The capability to produce submonolayer depositions permits an *in situ* investigation for reactions at the TiO_2 to sapphire interface. Chapter 7 addresses this issue and evaluates the XPS peak positions in greater detail.

6.5   References for Chapter 6

6.1   S.B. Desu, "Ultra-thin TiO_2 Film by a Novel Method," *Mater. Sci. Eng., B*, **13**, 299-303 (1992).

6.2   J.F. Moulder, W.F. Stickle, P.E. Sobol and K.D. Bomben, *Handbook of X-ray Photoelectron Spectroscopy*. Edited by J. Chastain. Perkin Elmer Corporation, Eden Prairie, Minnesota, 1992.

6.3   "Standard Terminology Relating to Surface Analysis (E673-90)" in *Annual Book of ASTM Standards*. American Society for Testing and Materials, Philadelphia, PA, (1990). Reprinted in *Surf. Interface Anal.*, **17**, 951-58 (1991).

6.4   C.J. Powell, "Attenuation Lengths of Low-energy Electrons in Solids," *Surf. Sci.*, **44**, 29-46 (1974).

6.5   C.J. Powell, "Inelastic Mean Free Paths and Attenuation Lengths of Low-energy Electrons in Solids", *Scanning Electron Microsc.*, **4**, 1649-64 (1984).

6.6   C.J. Powell, "Recent Developments in Quantitative Surface Analysis by Electron Spectroscopy," *J. Vac. Sci. Technol., A*, **4** [3] 1532-39 (1986).

6.7   M.P. Seah and W.A. Dench, "Quantitative Electron Spectroscopy of Surfaces: a Standard Data Base for Electron Inelastic Mean Free Paths in Solids," *Surf. Interface Anal.*, **1** [1] 2-10 (1979).

6.8   M.P. Seah, "Quantification of AES and XPS"; pp. 181-216 in *Practical Surface Analysis by Auger and X-ray Photoelectron Spectroscopy*. Edited by D. Briggs and M.P. Seah. John Wiley & Sons, Chichester, 1983.

6.9   M.P. Seah, "The Quantitative Analysis of Surfaces by XPS: a Review," *Surf. Interface Anal.*, **2** [6] 222-39 (1980).

6.10   C.D. Wagner, L.E. Davis and W.M. Riggs, "The Energy Dependence of the Electron Mean Free Path," *Surf. Interface Anal.*, **2** [2] 53-55 (1980).

6.11   K.J. Sadek and H.M. Herron, "Titanium Dioxide Coatings," *Ind. Eng. Chem. Prod. Res. Develop.*, **11** [1] 92-96 (1982).

6.12   S. Chen, M.G. Mason, H.J. Gysling, G.R. Paz Pujalt, T.N. Blanton, T. Castro, K.M. Chen, C.P. Fictorie, W.L. Gladfelter,

A. Franciosi, P.I. Cohen and J.F. Evans, "Ultrahigh Vacuum Metalorganic Chemical Vapor Deposition Growth and *In Situ* Characterization of Epitaxial TiO_2 Films," *J. Vac. Sci. Technol., A,* **11** [5] 2419-29 (1993).

6.13   K.B. Alexander, F.J. Walker, R.A. McKee, and F.A. List III, "TiO_x/Al_2O_3 Multilayer Ceramic Thin Films," *J. Am. Ceram. Soc.,* **73** [6] 1737-43 (1990).

6.14   S. Hayashi and T. Hirar, "Chemical Vapor Deposition of Rutile Films," *J. Crystal Growth,* **36**, 157-64 (1976).

6.15   W.O. Groves, M. Hoch, and H.L. Johnston, *"Vapor-Solid Equilibria in the Titanium-Oxygen System,"* J. Phys. Chem., **59** 127-131 (1955).

6.16   J. Berkowitz, W.A. Chupka, and M.G. Inghram, *"Thermodynamics of the $Ti-Ti_2O_3$ System and the Dissociation Energy of TiO and TiO_2,"* J. Phys. Chem., **61** 1569-1572 (1957).

6.17   R. Glang, "Vacuum Evaporation"; Ch. 1, pp. 1-10 - 1-69 in *Handbook of Thin Film Technology.* Edited by L.I. Maissel and R. Glang. McGraw-Hill Book Company, New York, 1970.

6.18   M.W. Chase, Jr., C.A. Davies, J.R. Downey, Jr., D.J. Frurip, R.A. Mcdonald, and A.N. Syverud, *JANAF Thermochemical Tables, 3rd Edition, Part II, Cr-Zr.* The American Chemical Society and the American Institute of Physics for the National Bureau of Standards, 1985.

Chapter 7
Titanium Dioxide to Sapphire Interface

7.1   Introduction

The observations of Chapter 6 showed controlled submonolayers of titanium dioxide depositions can be produced and the film thickness determined by the number of dosing and annealing cycles completed. This permits an *in situ* characterization of the film, and film to substrate interface as the overlayer is grown. In this chapter, XPS photoelectron peak shapes and positions are monitored as a function of film thickness for indications of interface reactions.

Film composition as a function of thickness, and the interface between a overlayer and substrate can be studied after deposition by depth profiling. Depth profiling techniques are separated into two categories according to whether the technique is non-destructive or destructive.[7.1-3] The non-destructive techniques include RBS and nuclear reaction analysis (NRA), which have depth resolutions of 50-2000 Å.[7.1-2] The common destructive technique used is sputter depth profiling. The overlayer is gradually removed by ion bombardment and the surfaces characterized by XPS or AES. This technique provides improved resolution (~10 Å).[7.1] The disadvantages of sputter depth profiling includes its destructive nature and difficulties in quantitative analysis due to the sputtering. Sputtering can result in changes in surface topography, changes in composition due to preferential

sputtering, reduction of compounds, and mixing at the interface.[7.1-3] *In situ* analysis of the film and interface as the film is deposited eliminates the potential for sputtering artifacts and sample destruction.

Studies of the interaction between Ti and Al_2O_3 (as sapphire or oxidized aluminum metal)[7.4-10] was reported by several researchers. All reported that titanium reacts at the alumina surface. All but Chaug, et al.[7.4] qualitatively agreed that the titanium reduces the alumina surface to form titanium to oxygen bonds and metallic aluminum. Chaug, et al.[7.4] reported no changes in the sapphire substrate as detected by XPS.

A systematic study of the titanium to sapphire interaction utilizing XPS, TEM, XRD and RBS by Selverian et al., was reported in a series of papers.[7.5-8] Deposition of titanium on sapphire at room temperature produced an additional peak on the low energy side of the XPS Al $2p$ photoelectron peak. Deposition at 1000°C accelerated the reaction. The position of the developing peak indicated the presence of aluminum in a lower valence, metallic state. The peak was detectable at one equivalent titanium monolayer (defined as the amount of overlayer equal to the sapphire(0001) surface atoms)[7.8] and increased with increased film thickness. The thickest film studied was four equivalent monolayers. The titanium formed titanium to oxygen and titanium to aluminum bonds.

7.2   Experimental procedure

7.2.1   Titanium dioxide growth

Titanium dioxide film growth was produced by the dose and anneal cycle method described in Section 6.2.1. The films evaluated were produced by 60°C dose and 460°C anneal cycles, and 200°C dose and 700°C anneal cycles. Growth rate and stoichiometry analysis was discussed in Sections 6.3.1 and 6.3.2.

7.2.2   XPS analysis

XPS spectra collection was detailed in Section 5.2.5. XPS peak positions and areas were obtained from the spectra following the procedures described in Sections 4.5 and 5.2.5. Determination of film thickness from XPS photoelectron peak areas was discussed in Sections 6.3.1 and 6.3.2.

7.3   Results and discussions

7.3.1   Titanium dioxide to sapphire interface

Figures 7.1, 7.2, and 7.3 show the XPS Al $2p$, Ti $2p$, and O $1s$ peaks, respectively, for a film grown by 60°C dose and 460°C anneal cycles. Peaks are shown for film thicknesses of 0, 0.6, 3.1, 5.2, and 7.5
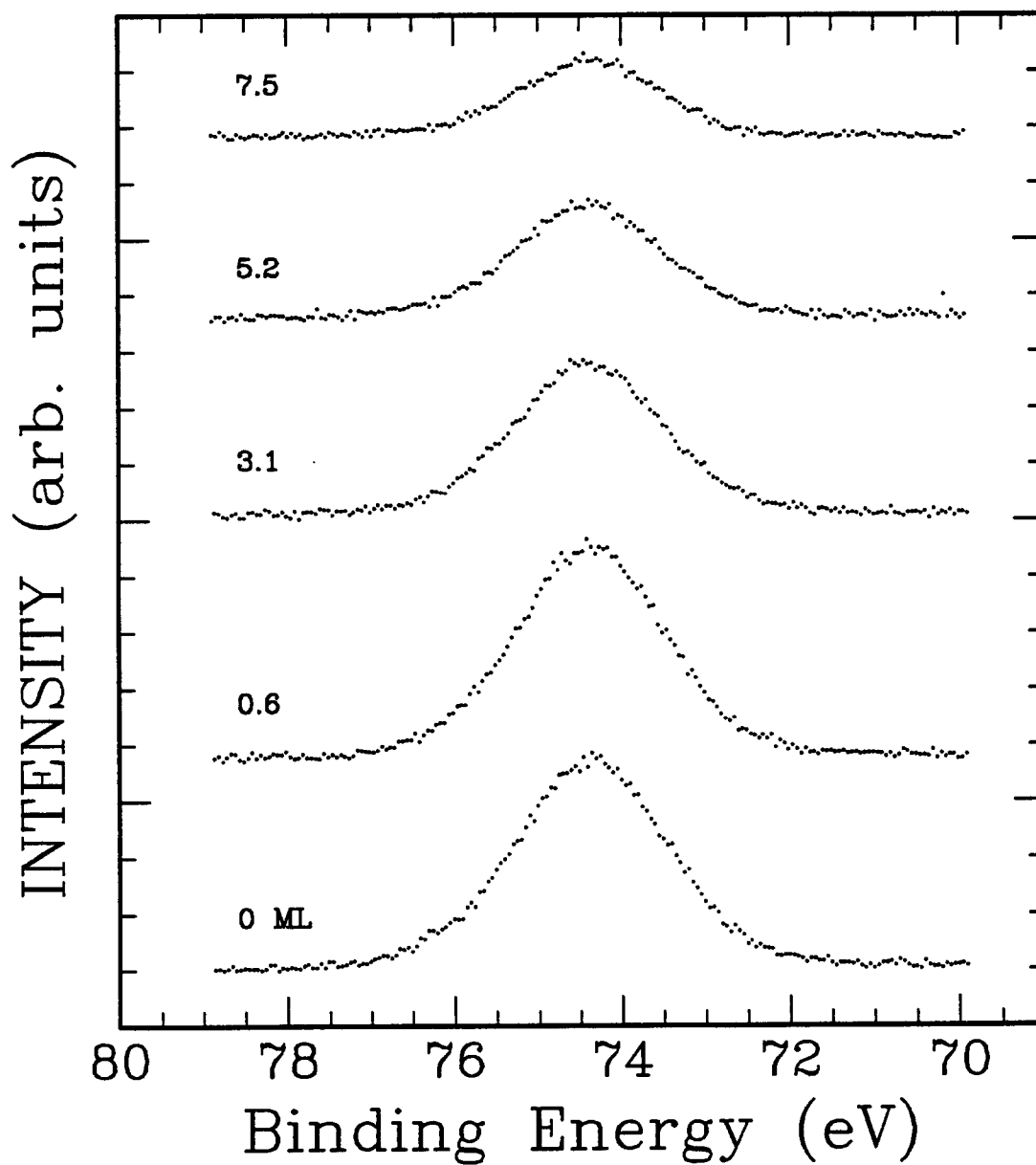
Figure 7.1. XPS Al $2p$ spectra with increasing number of 60°C dose and 460°C anneal cycles. The spectra were positioned at 74.4 eV which corresponds to aluminum bonded to oxygen in sapphire.[7.11]

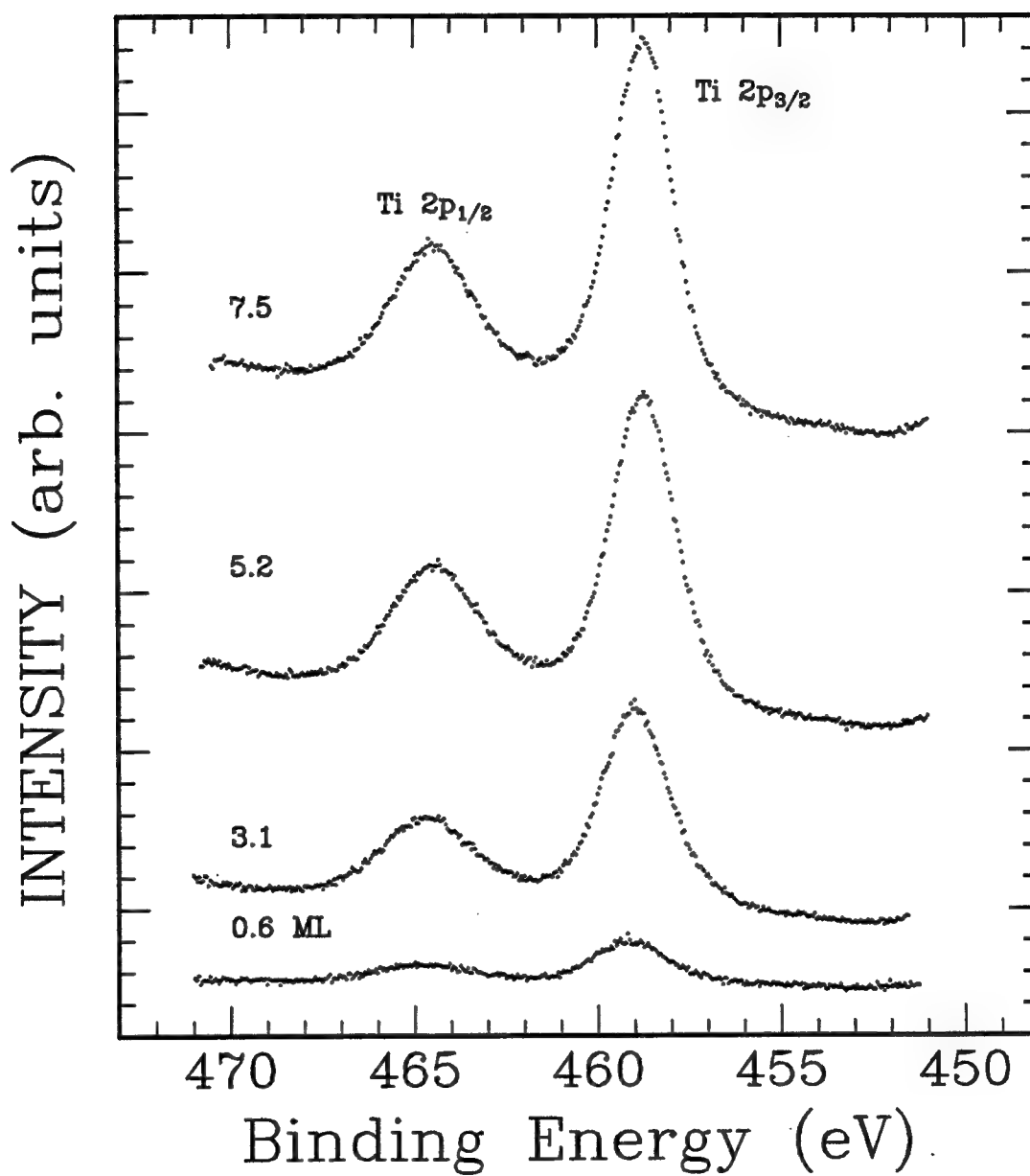**Figure 7.2.** XPS Ti 2*p* spectra with increasing number of 60°C dose and 460°C anneal cycles. The spectra were referenced to Al 2*p* at 74.4 eV.7.11
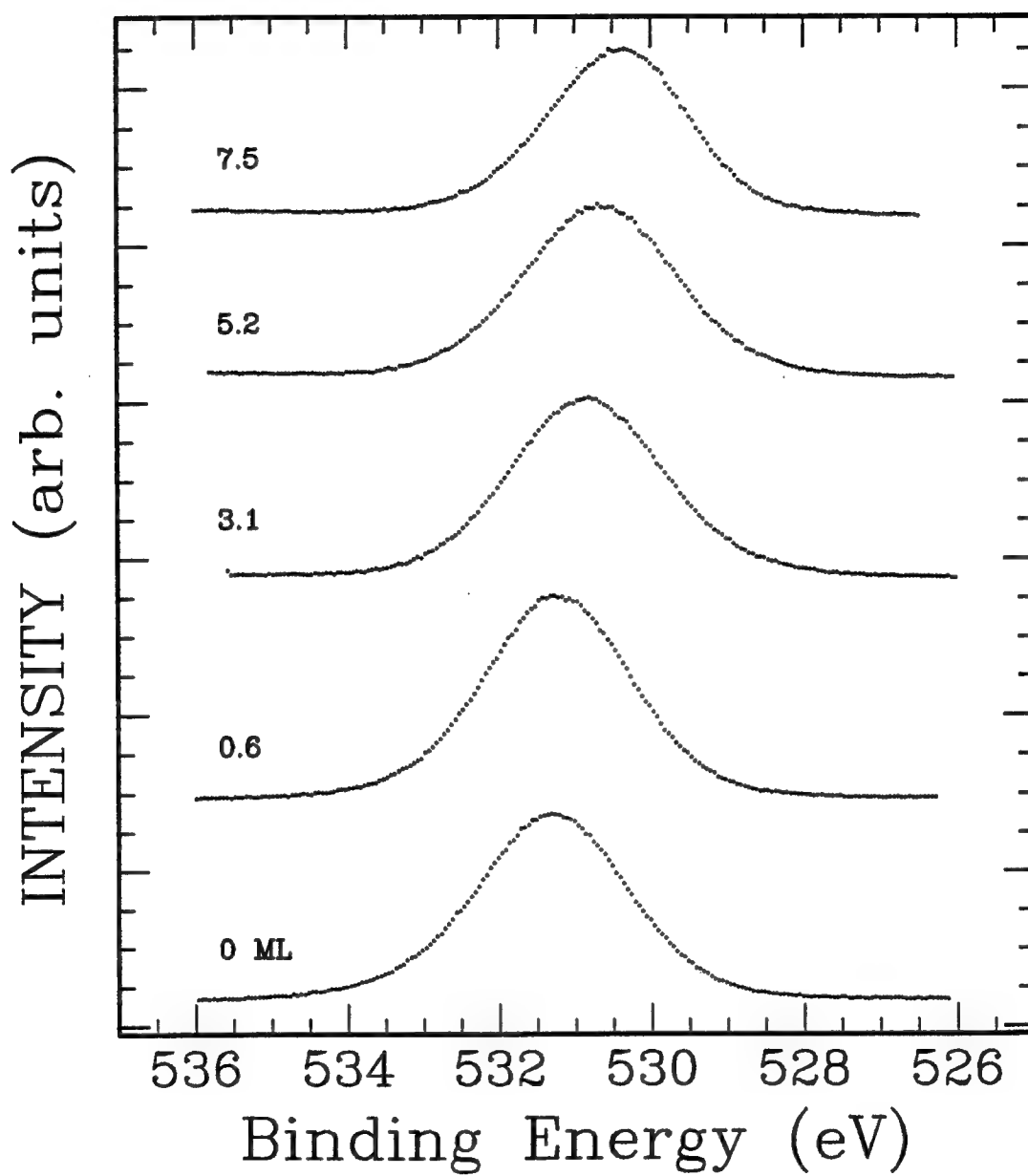
Figure 7.3. XPS O 1*s* spectra with increasing number of 60°C dose and 460°C anneal cycles. The spectra were referenced to Al 2*p* at 74.4 eV.7.11

ML. Although the spectra were collected during use of a low energy flood gun, charging shifted all peaks. The peaks were referenced to Al $2p$ at a binding energy of 74.4 eV.[7.11] This energy corresponds to aluminum bonded to oxygen in sapphire.

A study of the reduction of sapphire surface by titanium was reported to occur at thicknesses as low as a monolayer.[7.5-8] Although the sapphire used in that study was sapphire (1-12), the monolayer definition used was based on the sapphire(0001) surface atomic density. It is not clear if the definition was based on aluminum or oxygen surface density. The film thicknesses shown in Figures 7.1, 7.2, and 7.3 covers the range evaluated in the titanium and sapphire study. The monolayer thickness used here was defined in Section 6.3.1.

Additional peaks developing at the low binding energy side of the Al $2p$ peaks shown in Figures 7.1 were not detected within the detection limit of XPS. Spectra of titanium oxide films grown on sapphire continuously at temperatures of 300°C and 700°C also did not show additional peaks. The lack of sapphire reduction suggests titanium in titanium isopropoxide precursor has sufficient oxygen bonded to it. Additional oxygen from the sapphire surface was not required to form stoichiometric TiO_2. Bonds between the aluminum and oxygen were not broken.

The XPS Ti $2p$ spectra given in Figure 7.2 also do not show additional peaks developing with increased film thickness, within the detection limit of XPS. A Ti $2p_{3/2}$ peak at a binding energy 1.9 eV[7.12] lower than the ones shown would correspond to titanium in Ti_2O_3. Its

presence would suggest titanium replaces the aluminum in the sapphire.[7.5]

The XPS O 1s spectra in Figure 7.3 do not show distinct additional peaks developing with increased film thickness. They show a shift toward lower binding energy with increasing film thickness. Sapphire reduction could not explain these shifts. Evidence for such a reaction was not observed in the Al 2p and Ti 2p spectra.

A possible explanation could be charge transfer at the interface. Observations of charge transfer from a titanium film to sapphire at the interface was reported by Ohuchi and Kohyama.[7.8] A shoulder developed at the low binding energy side of the O 1s peak with increased film thickness. A corresponding feature at the higher binding energy side of the metallic Ti 2p peak was also observed.

Although Figure 7.3 shows the O 1s peak shifts occurs to lower binding energies, corresponding shifts were not observed with the Ti 2p peaks. Shifts in the O 1s persisted and increased with thicker films. In the case of an interface reaction, shifts should be limited to the initial few monolayers.

Evidence of an interface reaction in which titanium oxide reduced the sapphire surface or charge transfer at the interface occurred was not observed within the detection limit of the XPS. The shift in O 1s peak shift could be due to the presence of different binding energy positions for oxygen in sapphire and titanium oxide. This issue is discussed in the following section.

7.3.2 XPS peak shifts

Since charging in XPS prevents determination of absolute
binding energy positions, all peaks must be referenced to one peak. If all
the XPS peaks were referenced to O 1s at 531.0 eV,[7.11] which corresponds
to oxygen in sapphire, the result would be a shift in both the Al 2p and Ti
2p by the same amount toward higher binding energy. Any changes in
the aluminum from a 3+ state, is expected to shift the peak or produce
an additional peak toward lower not higher binding energy. Titanium in
the 4+ state has the highest binding energy among the titanium
oxides.[7.12] Any changes is again expected to shift the peak or produce a
peak at lower binding energy. Using the O 1s as the reference appears
inappropriate.

By referencing all peaks to Al 2p at 74.4 eV, a shift is observed in
the O 1s, but not the Ti 2p. This shift was highly reproducible. It was
observed in all films. They include those grown by cycling depositions
and continuous depositions above the pyrolysis temperature, and
characterization by XPS with and without the use of a low energy
electron flood gun. The stoichiometry of the films grown by the cycling
method and continuous depositions were confirmed to be TiO_2 in
Sections 5.3.4, 6.3.1, and 6.3.2 by the separation between the Ti $2p_{1/2}$ - Ti
$2p_{3/2}$ and O 1s - Ti $2p_{3/2}$ peaks. The constant energy difference between
the Al 2p and Ti 2p peaks suggests titanium and aluminum retain their
4+ and 3+ states, respectively, with increasing film thickness.

The O 1s shift could be due to oxygen from sapphire and the

titanium oxide possessing different binding energy positions. Shifts in the oxygen peak or additional peaks due to differences in binding environment have been reported for the cases of TiO_2 grown on Si[7.13] and Ti on SiO_2.[7.4]

There are several models in the literature for XPS shifts due to changes in the chemical environment.[7.14-17] The binding energies of photoelectrons from a particular species which retains the same oxidation state, should decrease (kinetic energy increases) as the electronegativity of the groups bonded or surrounding it decreases.[7.15,16] The electronegativities of O, Al and Ti are 3.44, 1.61, and 1.54, respectively.[7.18] Oxygen bonded to titanium should have XPS photoelectron peaks with lower binding energy than bonded to aluminum.

The XPS O $1s$ peak will initially reflect oxygen bonded to aluminum. With increasing film thickness, the XPS O $1s$ peak will have a higher oxygen contribution from oxygen to titanium bonds. In a relatively thick film, the O $1s$ peak should only reflect the oxygen to titanium bonds. The binding energy difference between O $1s$ - Ti $2p_{3/2}$ peaks should then be that of TiO_2. This was confirmed by thick films grown at 300° and 400°C in Section 5.3.4.

Figure 7.4 shows estimated O $1s$ peak position shifts as a function of film thickness for the films produced by 60°C doses and 460°C anneals, and 200°C doses and 700°C anneals. A trend of increasing binding energy shift with increasing film thickness is present. The estimated shifts, $\Delta(O\ 1s)_t$, for film thickness t, were determined as
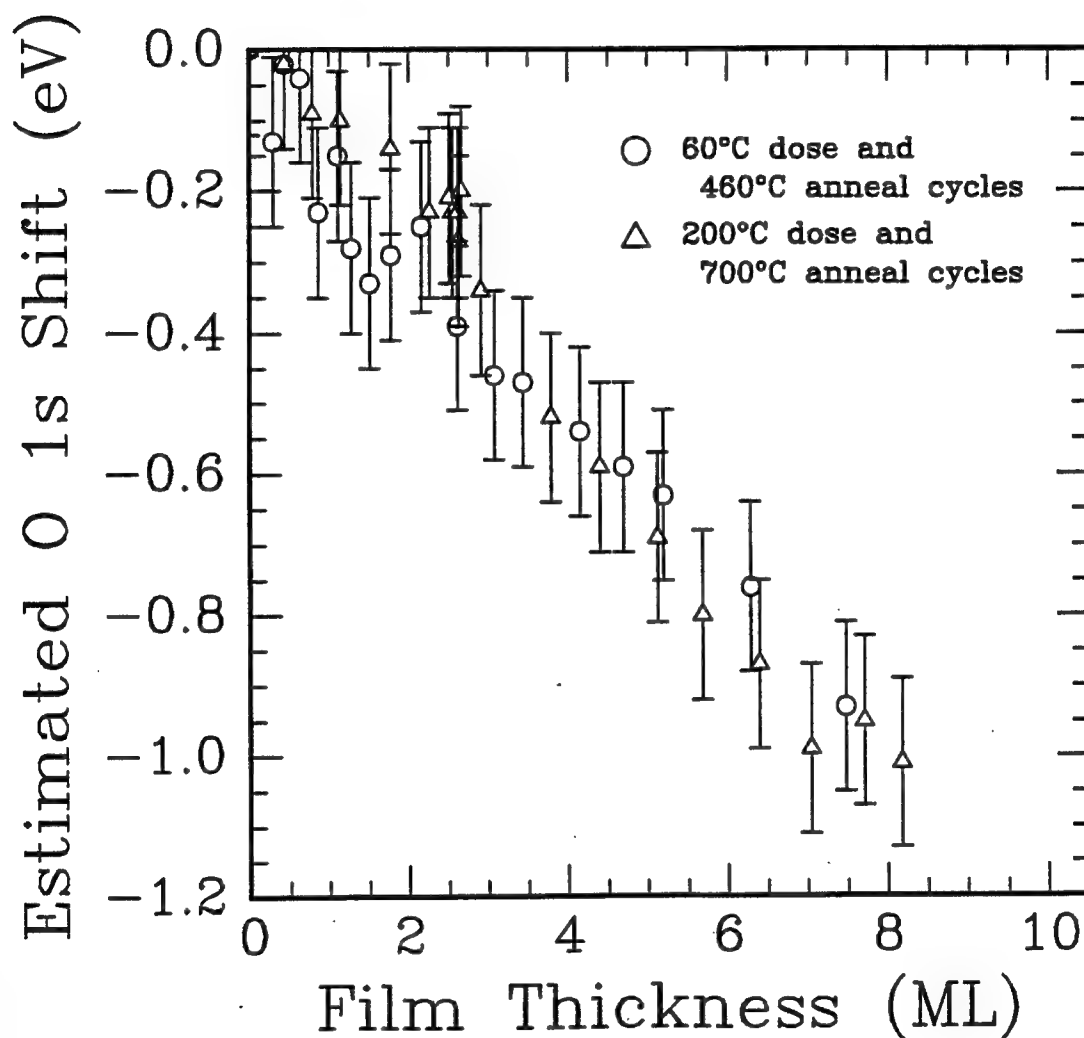
Figure 7.4. Estimated XPS O 1s peak position shifts as a function of film thickness. The thin films were produced by 60°C dose and 460°C anneal cycles, and 200°C dose and 700°C anneal cycles.

follows:

$$\Delta(\text{O } 1s)_t = (\text{O } 1s \text{ - Al } 2p)_t - (\text{O } 1s \text{ - Al } 2p)_o \qquad (7.1)$$

where $(\text{O } 1s \text{ - Al } 2p)_t$ is the difference for t, and $(\text{O } 1s \text{ - Al } 2p)_o$ is the initial difference for sapphire without depositions. Equation 7.1 uses the Al $2p$ peak as the reference.

Peak positions can be determined by visual inspection, curve fitting to the symmetric Gaussian - Lorentzian function discussed in Section 4.5.3, or taken as the binding energy at maximum height intensity. The O $1s$ peak positions for the thin films used in equation 7.1 were determined by visual inspection. The uncertainty is estimated to be $\pm$ 0.1 eV. Peak positions for the O $1s$ from sapphire without depositions, and Al $2p$ were determined by curve fitting to the Gaussian - Lorentzian function. As discussed in Section 4.6, the uncertainty in peak positions for the Al $2p$ was determined as 0.04 eV. Propagation of uncertainties from the O $1s$ and Al $2p$ positions gives an uncertainty of 0.12 eV for the estimated O $1s$ shifts determined from equation 7.1.

Several of the O $1s$ peaks from the thin films possess slight asymmetry. Application of a symmetric curve fitting function to these peaks produces approximations of peak positions. The maximum differences between the symmetric curve fitted positions and asymmetric experimental positions determined by visual inspection was 0.15 eV. The asymmetry of the thin film O $1s$ peaks were not observed in Al $2p$ and Ti $2p$ peaks, and O $1s$ peaks from clean sapphire and bulk

TiO_2. Positions for these peaks were determined from curve fitting. Using the binding energy at maximum height intensity as the peak position is appropriate for smooth peaks. Experimental data are not smooth due to random error. Scatter in experimental data can produce maximum intensities which are not at the peak position.

Determination of the total shift was made by three methods. The first was from thick film experimental data. The second method was by compiling literature reports of relevant XPS binding energy positions and re-referencing them to a common peak to obtain an estimate of the total shift. The final method was by simulation of the O 1s shift with increasing film thickness for the thin films. The total shifts obtained were compared.

The total shift can be determined experimentally from thick films grown at 300° and 400°C. Additional details regarding these films were presented in Section 5.3.4. The total shift from thick films was determined using the following equations:

$$\Delta \text{(O 1}s\text{)}_{Tot.} = [\text{(O 1}s \text{ - Ti } 2p_{3/2}) + D]_f - \text{(O 1}s \text{ - Al } 2p)_0 \qquad (7.2)$$

$$D = \text{Ti } 2p_{3/2} - \text{Al } 2p \qquad (7.3)$$

where the O 1s and Ti $2p_{3/2}$ peaks in the $[\text{(O 1}s \text{ - Ti } 2p_{3/2}) + D]_f$ are from XPS spectra where the Al $2p$ was not observed. D is a constant and was determined from the cycling experiments to be 384.53 ± 0.02 eV. The total O 1s shift from Al_2O_3 to TiO_2 for the 300° and 400°C films were calculated

to be -1.07 $\pm$ 0.08 and -1.19 $\pm$ 0.08 eV, respectively. These two values agree with each other within the uncertainties.

Table 7.1 shows a compilation[7.11,12,19-22] of reported XPS binding energy positions for O $1s$, Ti $2p_{3/2}$, and Al $2p$ as measured from different compounds. The literature sources gave the peak positions referenced to C $1s$. In order to provide a standard for comparing the positions, all peaks in Table 7.1 were re-referenced to a C $1s$ peak at 284.5 eV.[7.11] The compilation was used to estimate the total O $1s$ shift and D. They are estimates because the XPS peak positions were collected from different spectrometers and under various conditions. However, they provide a range to compare experimental values against.

The total O $1s$ shift from O to Al bonding in sapphire to O to Ti bonding in TiO_2 was estimated from the table to range from - 0.8 eV (Sayers, et al.[7.12] - PE, 1992[7.11]) to -1.5 eV (Gonbeau, et al.[7.22] - Madey, et al.[7.19]). The experimentally determined total shift for thick films agrees within this range. D ranged from 384.1 eV[7.11] to 384.4 eV [7.21] for aluminum in single crystal alumina. The experimentally determined D agrees within its uncertainties with this range.

O $1s$ shifts as a function of film thickness for thin films were simulated by assuming interface interaction did not occur. An O $1s$ peak was simulated for oxygen in O to Al bonds. The peak decreased in intensity with increasing film thickness. Similarly, a peak was simulated for oxygen in O to Ti bonds. This peak increased in intensity with increasing film thickness. For each thickness, the two peaks separated by a constant total shift, were added together to form a

Table 7.1. Compilation of Literature XPS O $1s$, Al $2p$, and Ti $2p_{3/2}$ Photoelectron Peak Positions*

Authors	Material**	O 1s	Al 2p	Ti 2p$_{3/2}$
Moulder, et al.[7.11]	TiO_2			458.5
	Al_2O_3		74.4	
	Al_2O_3 (sc)	531.0		
Madey, et al.[7.19]	Al_2O_3 (pd)	531.04	74.17	
Olefjord, et al.[7.20]	Al_2O_3 (ox)	531.4	71.7	
Cocke, et al.[7.21]	TiO_2			458.9
	Al_2O_3 (am)		73.8	
	Al_2O_3 (sc)		74.5	
Gonbeau, et al.[7.22]	TiO_2 (pd)	529.9		458.6
Sayers, et al.[7.12]	TiO_2 (sc)	530.2		458.7

* All peak positions have been re-referenced to C $1s$ at 284.5 as recommended in the *Handbook of X-ray Photoelectron Spectroscopy.*[7.11]

** (sc) = single crystal, (pd) = powder, (am) = amorphous, and (ox) = oxidized Al.

composite peak. The composite peak positions and shapes were compared to experimental peaks. The composite peak positions were determined as the binding energy at maximum height. Simulations were produced for a range of total O $1s$ shifts and thicknesses. Additional details describing the simulation procedure is provided in Appendix 3.

Figure 7.5 shows simulated and estimated experimental peak shifts as a function of film thickness for the film produced by cycles 60°C doses and 460°C anneals. Simulated shifts were generated for total shifts of -0.99 , -1.07, and -1.15 eV. The shifts were determined as the difference in binding energy positions between the composite peak for a particular t and the peak for sapphire without depositions. The simulations show a trend of increasing shift with increasing film thickness.

Figure 7.6 shows the simulated and estimated experimental shifts as a function of film thickness for the film produced by 200°C doses and 700°C anneals. The simulations were produced for total shifts of -1.07, -1.15, and -1.23 eV. Within the uncertainties, the experimental shifts agree with the simulated shifts for the range of total shifts shown.

Experimental peaks from the film grown by 60°C dose and 460°C anneal cycles are shown in Figures 7.7, 7.8, and 7.9 overlaid with simulated peaks for thicknesses of 0, 0.6, 3.1, 5.2, and 7.5 ML. The simulated peaks in Figures 7.7, 7.8, and 7.9 were created for total shifts of -0.99, -1.07, and -1.15 eV, respectively. The dots represent experimental peaks after background subtraction. The dash-dash, dot-dash, and solid lines represent the oxygen from O - Al bonding, O - Ti
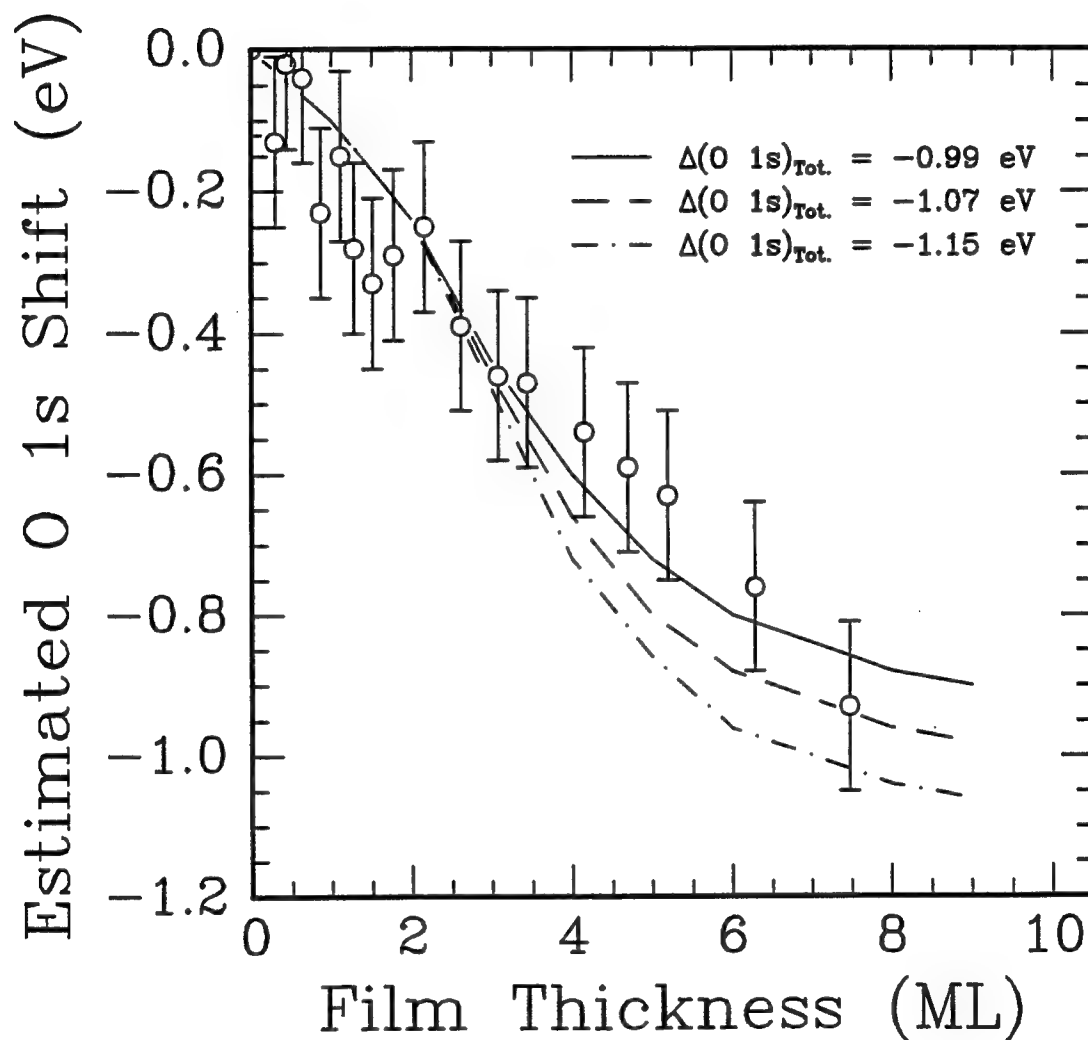
Figure 7.5. Estimated experimental and simulated O 1s peak shifts for total shifts of -0.99, -1.07, and -1.15 eV. The film was produced by 60°C dose and 460°C anneal cycles.
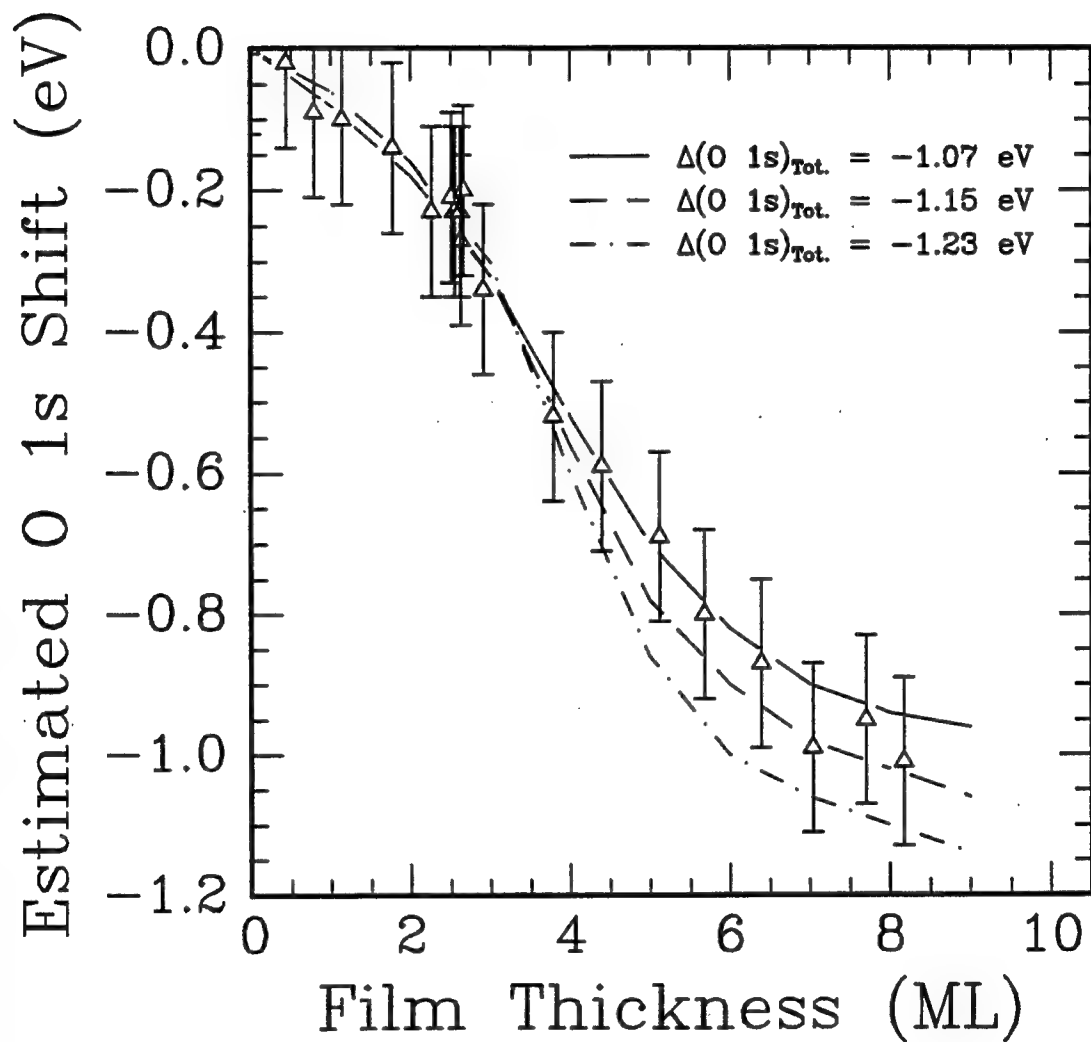
Figure 7.6. Estimated experimental and simulated O 1s peak shifts for total shifts of -1.07, -1.15, and -1.23 eV. The film was produced by 200°C dose and 700°C anneal cycles.
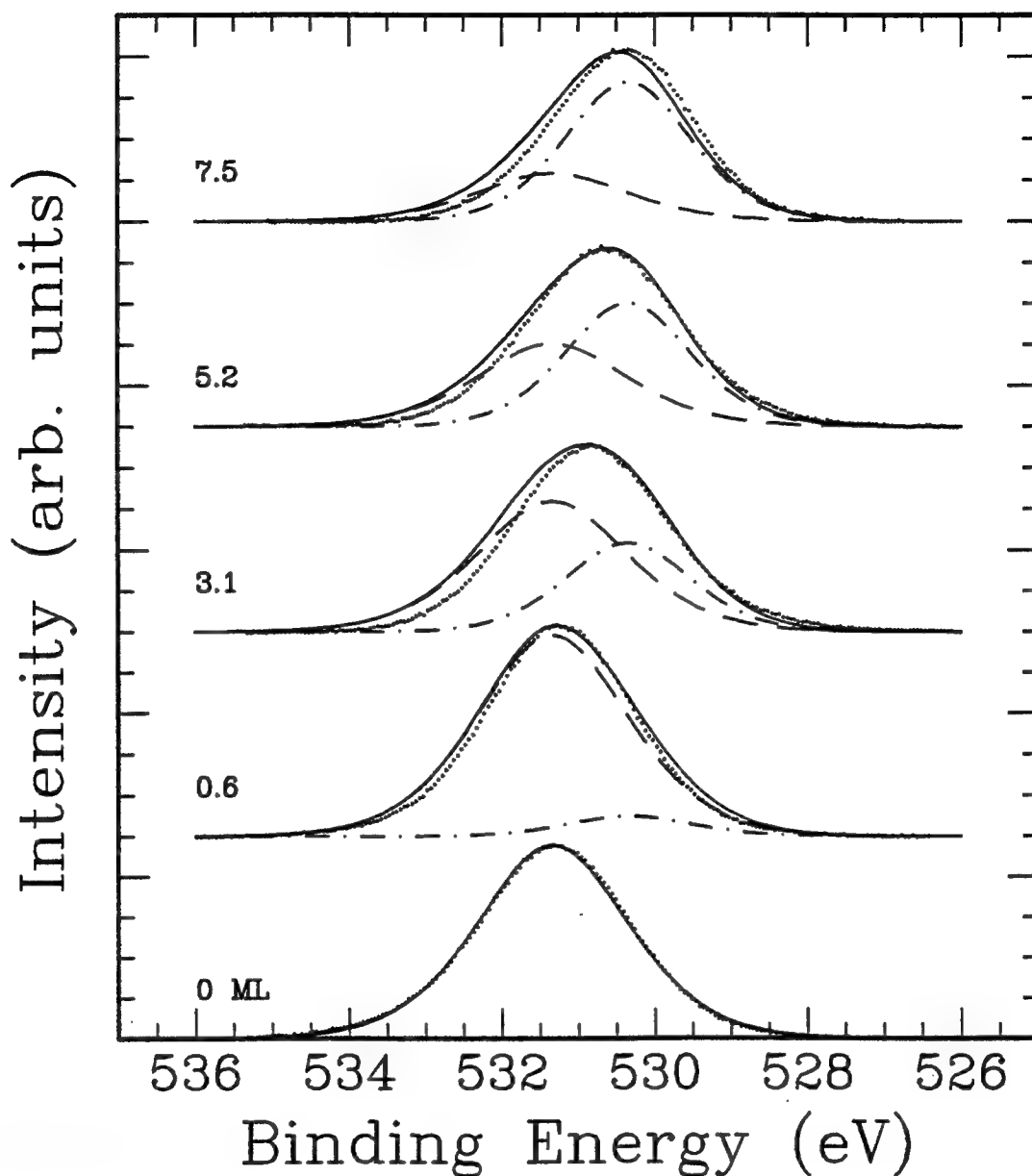
Figure 7.7. Experimental and simulated XPS O 1s peaks for a -0.99 eV total shift. The film was produced by 60°C dose and 460°C anneal cycles. The dots represent experimental peaks after background subtraction. The dash-dash, dot-dash, and solid lines represent the oxygen from O - Al bonding, O - Ti bonding, and the composite peak, respectively.

Figure 7.8. Experimental and simulated XPS O 1*s* peaks for a -1.07 eV total shift. The film was produced by 60°C dose and 460°C anneal cycles. The dots represent experimental peaks after background subtraction. The dash-dash, dot-dash, and solid lines represent the oxygen from O - Al bonding, O - Ti bonding, and the composite peak, respectively.

Figure 7.9. Experimental and simulated XPS O 1s peaks for a -1.15 eV total shift. The film was produced by 60°C dose and 460°C anneal cycles. The dots represent experimental peaks after background subtraction. The dash-dash, dot-dash, and solid lines represent the oxygen from O - Al bonding, O - Ti bonding, and the composite peak, respectively.

bonding, and the composite peak, respectively. The peak for O - Al bonding was fixed at 531.34 eV. This is the position of the experimental peak at 0 ML relative to Al $2p$ at 74.4 eV.[7.11] Where necessary, the simulated peaks for a particular thickness were scaled by the same factor to match the amplitudes of the experimental and simulated composite peak. The scaling factors ranged from 1.0 to 1.4.

The three total shifts produced composite peaks decreasing in binding energy with increasing film thickness. The shapes of the experimental and simulated peaks agree within the range of total shifts shown. Peak shapes from one total shift does not produce the best agreement with all the experimental peaks. This suggests the total shift for the thin film produced by 60°C doses and 460°C anneals ranges from -0.99 to -1.15 eV.

Experimental peaks for the film grown by 200°C dose and 700°C anneal cycles and simulated peaks for total O $1s$ shifts of -1.07, -1.15, and -1.23 eV are shown in Figures 7.10, 7.11, and 7.12, respectively. The peaks are shown for thicknesses of 0, 0.8, 3.8, 5.7, and 8.3 ML. The peak for oxygen from Al_2O_3 was fixed at 531.42 eV. This is the position of the O $1s$ peak for 0 ML relative to Al $2p$ at 74.4 eV.[7.11]

Composite peak positions decreased with increasing film thickness for the three total shifts. The experimental peak shapes agree with simulated peaks for the range of total shifts shown. The peaks from one total shift did not appear to give the best agreement with all the experimental peaks. This suggests the total shift for the film produced by 200°C doses and 700°C anneals ranges from -1.07 to -1.23 eV.

Figure 7.10. Experimental and simulated XPS O 1s peaks for a
-1.07 eV total shift. The film was produced by 200°C dose and 700°C
anneal cycles. The dots represent experimental peaks after background
subtraction. The dash-dash, dot-dash, and solid lines represent the
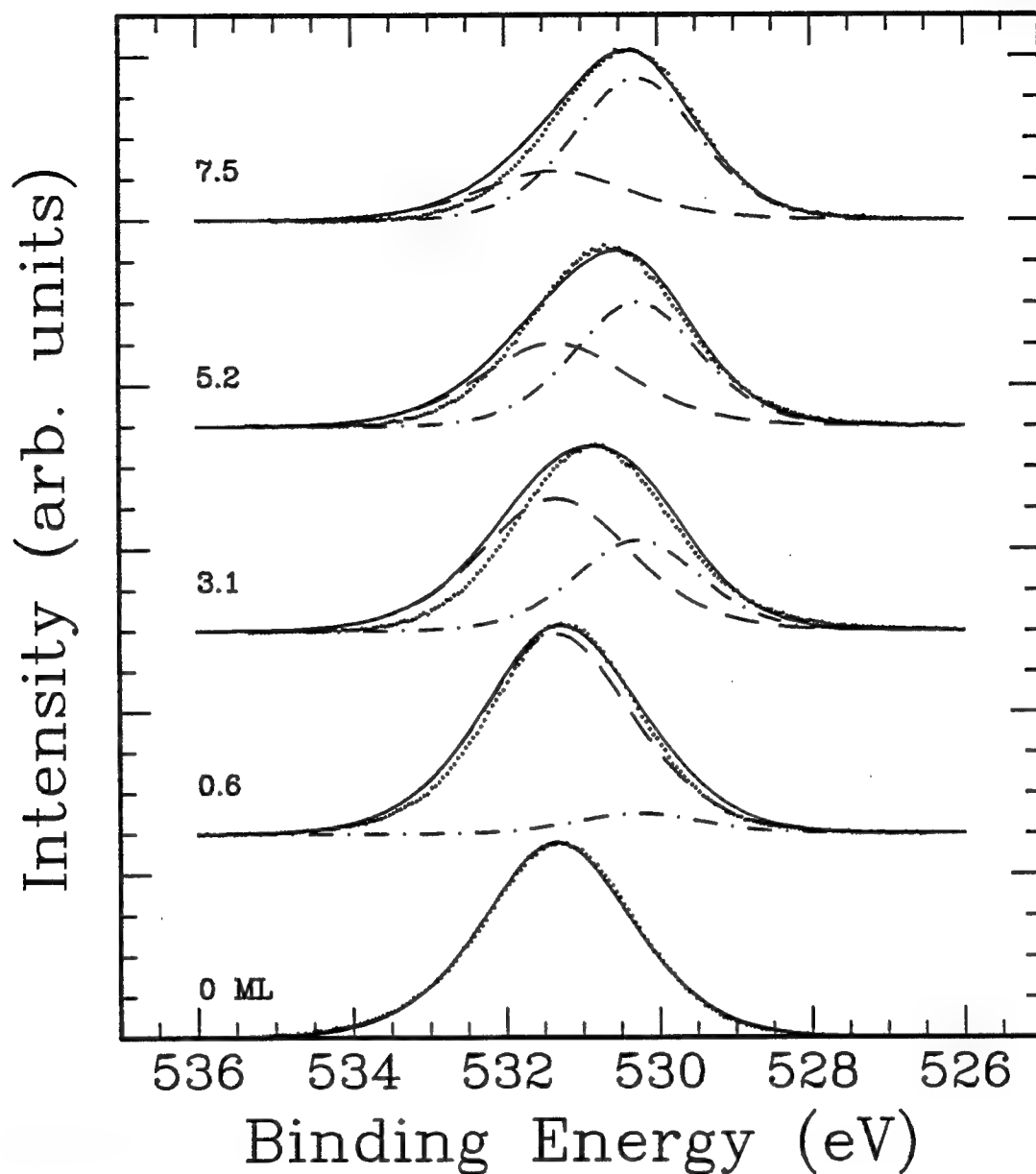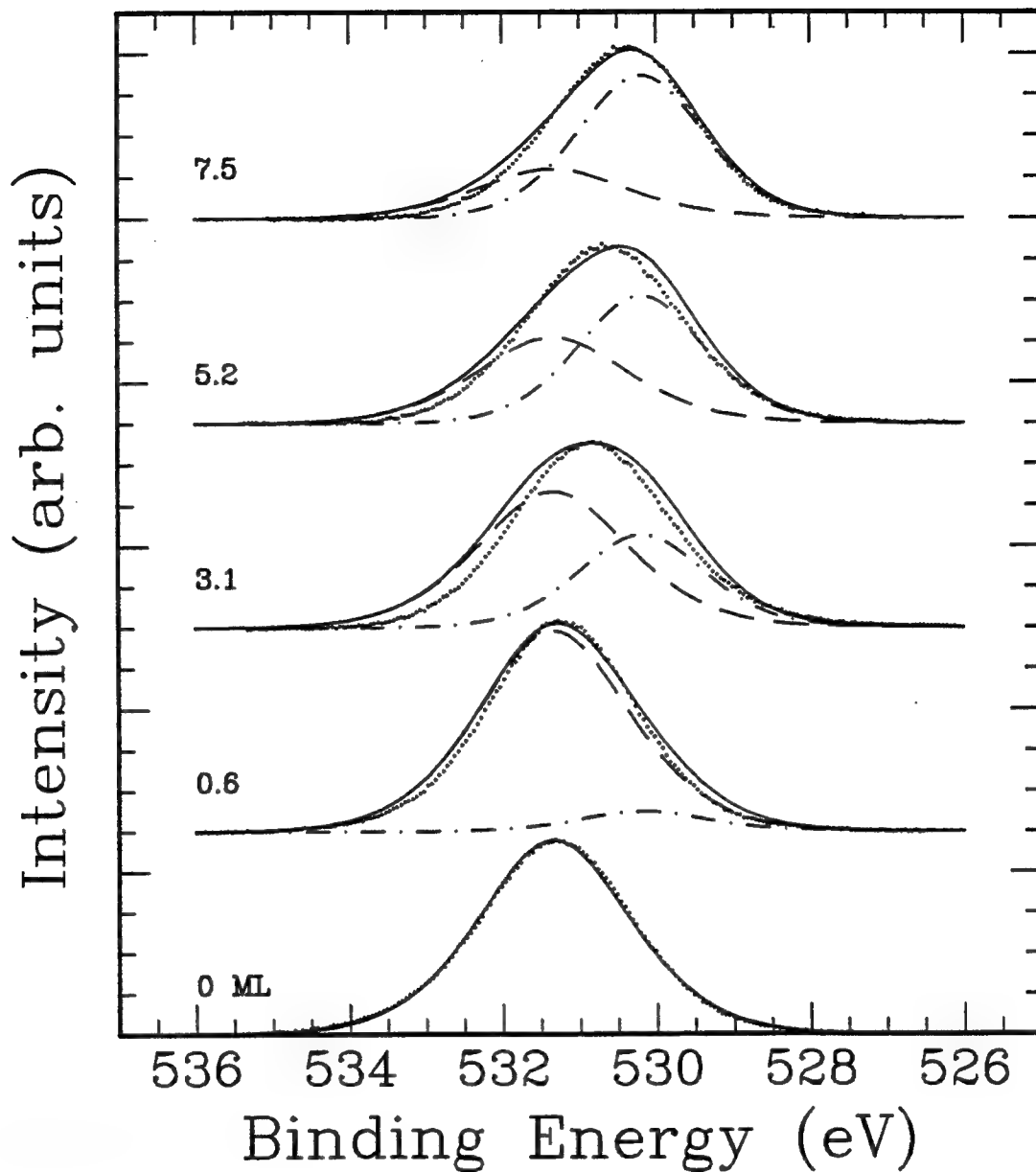oxygen from O - Al bonding, O - Ti bonding, and the composite peak,
respectively.
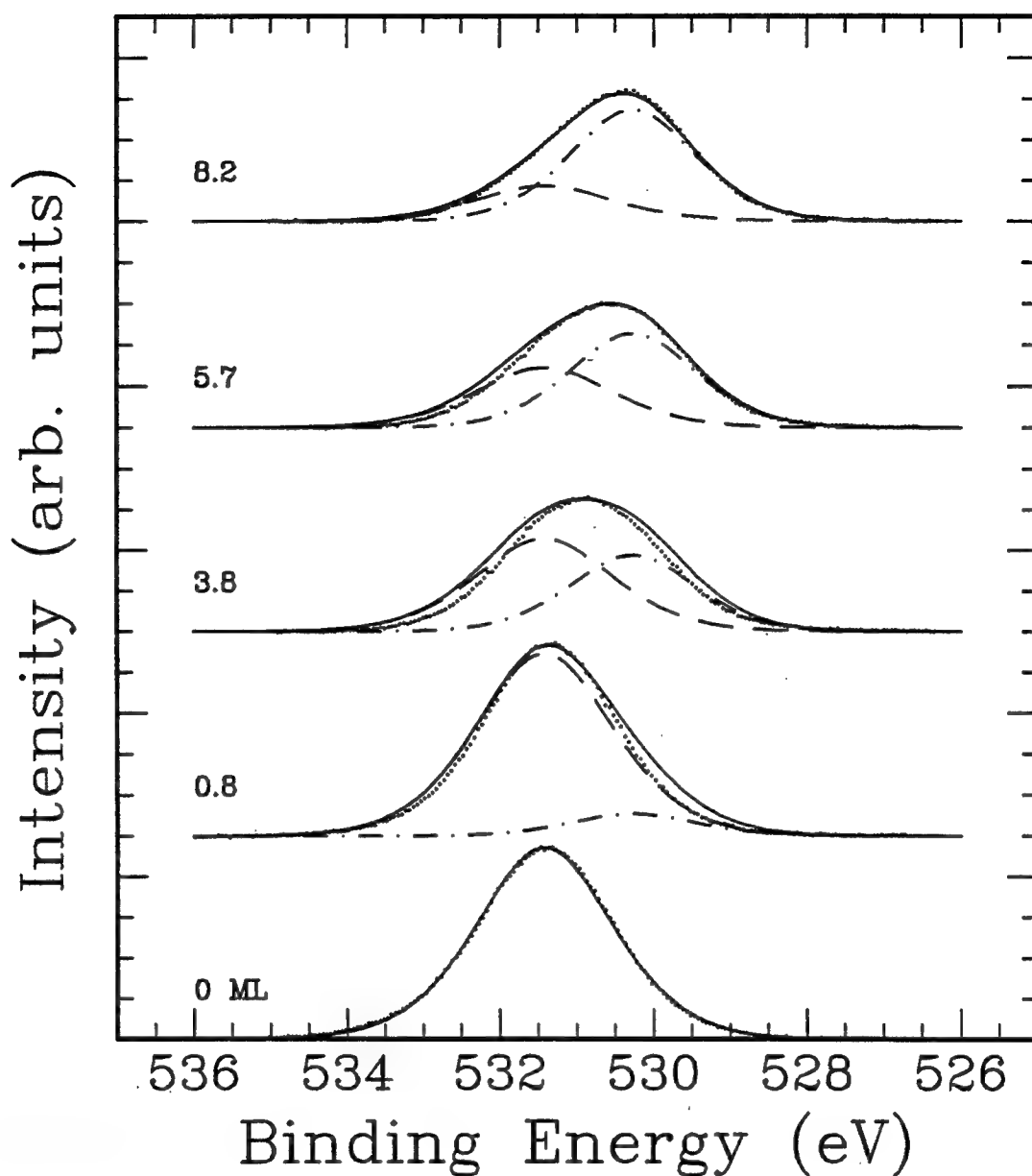
Figure 7.11. Experimental and simulated XPS O 1s peaks for a
-1.15 eV total shift. The film was produced by 200°C dose and 700°C
anneal cycles. The dots represent experimental peaks after background
subtraction. The dash-dash, dot-dash, and solid lines represent the
oxygen from O - Al bonding, O - Ti bonding, and the composite peak,
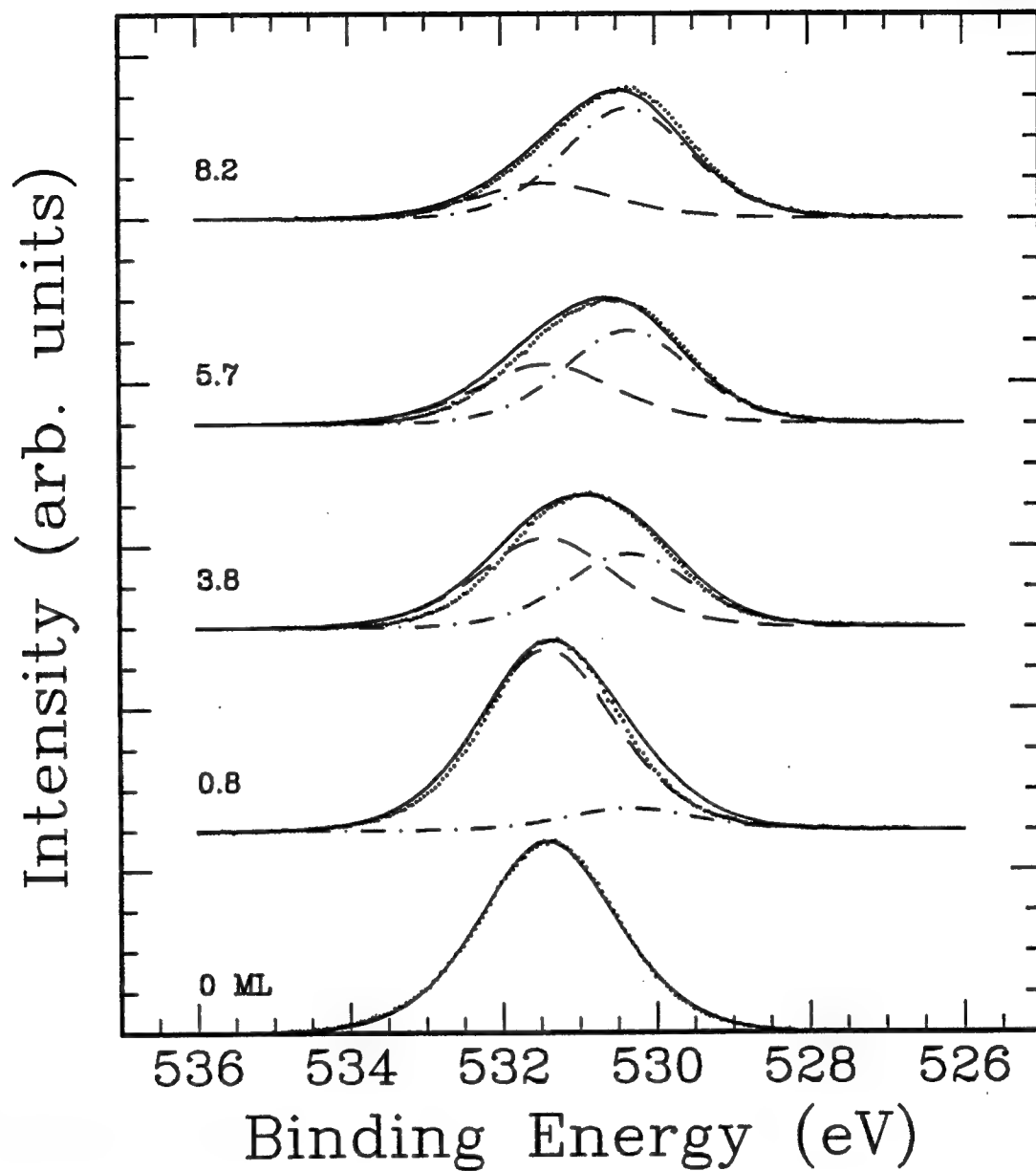respectively.
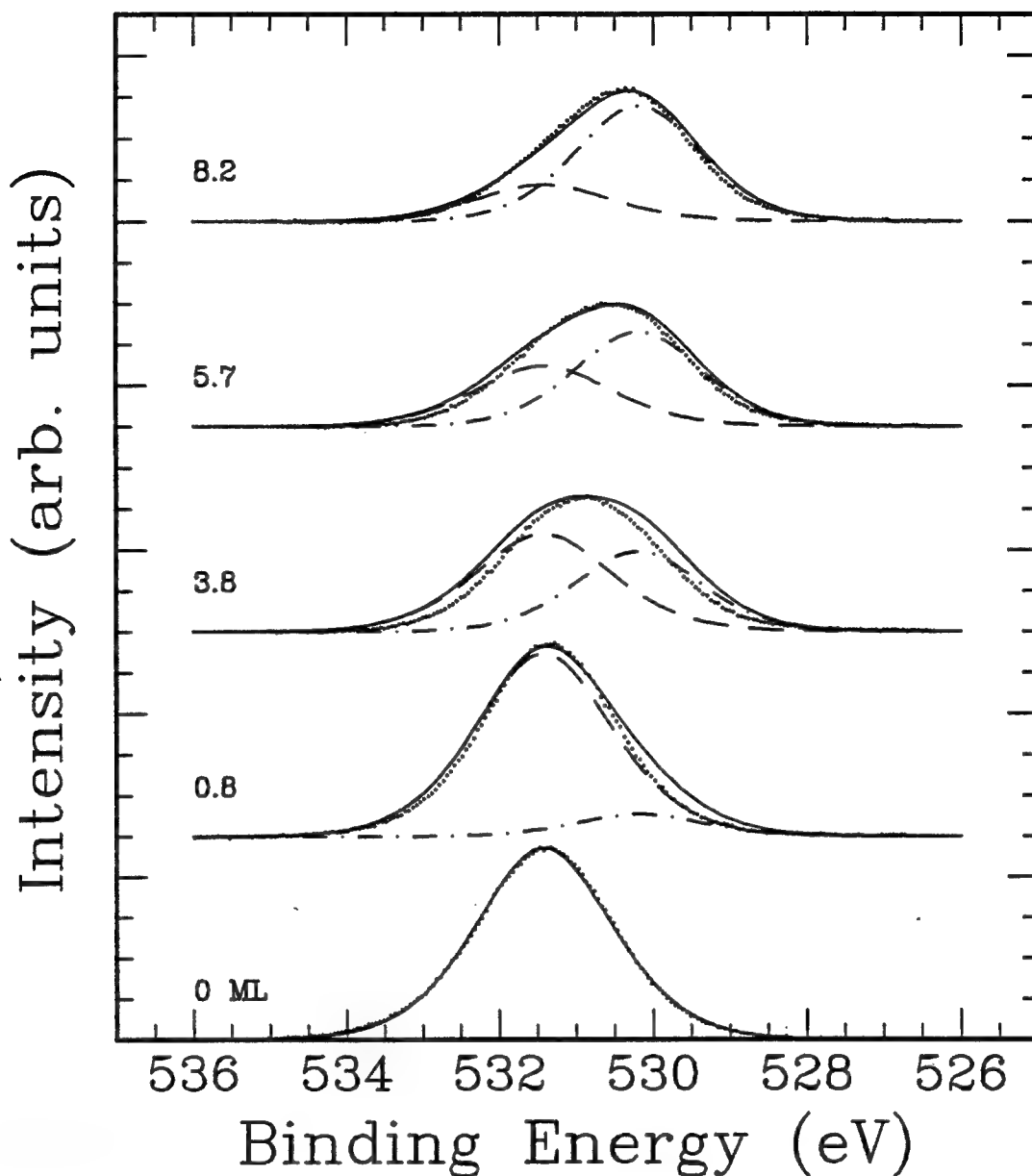
Figure 7.12. Experimental and simulated XPS O 1s peaks for a -1.23 eV total shift. The film was produced by 200°C dose and 700°C anneal cycles. The dots represent experimental peaks after background subtraction. The dash-dash, dot-dash, and solid lines represent the oxygen from O - Al bonding, O - Ti bonding, and the composite peak, respectively.

Several simulated composite peaks are wider than the corresponding experimental peaks. Two assumptions were made in creating the simulations. The simulations were created from FWHMS and Gaussian-Lorentzian mixing factors measured from oxygen peaks for clean sapphire and bulk TiO_2. These values were assumed to be independent of thickness. This appears reasonable because the Al $2p$ peaks did not show trends in changing FWHM or mixing factor with film thickness.

The FWHM of a peak, ΔE, is determined by the following:[7.16]

$$\Delta E = \left(\Delta E_n^2 + \Delta E_p^2 + \Delta E_a^2\right)^{1/2} \qquad (7.4)$$

where ΔE_n, ΔE_p, and ΔE_a are widths of the core level, X-ray source and analyser, respectively. The peaks are assumed to be Gaussian shapes. In the simulations, the widths from the x-ray source and analyser were not separated from the core level. Creating two separate peaks and then adding them accounts for the X-ray source and analyser widths twice. The composite peak width will larger than a peak in which the X-ray source and analyser widths are accounted for once.

The total O $1s$ shifts of -0.99 to -1.23 eV determined from simulations for thin films produced by 60°C dose and 460°C anneal cycles, and 200°C dose and 700°C anneal cycles, agree within the uncertainties with total shifts determined from thick films.

7.4   Conclusions

Reduction of sapphire due to CVD deposition of titanium dioxide from titanium isopropoxide precursor was not detected within the limits of XPS. This suggests the titanium in the precursor molecule has sufficient oxygen to form stoichiometric TiO_2 without breaking oxygen to aluminum bonds in the sapphire. Evidence for charge transfer at the interface from the titanium to the oxygen in the sapphire was also not observed within the limits of XPS.

The XPS O $1s$ peak was observed to shift with increasing film thickness for films produced by the cycle method and continuous depositions above the pyrolysis temperature. Simulations of shifts with film thickness for thin films were produced. They indicated changes in energy positions are consistent with oxygen in O to Al bonds from sapphire and in O to Ti bonds from TiO_2 having different binding energy positions. The shifts are due to changes in bonding environment.

7.5   References for Chapter 7

7.1   S. Hofmann, "Depth Profiling"; pp. 141-79 in *Practical Surface Analysis by Auger and X-ray Photoelectron Spectroscopy*. Edited by D. Briggs and M.P. Seah. John Wiley & Sons, Chichester, 1983.

7.2   L.C. Feldman and J.W. Mayer, *Fundamentals of Surface and Thin Film Analysis*; Ch. 3-4, pp. 39-98. Elsevier Science Publishing Co., Inc., New York, New York, 1986.

7.3   J.C. Rivière, *Surface Analytical Techniques*; Ch. 3, pp. 27-80. Oxford University Press, New York, 1990.

7.4   Y.S. Chaug, N.J. Chou, and Y.H. Kim, "Interaction of Ti With Fused Silica and Sapphire During Metallization," *J. Vac. Sci. Technol. A*, **5** [4] 1288-91 (1987).

7.5   J.H. Selverian, F.S. Ohuchi, M. Bortz and M.R. Notis, "Interface Reactions Between Titanium Thin Films and (1-12) Sapphire Substrates," *J. Mater. Sci.*, **26**, 6300-308 (1991).

7.6   J.H. Selverian, F.S. Ohuchi, and M.R. Notis, "Microstructure and Kinetics of the Interface Reaction Between Titanium Thin Films and (1-12) Sapphire Substrates," *Mater. Res. Soc. Symp. Proc.*, **167**, 335-40 (1990).

7.7   J.H. Selverian, M. Bortz, F.S. Ohuchi and, M.R. Notis, "The Microstructure and Chemistry of the Reaction Between Ti and α-Al_2O_3," *Mater. Res. Soc. Symp. Proc.*, **108**, 107-10 (1988).

7.8   F.S. Ohuchi and M. Kohyama, "Electronic Structure and Chemical Reactions at Metal-Alumina and Metal-Aluminum Nitride Interfaces," *J. Am. Ceram. Soc.*, **74** [6] 1163-87 (1991).

7.9   H. Lefakis, M. Liehr, G.W. Rubloff, P.S. Ho, "Alumina-Ti Interface Reactions Studied by AES and UPS," *Mater. Res. Soc. Symp. Proc.*, **54**, 133-38 (1986).

7.10   C.P. Lofton and W.E. Swartz, Jr., "Auger and X-ray Photoelectron Spectroscopies Depth Profiling Techniques Applied to Ultra-Thin Titanium Films," *Thin Solid Films*, **52**, 271-80 (1978).

7.11   J.F. Moulder, W.F. Stickle, P.E. Sobol, and K.D. Bomben, *Handbook of X-ray Photoelectron Spectroscopy*. Edited by J. Chastain. Perkin Elmer Corporation, Eden Prairie, Minnesota,

1992.

7.12   C.N. Sayers and N.R. Armstrong, "X-ray Photoelectron Spectroscopy of TiO_2 and Other Titanium Oxide Materials: Surface Compositional Changes of the TiO_2 Electrode During Photoelectrolysis," *Surf. Sci.*, **77**, 301-20 (1978).

7.13   J.P. Lu and R. Raj, "Ultra-high Vacuum Chemical Vapor Deposition and *In situ* Characterization of Titanium Oxide Thin Films," *J. Mater. Res.*, **6** [9] 1913-18 (1991).

7.14   J.C. Rivière, *Surface Analytical Techniques*; Ch. 10, pp. 238-313. Oxford University Press, New York, 1990.

7.15   A.D. Baker and D. Betteridge, *Photoelectron Spectroscopy: Chemical and Analytical Aspects*; Ch. 4, pp. 55-101. Pergamon Press Ltd., Oxford, 1972

7.16   D. Briggs and J.C. Rivière , "Chapter 3. Spectral Interpretation"; pp. 87-139 in *Practical Surface Analysis by Auger and X-ray Photoelectron Spectroscopy*. Edited by D. Briggs and M.P. Seah. John Wiley & Sons, Chichester, 1983.

7.17   G. Ertl and J. Küppers, *Low Energy Electrons and Surface Chemistry*; Ch. 3, pp. 66-85. VCH Publishers, Deerfield Beach, Fl, 1985.

7.18   W.J. Moore, *Physical Chemistry*, Vol 4; Ch. 15, pp. 697-699. Prentice-Hall, Inc., Englewood Cliffs, New Jersey, 1972.

7.19   T.E. Madey, C.E. Wagner and A. Joshi, "Surface Characterization of Catalysis Using Electron Spectroscopies: Results of a Round-Robin Sponsored by ASTM Committee D-32 on Catalysts," *J. Electron Spectrosc. Relat. Phenom.*, **10**, 359-88 (1977).

7.20   I. Olefjord, H.J. Mathieu, and P. Marcus, "Intercomparison of Surface Analysis of Thin Aluminum Oxide Films," *Surf. Interface Anal.*, **15**, 681-92 (1990).

7.21   D.L. Cocke, T.R. Hess, T. Mebrahtu, D.E. Mencer, Jr., and D.G. Naugle, "The Surface Reactivity of Ti-Cu and Ti-Al Alloys and the Ion Chemistry of Their Oxide Overlayers," *Solid State Ionics*, **43**, 119-31 (1990).

7.22   D. Gonbeam, C. Guimon, G. Pfister-Guillouzo, A. Levasseur, G. Meunier, and R. Dornoy, "XPS Study of Thin Films of Titanium Oxysulfides," *Surf. Sci.*, **254**, 81-89 (1991).

7.23   S. Chen, M.G. Mason, H.J. Gysling, G.R. Paz Pujalt, T.N.
        Blanton, T. Castro, K.M. Chen, C.P. Fictorie, W.L. Gladfelter,
        A. Franciosi, P.I. Cohen and J.F. Evans, "Ultrahigh Vacuum
        Metalorganic Chemical Vapor Deposition Growth and *In Situ*
        Characterization of Epitaxial TiO_2 Films," *J. Vac. Sci. Technol.,
        A*, **11** [5] 2419-29 (1993).

Chapter 8
Conclusions

8.1   Introduction

Thin films of titanium dioxide produced on sapphire(0001) by MOCVD from titanium isopropoxide precursor were investigated in this work. The films were deposited and characterized by *in situ* XPS analysis in an UHV chamber. Film thicknesses ranged from 0.1 to 2.7 nm. Although the primary focus of this work was thin films, thick ones were also produced and evaluated as a comparison. A summary of the experimental observations from Chapters 5, 6, and 7 is presented in this chapter. Suggestions for future work are also included.

8.2   UHV-MOCVD of titanium dioxide from titanium isopropoxide precursor

An understanding of the CVD process steps and parameters provides the basic groundwork for optimization and control of titanium dioxide deposition from titanium isopropoxide precursor. The issues of interest include precursor decomposition temperature, dosing above and below the pyrolysis temperature, affects of post-deposition annealing, and film stoichiometry.

The precursor decomposition temperature was determined by two methods. In one case, sapphire heated to temperatures ranging

from room temperature to 700°C was dosed with precursor vapor and the resulting depositions evaluated. In the second case, precursor was first adsorbed on sapphire at low temperature. The XPS C 1s and Ti 2$p_{3/2}$ photoelectrons peaks were then monitored as a function of isothermal anneals to 700°C. Both cases indicated decomposition occurred above 300°C. Decomposition of precursor molecules on the sapphire was not accompanied by desorption. Dosing below the pyrolysis temperature showed initial uptake of precursor, followed by saturation at approximately 15 minutes. Titanium isopropoxide was confirmed by XPS analysis of thick films to produce stoichiometric TiO_2.

The CVD process steps include adsorption and decomposition of precursor. The observations of Chapter 5 indicated these steps could be performed in a distinct separate manner by first adsorbing the precursor below the pyrolysis temperature, then annealing above the pyrolysis temperature to form titanium oxide.

8.3   Controlled submonolayer depositions of titanium dioxide

The observations from Chapter 5 were applied to produce controlled submonolayer depositions of titanium dioxide. The procedure developed consisted of cycles of absorbing precursor below 300°C for 15 minutes, followed by annealing above 300°C. Film thickness was built up by repeated cycles. Two dose and anneal temperatures were investigated.

Cycles of 60°C doses and 460°C anneals produced a growth rate of 0.11 ML of titanium dioxide per cycle. This growth rate was compared to a theoretical rate of 0.169 ML/cycle and 0.158 ML/cycle for anatase and rutile, respectively. The theoretical calculation assumed adsorption of titanium isopropoxide was limited to one monolayer and each molecule decomposed to form one molecule of titanium dioxide. Since the precursor molecules are assumed to have ideal packing, the theoretical value is an upper limit to the growth rate. The experimental and theoretical growth rates were in agreement.

Films were produced by 200°C dose and 700°C anneal cycles in which the annealing duration was 30 minutes. A growth rate consistent with the theoretical calculation was observed up to 15 cycles or approximately 2.5 monolayers. Above that thickness the growth rate decreased. Additional investigation showed the apparent growth rate was affected by the annealing duration above, but not below that thickness. Decreasing the annealing time increased the growth rate. The affects of isothermal annealing at 700°C was evaluated. Film thickness was observed to decreased with annealing time until 3 monolayers was reached.

The affect of annealing can be explained by film desorption. The stable film thickness is 2.5 to 3 monolayers. Above this thickness, desorption occurs with annealing. For a film thickness above 2.5 to 3 monolayers, decomposition of precursor was accompanied by titanium oxide desorption during the annealing segment of the cycling procedure. The stability of films at 2.5 to 3 monolayers suggests bonding of the

initial few monolayers to the sapphire is stronger.

The low temperature dose and high temperature anneal cycling procedure produced films with the TiO_2 stoichiometry as determined by XPS. Film thickness ranged from 0.1 to 2.7 nm.

The AFM topographic images of the films produced by the cycling method indicated the presence of grain structure. The grain size increased with increased cycle annealing temperature. It is possible the grains are due to the formation of the rutile phase with three orientation variants. A TEM cross-sectional image to determined if the grains are due to orientation variants is suggested for future work.

8.4   Titanium dioxide to sapphire interface

Evidence for reduction of sapphire by titanium dioxide and charge transfer at the interface was investigated by studying the XPS peak shapes and positions. Reactions were not observed within the detection limit of XPS. Reduction of sapphire substrate by titanium metal has been reported in the literature. Depositions from titanium isopropoxide was not observed to reduce the sapphire in order to form bonds with oxygen in the substrate. The precursor appears to contain sufficient oxygen to form the stoichiometric titanium dioxide film.

The XPS O $1s$ peak showed shifts to lower binding energies with increasing film thickness. A simulation for the shifts were made by assuming oxygen from sapphire and titanium dioxide occupy different energy positions. Simulated peak shapes and positions were compared

with experimental peaks. The simulations indicated the total shift was -0.99 to -1.23 eV. For thick films, the total shift was determined to be -1.07 $\pm$ 0.08 eV and -1.19 $\pm$ 0.08 eV. The total shifts from the thin and thick films are in agreement.

A TEM image providing a cross-sectional view of the thin films would show the atomic arrangement in the films and structural relationships between the films and sapphire. It would also permit determination of the TiO_2 structural phases. Such an analysis was not possible for the thin films by XRD.

Appendix 1
Dosing Tube Flux

A1.1   Introduction

Film growth in the UHV-MOCVD chamber is produced by
introducing precursor vapor through a dosing tube. The substrate is
placed at the exit of the tube. Films may also be produced by introducing
vapor into the chamber without a tube. The use of a dosing tube
eliminates or reduces the effects of residual gas impurities or impurities
from chamber walls or surfaces, and precursor decomposition due to
hot filaments within the chamber.[A1.1] The flux (molecules/m^2 sec)
emerging from the tube is expected to be higher than in the chamber.[A1.1]

In this appendix, the dosing tube flux is determined and
compared to the chamber flux for a pressure of 1.0 x 10^{-8} Torr. The
chamber was maintained at this pressure for all depositions produced
in this work. Additional details regarding the chamber setup and
deposition procedures were provided in Chapters 4 and 5. Section A1.3.2
discusses the thickness profile of a film produced by dosing through the
tube. The profile was obtained by RBS analysis.

The dosing tube flux was determined from the chamber
molecular pumping rate (molecules per second) and tube cross sectional
area. A molecular flow rate balance was applied to determine this
pumping rate. It accounted for removal of molecules, and introduction
of molecules by leakage and desorption off chamber surfaces.

A1.2 Experimental procedure

A1.2.1 Determination of chamber molecular pumping rate

The chamber molecular pumping rate was determined by first introducing titanium isopropoxide precursor vapor into the chamber until a pressure, P_0, ranging from 1.0 x 10-7 to 5.0 x 10-9 Torr was reached. The pressure was maintained at P_0 for hold times ranging from 0 to 15 minutes. The chamber was then permitted to pump down. The pressure decrease was monitored as a function of time until typically better than 1.0 x 10-9 Torr was reached. Timing began when the leak valve to the precursor was closed. The chamber pressure before vapor introduction was better than 5.0 x 10-10 Torr.

Ten combinations of P_0 and hold times were used to evaluate their effect on pump speed and desorption. Five repeat runs were made for a P_0 of 1.0 x 10-7 Torr and zero hold time. Two repeat runs were made for a P_0 of 1.0 x 10-7 Torr and 10 minutes hold times. Two repeat runs were also made for a P_0 of 1.0 x 10-8 Torr and zero hold time. Data from these P_0 and hold times are shown as averages.

A1.2.2 RBS analysis

RBS analysis was performed on a thick film of titanium dioxide to determine its thickness profile. The film was produced by continuous

dosing with titanium isopropoxide precursor at a substrate temperature of 300°C. Additional details regarding the growth of this film was given in Chapter 5. The film stoichiometry was determined to be TiO_2 in Section 5.3.4

RBS spectra was collected using He^{2+} ions with 2.2 MeV energy at an angle of 7° to the surface normal. Film thicknesses were determined from simulations using the RUMP program. The program uses a film density to create the simulation. The film was assumed to have the density of an anatase phase. Comments regarding the assumption of an anatase or rutile density were given in Section 5.2.6.

A1.3   Results and discussion

A1.3.1 Dosing tube and chamber flux

The dosing tube flux, Γ_d (molecules/m^2 sec), at a particular pressure can be determined from the molecular flow rate, dN_d/dt (molecules/sec), entering the chamber and the tube cross sectional area. The net molecular flow rate, dN/dt (molecules/sec) in a chamber is a sum of terms representing gas entering and leaving the chamber. The dN/dt can be given as:

$$\frac{dN}{dt} = -\frac{dN_r}{dt} + \frac{dN_i}{dt} \qquad (A1.1)$$

where dN_r/dt and dN_i/dt are the molecular flow rates for removal and

introduction of molecules, respectively. Removal could be due to pumping or adsorption on the walls. Sources of gas include deliberate introduction through a leak valve, leakage into the chamber, and outgassing from the walls and surfaces.

During film growth in this work, the chamber pressure was maintained at a pressure of 1×10^{-8} Torr. The dN/dt is related to changes in pressure by the following equations:

$$\frac{dP}{dt} = \frac{dP}{dN}\frac{dN}{dt} \qquad \text{(A1.2)}$$

For an ideal gas:

$$\frac{dP}{dN} = \frac{kT}{V} = A_v \qquad \text{(A1.3)}$$

where k, T, and V are the Boltzmann constant, temperature, and chamber volume, respectively. A_v is a constant for constant T. The chamber volume was estimated to be 49.43 L. From equations A1.2 and A1.3:

$$\frac{dP}{dt} = A_v \frac{dN}{dt} \qquad \text{(A1.4)}$$

For a constant pressure, dN/dt will be zero. During film deposition, removal of gas molecules is assumed to be due only to pumping by the chamber ionization pump. Adsorption by walls is assumed to occur quickly and to reach a saturation limit during the initial introduction of

precursor vapor. The chamber base pressure is typically better than 1.0 x 10^{-10} Torr. Any leakage into the chamber is considered relatively small compared to the dosing pressure. Outgassing is not expected to occur because the chamber pressure was raised during film deposition. During film deposition, the balance of molecular flow rates in and out of the chamber is given by:

$$\frac{dN_d}{dt} = \frac{dN_p}{dt} \tag{A1.5}$$

where dN_p/dt is the chamber molecular pumping rate due to the ionization pump. The dosing tube flux can be determined if dN_p/dt is known.

The dN_p/dt as a function of pressure was determined by initially filling the chamber with titanium isopropoxide precursor, then monitoring decreases in pressure with time. In this case, during the pump down, dN_d/dt and adsorption by the walls is zero. Leakage, dN_l/dt, and desorption, dN_o/dt, from the walls must be considered in equation A1.1. The resulting molecular flow rate balance is:

$$\frac{dN}{dt} = -\frac{dN_p}{dt} + \frac{dN_l}{dt} + \frac{dN_o}{dt} \tag{A1.6}$$

The dN_p/dt is proportional to flux, Γ, which is related to pressure by the following equation:[A1.2]

$$\Gamma = \left(\frac{P}{kT}\right)\left(\frac{kT}{2\pi M}\right)^{1/2} \qquad (A1.7)$$

where k and M are the Boltzmann constant and molecular mass, respectively. For a given temperature, the relation between dN_p/dt and pressure can be expressed as:

$$\frac{dN_p}{dt} = \beta P \qquad (A1.8)$$

where β is a proportionality constant. For the case where dN_i/dt is zero, the chamber pressure change is given by the following equation:

$$\frac{dP}{dt} = A_v \frac{dN}{dt} = -A_v \frac{dN_p}{dt} = -A_v \beta P \qquad (A1.9)$$

A similar equation which often appears in the literature is:[A1.3]

$$\frac{dP}{dt} = \frac{-S_{pump} P}{V} \qquad (A1.10)$$

where S_{pump} is defined as the pumping speed or volumetric flow rate across a plane.[A1.2, A1.3] It has units of volume per unit time. S_{pump} is related to β as follows:

$$S_{pump} = kT\beta \qquad (A1.11)$$

For a constant leakage rate, dN_l/dt, can be expressed as:

$$\frac{dN_1}{dt} = q \tag{A1.12}$$

where q is a constant with units of molecules per second. As an approximation, desorption from chamber surfaces is assumed to be a first order reaction. It is expressed as:[A1.3]

$$\frac{dN_o}{dt} = K \ N^a \ exp \ (-K \ t) \tag{A1.13}$$

where K and N^a are the time constant and initial concentration of molecules on the chamber surfaces, respectively.

Combining equations A1.6, A1.8, A1.12, and A1.13 gives:

$$\frac{dN}{dt} = -\frac{dN_p}{dt} + \frac{dN_1}{dt} + \frac{dN_o}{dt} = -\beta P + q + K N^a exp(-Kt) \tag{A1.14}$$

During the initial pump down from P_o, dN_p/dt will be the predominant term. As the pressure decreases, dN_1/dt and dN_o/dt will become more predominant. Equation A1.14 can be expressed in terms of pressures changes.

$$\frac{dP}{dt} = -A_v \beta P + A_v q + A_v K N^a exp \ (-Kt) \tag{A1.15}$$

Nomalizing by dividing by P_o and defining P^* as P/P_o gives:

$$\frac{dP^*}{dt} = -A_v \beta P^* + \frac{A_v}{P_o} q + \frac{A_v}{P_o} K N^a \exp(-Kt) \qquad \text{(A1.16)}$$

In the limiting case where t approaches infinity, dP^*/dt and $\exp(-\infty)$ will approach zero. The q is given by the following terms:

$$q = \beta P_\infty \qquad \text{(A1.17)}$$

where P_∞ is the pressure as t approaches infinity. Equation A1.16 can be rewritten as:

$$\frac{dP^*}{dt} = -a_1 P^* + a_1 P_\infty^* + \frac{a_2}{P_o} \exp(-a_3 t) \qquad \text{(A1.18)}$$

where
$$a_1 = A_v \beta \qquad \text{(A1.19)}$$

$$a_2 = A_v K N^a \qquad \text{(A1.20)}$$

$$a_3 = K \qquad \text{(A1.21)}$$

The differential of equation A1.18 is a second order non-homogeneous linear equation. The solution for equation A1.18 is:

$$P^*(t) = P_\infty^* + C_1 \exp(-a_1 t) + C_2 \exp(-a_3 t) \qquad \text{(A1.22)}$$

where
$$C_1 = 1 - C_2 - P_\infty^* \qquad \text{(A1.23)}$$

$$C_2 = \frac{a_2}{P_o \left(a_1 - a_3\right)} \qquad \text{(A1.24)}$$

Figure A1.1 shows the normalized pressure as a function of pumping time for a P_0 of 1 x 10^{-7} Torr and zero hold time. The line shown is a non-linear least squares fit of equation A1.22 to the data using the GENPLOT program. Values for a_1, a_2, and a_3 were obtained from this fit. There is good agreement between the experimental data and the fit. Figure A1.1 is a typical example of the pressure with pumping time experimental data and its corresponding fit. Table A.1 summarizes the results of fitting equation A1.22 to experimental data with varying P_0 and hold times. The table gives values for a_1, a_2, and a_3.

For a P_0 of 1.0 x 10^{-7} Torr and zero hold time, a_1, a_2, and a_3 are averages of five runs with uncertainties of 5.8 x 10^{-3} s^{-1}, 7.6 x 10^{-11} Torr/sec, and 2.8 x 10^{-4} s^{-1}, respectively. For a P_0 of 1.0 x 10^{-7} Torr and 10 minutes hold time, the a_1, a_2, and a_3 are averages of two runs with uncertainties of 8.9 x 10^{-3} s^{-1}, 2.1 x 10^{-10} Torr/sec, and 7.6 x 10^{-5} s^{-1}, respectively. For a P_0 of 1.0 x 10^{-8} Torr and zero hold time, a_1, a_2, and a_3 are averages of two runs with uncertainties of 2.8 x 10^{-3} s^{-1}, 4.1 x 10^{-11} Torr/sec, and 4.2 x 10^{-4} s^{-1}, respectively.

The a_1 averaged 8.4 x 10^{-2} ± 1.3 x 10^{-2} s^{-1}. This term is not expected to vary with P_0 or hold time. The a_1 did not appear to change with hold time. It appeared to increase with decreasing P_0. The a_1 may not be constant over the two orders of magnitude in pressure evaluated. It also showed a relatively wide range of values. Use of the average a_1 will provide an estimate of the average dN_p/dt.
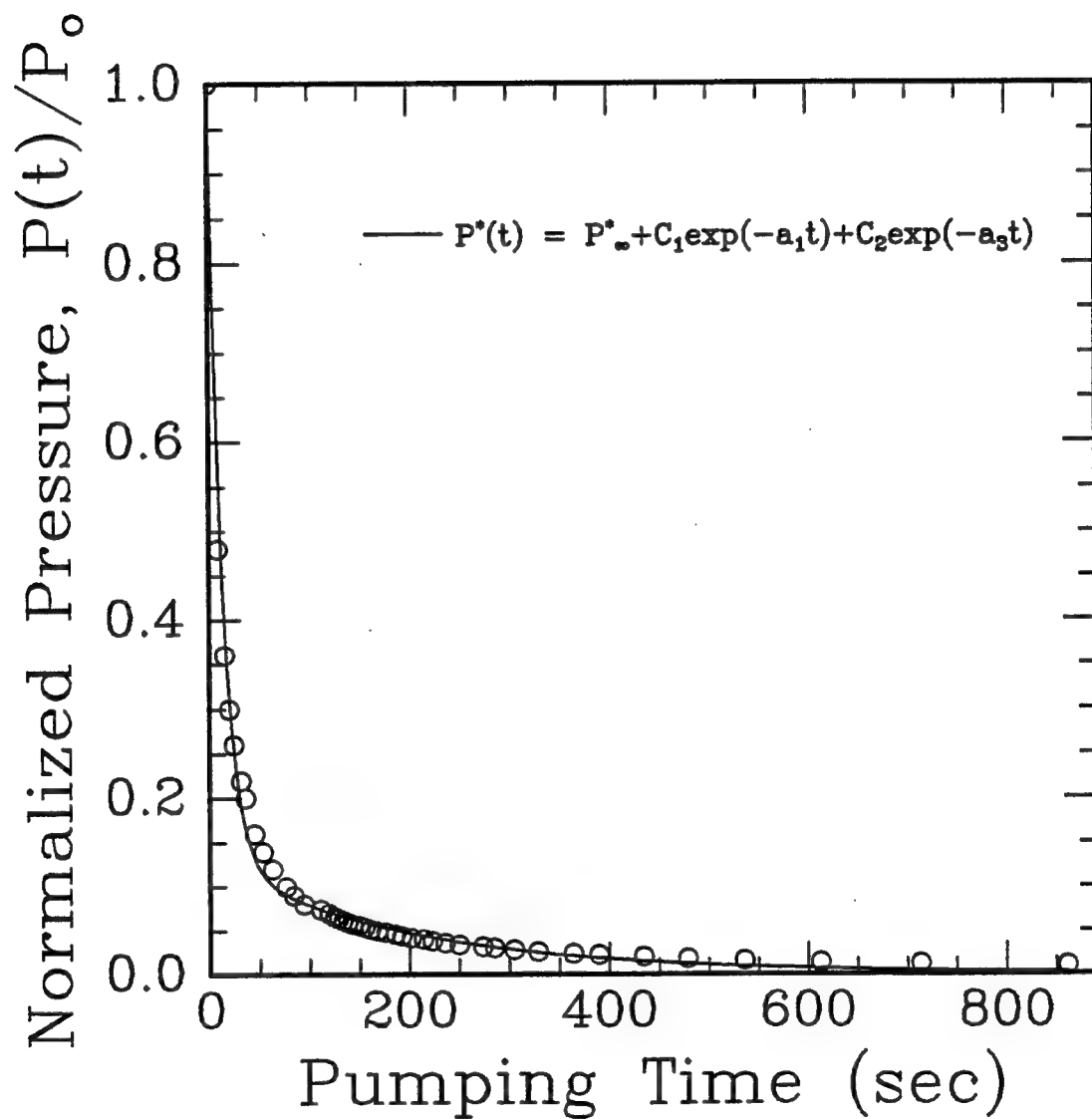
Figure A1.1. Normalized pressure, $P^*(t) = P(t)/P_o$, as a function of pumping time. The P_o and hold time were 1.0×10^{-7} Torr and zero, respectively.

Table A1.1 Values of a_1, a_2, and a_3 for Different P_o and Hold Times.

Experimental Conditions		Values From Fits to $P^*(t) = P^*_\infty + C_1 \exp(-a_1 t) + C_2 \exp(-a_3 t)$ $C_1 = 1 - C_2 - P^*_\infty, \quad C_2 = \dfrac{a_2}{P_o (a_1 - a_3)}$		
P_o (Torr)	Hold Time (min.)	a_1 (s^{-1}) x 10^{-2}	a_2 (Torr/sec) x 10^{-9}	a_3 (s^{-1}) x 10^{-3}
1.0×10^{-7}	0	7.7	1.0	4.2
1.0×10^{-7}	2	3.0	0.6	2.2
1.0×10^{-7}	5	6.2	1.1	2.4
1.0×10^{-7}	10	3.0	0.6	1.5
1.0×10^{-7}	15	5.2	0.9	1.7
7.5×10^{-8}	0	8.3	0.9	4.5
5.0×10^{-8}	0	10.6	0.8	5.1
2.5×10^{-8}	0	11.0	0.7	5.4
1.0×10^{-8}	0	15.4	0.5	9.3
5.0×10^{-9}	0	13.9	0.2	4.2

The a_2 and a_3 account for desorption off the chamber surfaces. The a_3 is a time constant and should not change with P_0 or hold time for a constant temperature. Values for a_3 did not show any clear trends with increasing P_0 or hold time. The a_3 for a P_0 of 1.0 x 10-8 Torr appeared high and may be an artifact.

An increase in adsorption concentration on the walls should occur with increased P_0 or hold time. The concentration increase should be reflected as a increase in a_2. Table A1.1 indicates the a_2 values increased with increased P_0. A consistent trend of increasing a_2 with hold time was not observed. If adsorption reaches a saturation limit relatively quickly for a P_0 of 1.0 x 10-7 Torr, increasing hold time will have insignificant effects on a_2.

The molecular flow rate through the dosing tube at a chamber pressure of 1 x 10-8 Torr was determined from equations A1.5, A1.8 and A1.19 to be 1.3 x 10^{12} molecules/sec. The dosing tube diameter, D_t, is 3/8 inches. The dosing tube flux was calculated from the following equation:

$$\Gamma_d = \frac{\dfrac{dN_d}{dt}}{\pi \left(\dfrac{D_t}{2}\right)^2} \tag{A1.25}$$

The dosing tube flux was estimated as 1.9 x 10^{16} molecules/m^2 sec. The chamber flux was determined to be 1.2 x 10^{16} molecules/m^2 sec from equation A1.7 for a pressure of 1.0 x 10-8 Torr. The dosing tube flux is 1.6 times higher than the chamber flux.

There were several assumptions made in determining the dosing tube and chamber flux. The pressure monitored during pump down was assumed to reflect the same gas species. Initially, the gas detected will be composed predominately of titanium isopropoxide. With continued pumping, the gas will be composed predominately of species such as oxygen or decomposed titanium isopropoxide products. The ionization gauge used to measured chamber pressure has different sensitivities to various gas molecules. The sensitivities were assumed to be the same.

In equation A1.22, the pressures are normalized. The only term affected by a sensitivity factor would be C_2 which accounts for desorption. The use of a sensitivity factor would affect determination of chamber flux from equation A1.7. A sensitivity factor for titanium isopropoxide was not given in the mass spectrometer manual[A1.4] or found in the literature. The sensitivity factors for organic molecules relative to nitrogen tend to be greater than 1. For methanol and acetone, the factors are 1.8 and 3.6, respectively.[A1.4] The sensitivity factor for titanium isopropoxide is also expected to be greater than 1.

The flux emerging from the dosing tube was assumed to be uniform across the tube cross sectional area. A circular pattern due to deposition is clearly visible in thick films deposited on sapphire. Film thickness uniformity is discussed in the following section.

A1.3.2 Film thickness profile

The thickness profile of a film deposited at 300°C was determined by RBS. The deposition appeared as a circle on the substrate with dimensions approximately close to the dosing tube diameter of 0.375 inches. The center has a blue color. At a diameter of about 0.32 inches, the color changed to red. At a diameter of about 0.35 inches, the color changed again to orange-yellow. The diameter of the orange-yellow was about 0.39 inches. The color beyond this diameter appeared grey due to the tantalum coated on the backside of the sapphire. The film colors may appear darker than they are due to the tantalum coating. However, the colors are clearly visible compared to clean sapphire.

RBS spectra were collected at six positions. Figure A1.2 shows a schematic of the film pattern and the RBS analysis positions. The RBS beam left a mark of about 1.5 mm x 1.5 mm at each position. Figure A1.3 shows the RBS spectra collected at position 1. The solid line is a RUMP simulation for a film with a thickness of 1500 Å. The spectra and simulation are typical of the six RBS spectra collected and their corresponding simulations.

Table A1.2 shows the film thickness at each position as determined from the RUMP simulations of the spectra. The highest thickness is at the center. Although the analysis area at each position is fairly large, the thicknesses from positions 1, 2, 3, and 4 agree within 150 Å. The thickness measured at position 5 is lower because it saddles the edge of the main grey circle. The decrease in thickness at the edge of the
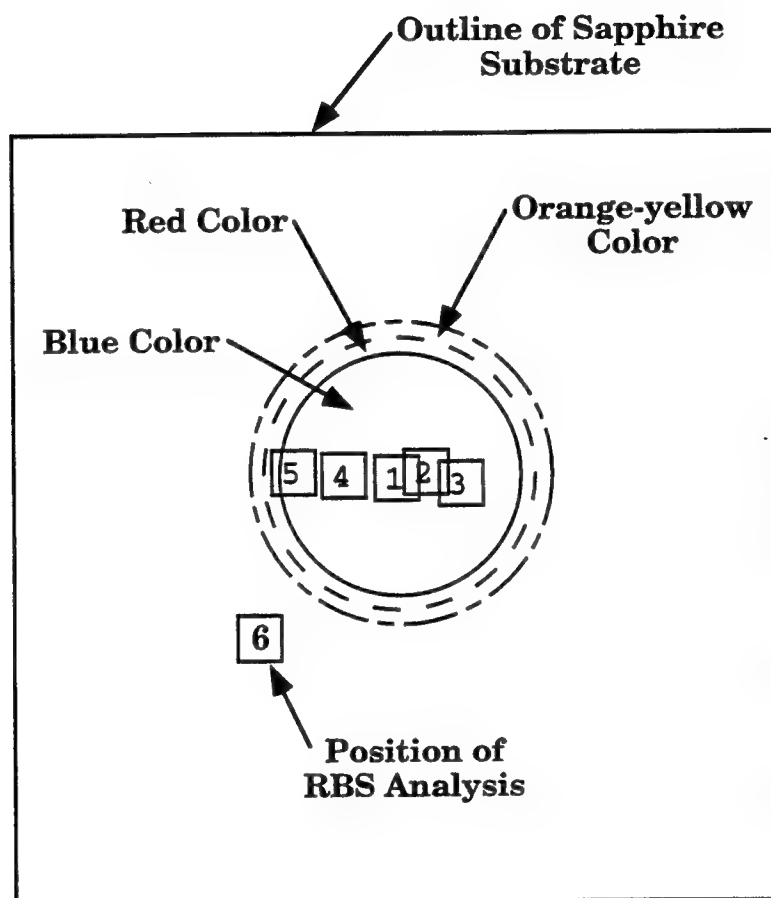
176

Figure A1.2. Schematic of RBS analysis positions on a thick film deposited at 300°C. The circles outline the pattern and colors visible on the sapphire due to the film.
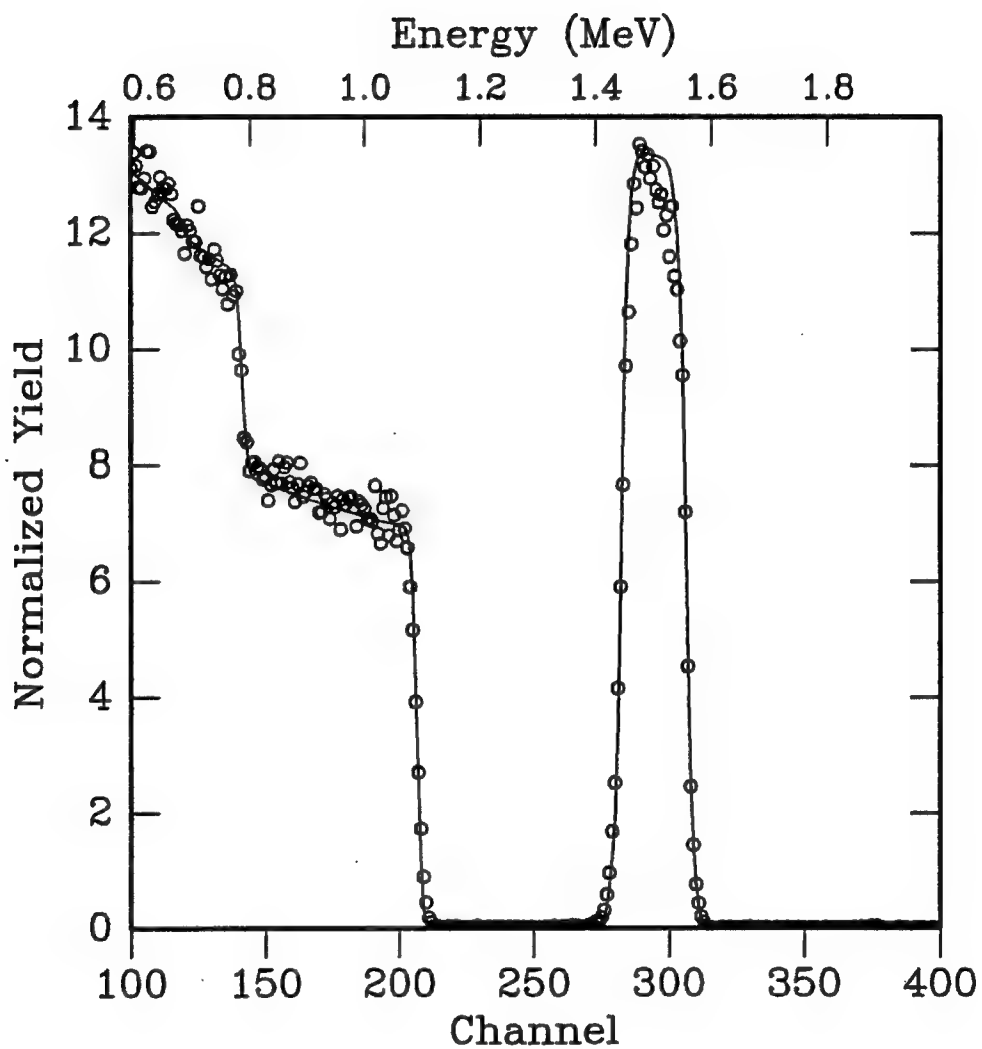
Figure A1.3. RBS spectrum from the center of a thick film grown at 300°C. The spectra corresponds to position 1 shown in Figure A1.2. The line is a RUMP simulation for a thickness of 1500 Å.

Table A1.2. RBS Thickness Profile of a Film Grown at 300°C

RBS Analysis Position	Thickness (Å)	Thickness / Thickness of Position 1
1	1500	1
2	1425	0.95
3	1350	0.9
4	1420	0.95
5	1175	0.78
6	750	0.5

circle is fairly rapid.

The thickness difference between positions 1 and 6 is a factor of 2. This agrees with the higher flux determined for the dosing tube compared to the chamber. The higher factor for the film thickness may be due to a slightly higher density of molecules at the immediate vicinity of the tube exit and substrate. The thickness profile suggests the dosing tube produces a higher growth rate by providing an increased flux. The presence of a circle due to deposition suggests a well collimated beam of molecules emerging from the dosing tube.

A1.4   Conclusions

The dosing tube flux was estimated to be 1.6 times higher than the chamber flux for a measured chamber pressure of 1.0×10^{-8} Torr. A thick film grown at 300°C appeared as a circle on the substrate. The film thickness profile indicated a uniform deposition across the circle within the limits of RBS analysis. The thickness at the circle center and outside the circle differed by a factor of two which agreed with the flux calculations. The circle suggests the dosing tube provides a collimated beam of precursor molecules for film deposition.

A1.5   References for Appendix 1

A1.1   V.S. Smentkowski and J.T. Yates, Jr., "A Multipurpose Quadrupole Mass Spectrometer Detector for Surface Kinetic and Absolute Surface Coverage Measurements," *J. Vac. Sci. Technol. A.*, **7** [6] 3325-3331 (1989).

A1.2   J.F. O'Hanlon, *A User's Guide to Vacuum Technology*; Ch. 13, pp. 12-13. John Wiley & Sons, New York, 1989.

A1.3   M.W. Roberts and C.S. McKee, *Chemistry of the Metal-Gas Interface*, Ch. 6, pp. 269-271. Oxford University Press, Oxford, 1978.

A1.4   Leybold Inficon, Inc., *Quadrex 200 Residual Gas Analyzer Manual*. East Syracuse, New York, 1988.

Appendix 2
Simulation of Uniform and Island Mode Films

A2.1 Introduction

The thicknesses of films grown by the cycling method were determined in Chapter 6 from the XPS Al $2p$ and Ti $2p_{3/2}$ photoelectron peak areas using a uniform overlayer model.[A2.1-3] The applicability of the model is evaluated in this appendix by applying it to simulated XPS peak intensities from films growing in uniform and island type modes. Islands were assumed to grow with constant fractional surface coverage from the substrate. This is also referred to as the Volmer - Weber growth mode. The simulations were for the Ti $2p_{3/2}$ photoelectron peak. Similar analysis is possible for the Al $2p$ photoelectron peak.

An analogous evaluation was made by Feldman and Mayer[A2.4] for the case of islands growing on an initial single monolayer of film. This is also known as the Stranski - Krastanov growth mode. In their analysis, a series of equations were proposed for island growth proceeding as one monolayer at a time for constant coverage. In this appendix, one equation is applied.

Peak intensities as a function of thickness follows an exponential relationship for uniform films. Similar simple quantitative expressions are not readily available for island growth.[A2.4]

A2.2   Simulation procedure

The procedure for evaluating the model consisted of simulating the XPS peak areas that would be observed if film grew as islands. The intensities were then converted to apparent film thicknesses by applying the uniform growth model. A linear least squares fit between film thickness and number of deposition cycles were then produced. The last steps are analogous to the procedure used in Chapter 6 to determine thicknesses from XPS photoelectron peak areas of films grown by the cycling method. The film growth modes were unknown.

Uniform overlayer thickness is determined from XPS Al $2p$ and Ti $2p_{3/2}$ photoelectron peak areas by using the following equations:[A2.1]

$$I^{Al} = I_\infty^{Al} \exp\left(\frac{-d_{am} \sec \theta}{\lambda_{am}^{TiO_2}\left(E_{Al\, 2p}\right)}\right) \qquad (A2.1)$$

$$I^{Ti} = I_\infty^{Ti} \left\{1 - \exp\left(\frac{-d_{am} \sec \theta}{\lambda_{am}^{TiO_2}\left(E_{Ti\, 2p_{3/2}}\right)}\right)\right\} \qquad (A2.2)$$

where I^{Al} and I^{Ti} are the Al $2p$ and Ti $2p_{3/2}$ photoelectron peak areas respectively, $\lambda_{am}^{TiO_2}\left(E_{Al\, 2p}\right)$ and $\lambda_{am}^{TiO_2}\left(E_{Ti\, 2p_{3/2}}\right)$ are the IMFP for the Al $2p$ and Ti $2p_{3/2}$ photoelectrons, respectively, and d_{am} is the overlayer film thickness in atomic monolayers. For a constant growth rate per cycle, d_{am} is related to the number of cycles, n_c, by the following equation:

$$d_{\text{am}} = \Delta d_{\text{amc}}\, n_c \qquad \text{(A2.3)}$$

where Δd_{amc} is the atomic monolayer growth rate per cycle. Detailed definitions for the terms in equations A2.1 to A2.3 were discussed in Chapter 6.

For the case of film growth where thickness is limited to one monolayer and surface coverage varies from 0 to 1, the Ti $2p_{3/2}$ intensities are given by the following equation: [A2.1,2]

$$I^{\text{Ti}} = \phi\, I_\infty^{\text{Ti}} \left\{ 1 - \exp\left(\frac{- \sec\theta}{\lambda_{\text{am}}^{\text{TiO}_2}\left(E_{\text{Ti}\,2p_{3/2}}\right)} \right) \right\} \qquad \text{(A2.4)}$$

where ϕ is the surface fractional coverage.

For films growing in the Volmer - Weber mode, the islands can be approximated as growing with a constant fractional coverage. The shape of actual islands are varied and may grow with changing coverage as in the case of hemispheres. The use of constant coverage provides a simple approximation. The Ti $2p_{3/2}$ intensities from a film growing with constant coverage can be determined from a modified form of equation A2.4. The equation is:

$$I^{\text{Ti}} = \phi\, I_\infty^{\text{Ti}} \left\{ 1 - \exp\left(\frac{- h_f\, d_{\text{am}}\, \sec\theta}{\lambda_{\text{am}}^{\text{TiO}_2}\left(E_{\text{Ti}\,2p_{3/2}}\right)} \right) \right\} \qquad \text{(A2.5)}$$

where h_f is a height factor. The height factor was determined by

comparing the thickness of islands and uniform films. For the same growth rate and number of cycles, the islands in a film growing with 50% constant coverage will have a thickness consistently twice that of a uniform film. The height factor would be 2.

Figure A2.1 shows the Ti $2p_{3/2}$ intensities as a function of number of growth cycles for films growing in a uniform manner and with constant 75, 50, and 25% coverage. The intensities for the uniform film were determined from equation A2.2. The intensities for the island films were determined from equation A2.5 using h_f of 1.33, 2, and 4 for coverages of 75, 50, and 25% coverage, respectively. The bulk intensity and Δd_{am} were taken as 31254 and 0.10 atomic monolayers per cycle, respectively. The intensities for the island films are lower compared to the uniform film. Each approaches a limit beyond which the intensity ceases to increase because the island heights are greater than the photoelectrons IMFP.

The intensities from Figure A2.1 were than converted to apparent film thicknesses assuming a uniform film. The following equation, which is another form of equation A2.2, was applied:

$$d_{am} = -\lambda_{am}^{TiO_2} \left(E_{Ti\,2p_{3/2}} \right) \cos \theta \ln \left\{ 1 - \left(I^{Ti} / I_{\infty}^{Ti} \right) \right\} \qquad (A2.6)$$

Figure A2.2 shows the apparent film thickness (atomic monolayers) as a function of number of cycles for the uniform and island growth films. The uniform film represents the actual thickness for 100% coverage. Deviation of island films from the uniform film increases with
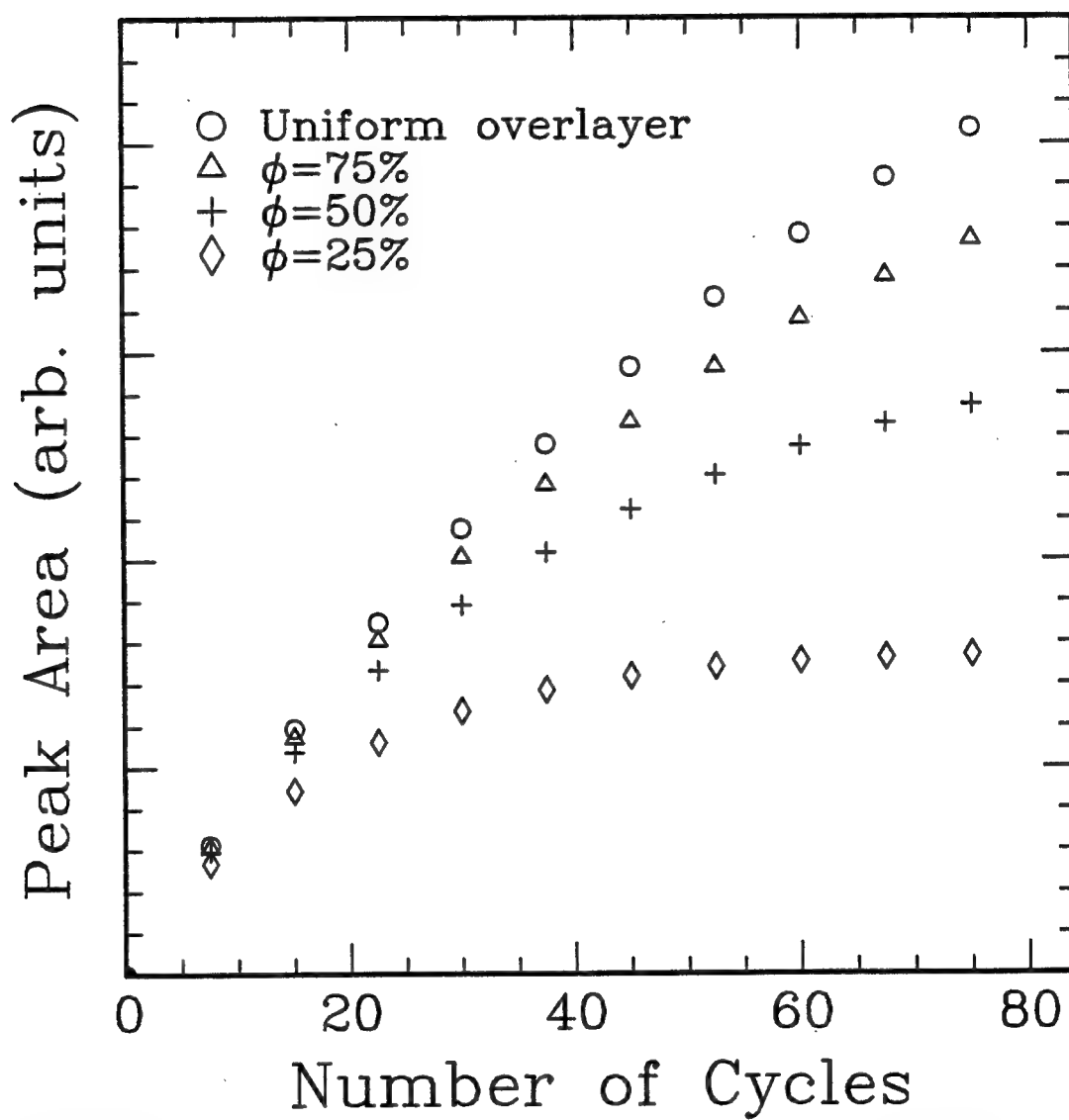
Figure A2.1. Simulated XPS Ti $2p_{3/2}$ photoelectron peak areas as a function of number of cycles. Simulations are for films with a uniform overlayer, and islands with 75, 50, and 25% constant coverage.
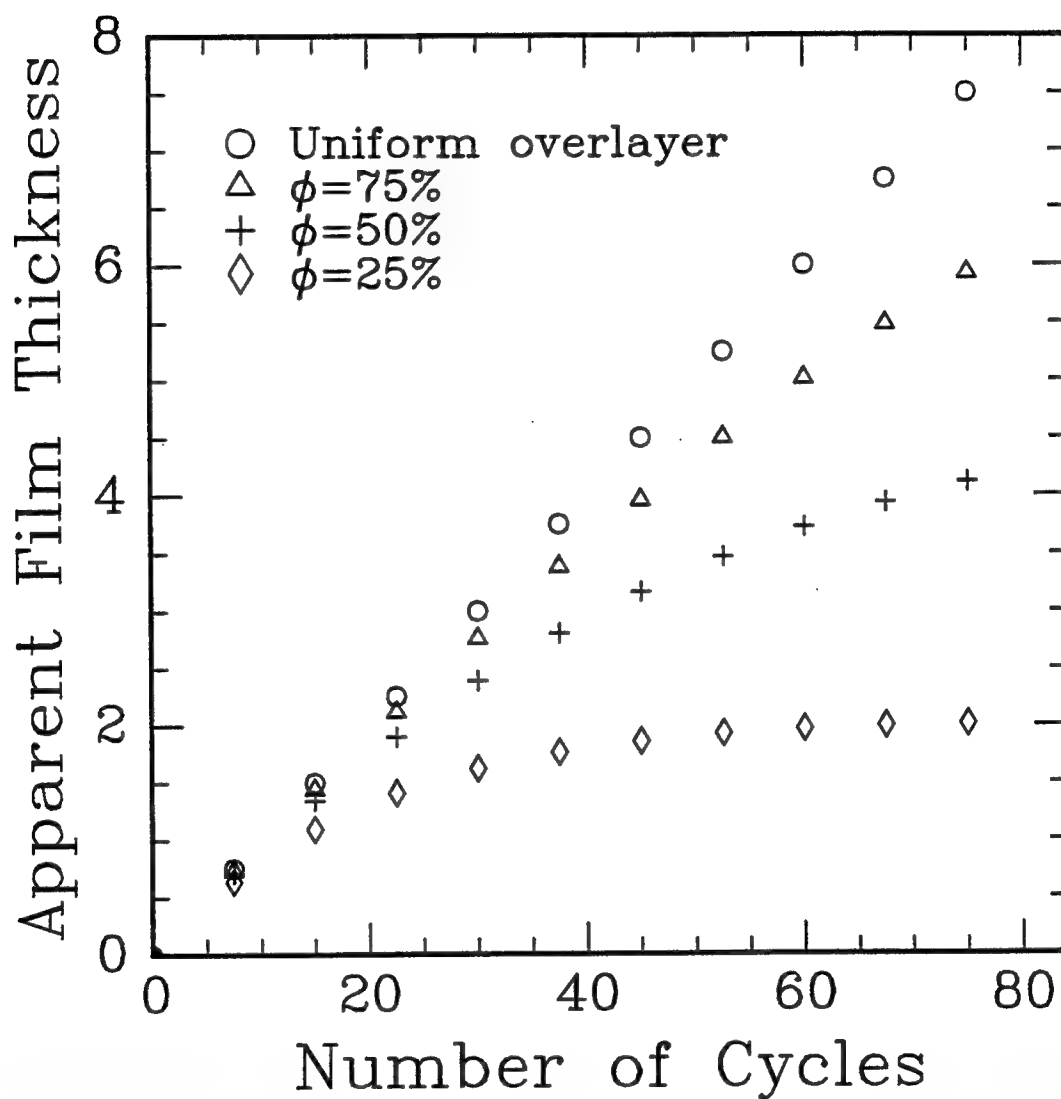
Figure A2.2. Apparent film thickness as a function of number of cycles for simulated films with a uniform overlayer, and islands with 75, 50, and 25% coverage. Film thicknesses (in atomic monolayers) were determined using a uniform overlayer model.

increasing uniform thickness and decreasing constant coverage.

Figure A2.3 shows linear least squares fits applied to the uniform and 75% coverage film. The uniform film shows the expected linear relation between thickness and number of cycles for a constant growth rate per cycle. The 75% coverage island film approaches a linear relation. Deviation of the film thickness and number of cycles from a linear relationship increases with increasing deviation from uniform growth.

The simulations suggest application of equations A2.1 and A2.2 to films with unknown growth modes should provide qualitative analysis of the extent growth deviates from an uniform mode. For uniform growth by a constant growth rate per cycle, the relationship between number of cycles and overlayer thickness should be linear.
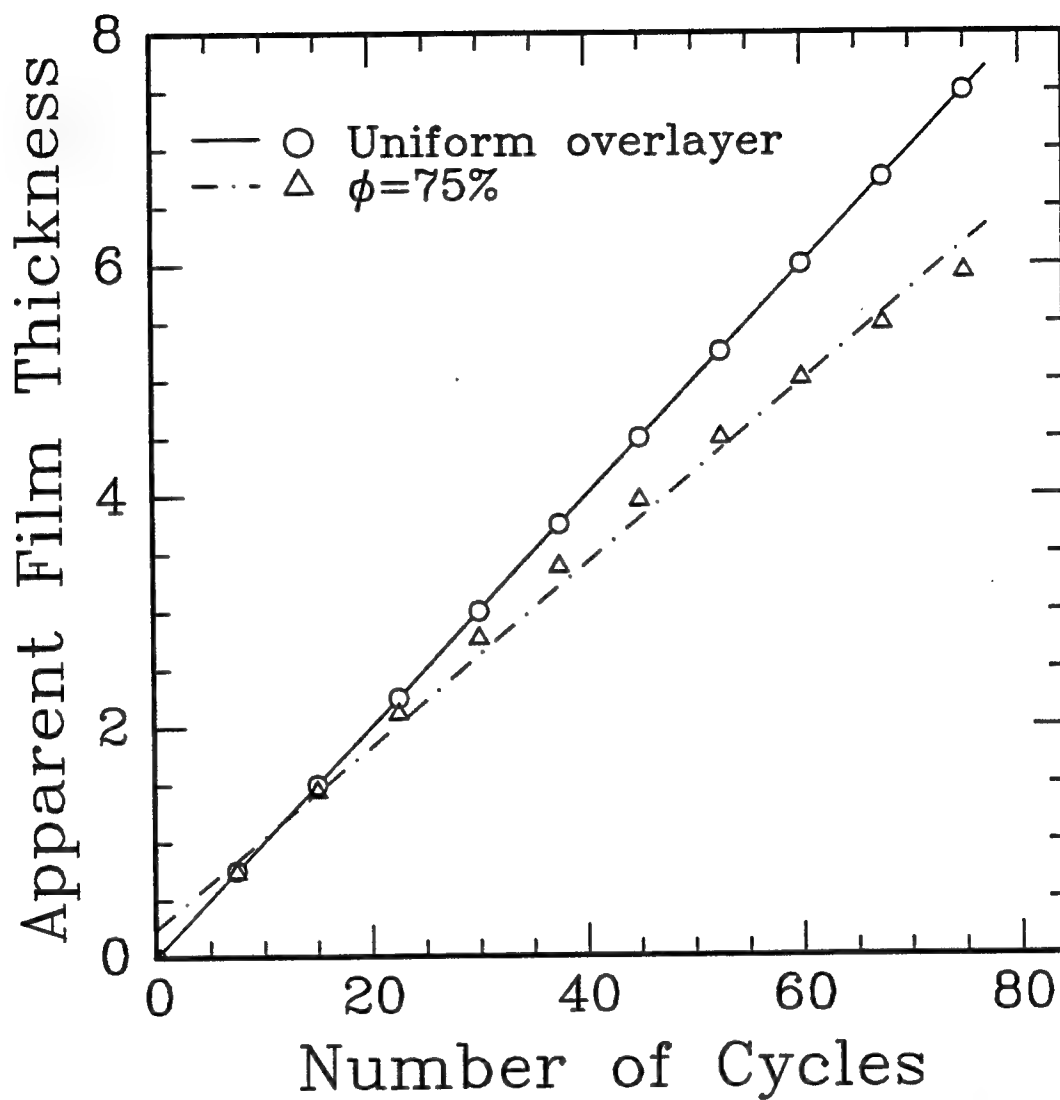
Figure A2.3. Apparent film thickness as a function of number of cycles for simulated films with a uniform overlayer, and islands with 75% coverage. Film thicknesses (in atomic monolayer) were determined using a uniform overlayer model. The lines shown are linear least squares fits.

A2.3 References for Appendix 2

A2.1 M.P. Seah and W.A. Dench, "Quantitative Electron Spectroscopy of Surface: a Standard Data Base for Electron Inelastic Mean Free Paths in Solids," *Surf. Interface Anal.*, **1** [1] 2-10 (1979).

A2.2 M.P. Seah, "Quantification of AES and XPS"; pp. 181-216 in *Practical Surface Analysis by Auger and X-ray Photoelectron Spectroscopy*. Edited by D. Briggs and M.P. Seah. John Wiley & Sons, Chichester, 1983.

A2.3 M.P. Seah, "The Quantitative Analysis of Surfaces by XPS: a Review," *Surf. Interface Anal.*, **2** [6] 222-39 (1980).

A2.4 L.C. Feldman and J.W. Mayer, *Fundamentals of Surface and Thin Film Analysis*; Ch. 6, pp. 125-53. North-Holland, New York, 1986.

Appendix 3
Simulation of XPS O 1s Peak Shift

A3.1   Introduction

In Section 7.3.2, experimental XPS O 1s peaks were compared with simulated shifted composite peaks for increasing film thickness. Details regarding the simulation are given in this appendix. The simulation assumes there is no interface reaction in which the titanium oxide film reduces the sapphire surface or charge transfer occurs. The XPS O 1s shift is due to oxygen in sapphire and titanium oxide having distinct and difference binding energy positions. Hereafter, oxygen from sapphire and titanium oxide will be referred to as O^S and O^T, respectively. There are three parts to the simulation. The first part relates peak height to film thickness. The second section simulates peak signals from O^S and O^T for incremental film thicknesses. The final section adds the peaks for each thickness.

A3.2   Simulation procedure

XPS peaks were simulated using the mixed Gaussian and Lorentzian function proposed by Evans.[A3.1] This function was used to curve fit experimental peaks in Chapters 5 and 6. The function is:[A3.1]

$$f(x) = \frac{\text{peak height}}{\left\{\left(1 + Q\, m^{1/2}\right) \exp\left[\left(1 - m^{1/2}\right)^{(0.87 - 0.1855\, m^{1/2})} Q \ln 2\right]\right\}} \quad \text{(A3.1)}$$

Q is given by:[A3.1]

$$Q = \frac{\left(x - x_o\right)^2}{w^2} \quad \text{(A3.2)}$$

where x_o, w, and m are the peak center, half width at half maximum (FWHM/2), and mixing factor. The function given in equation A3.1 represents a pure Gaussian or Lorentzian when m is 0 or 1, respectively. The x_o, w, m, and peak height must be known to simulate peaks. The function was related to film thickness, d (in molecular monolayers) by determining the relation between peak height and film thickness.

The peak intensities (heights and areas) for the O^S and O^T peaks will decrease and increase with d, respectively. Peak heights were related to thickness by first determining the relation between heights and areas.

For O^S, the relations between peak height and area was determined by simulating peaks using equation A3.1 for incremental heights. The w and m were taken from clean sapphire. They were assumed unchanged by film thickness. For the film grown by 60°C dose and 460°C anneal cycles, the w and m used were 1.26 eV and 0.3, respectively. For the film grown by 200°C dose and 700°C anneal cycles, the w and m center used were 1.135 eV and 0.3 eV, respectively. The position of the peak center was set at 531.0. The areas for each peak was then determined by integration. Peak height was determined to be

linearly related to peak area.

$$O^S \text{ peak height} = (ratioa) (peak area) \qquad (A3.3)$$

where ratioa is 0.390 and 0.433 for the films grown by 60°C dose and 460°C anneal cycles, and 200°C dose and 700°C anneal cycles, respectively. The difference between the two films may be caused by charging. The low energy electron flood gun was not used during XPS of the latter film.

The relation between O^T peak height and area was determined in a similar manner. The w and m used were from thick films and are 1.04 eV and 0.2, respectively. A description of these films were given in Section 5.3.4. The relation was determined to be:

$$O^T \text{ peak height} = (ratiot) (peak area) \qquad (A3.4)$$

where ratiot is 0.474.

Peak areas are related to film thicknesses by the following equations:[A3.2]

$$I^{O^S} = I_\infty^{O^S} \exp\left(\frac{-d_{am} \sec \theta}{\lambda_{am}^{TiO_2} (E_{O\,1s})}\right) \qquad (A3.5)$$

$$I^{O^T} = I_\infty^{O^T} \left\{1 - \exp\left(\frac{-d_{am} \sec \theta}{\lambda_{am}^{TiO_2} (E_{O\,1s})}\right)\right\} \qquad (A3.6)$$

where I^O, I_∞, d_{am}, and λ are the peak areas for a particular thickness, peak areas from bulk standards, film thickness in atomic monolayer, and IMFP. Determination of I_∞ was described in Section 5.3.4. The relation between d and d_{am} was given in equation 6.6. Assuming an anatase TiO_2 phase:

$$d = 0.697\, d_{am} \qquad (A3.7)$$

Since the XPS energy positions for O^S and O^T differ by at most 1.3 eV, the IMFP are assumed to be the same. Since the relations between peak height and area, and area and thickness are known, peak height can be related to film thickness.

In the second part of the simulation, peaks for O^S and O^T were simulated using equation A3.1 for different thicknesses. The O^S peak for films grown by 60°C dose and 460°C anneal cycles, and 200°C dose and 700°C anneal cycles were fixed at 531.34 and 531.42 eV, respectively. These were the O 1s peak positions from the clean sapphire referenced to Al 2p at 74.4 eV.[A3.3] The O^T peak was fixed at a total O 1s shift relative to the O^S.

In the last part of the simulation, for each thickness, O^S and O^T peaks were added together to form a single composite peak. Simulations were produced for total shifts ranging from -0.99 to -1.23 eV. Figures showing the simulated O^S and O^T and composite peaks overlaid on experimental peaks for different thicknesses and total shifts were presented in Chapter 7.

A3.3 References for Appendix 3

A3.1   S. Evans, "Curve Synthesis and Optimization Procedures for X-ray Photoelectron Spectroscopy," *Surf. Interface Anal.*, **17**, 85-93 (1991).

A3.2   M.P. Seah and W.A. Dench, "Quantitative Electron Spectroscopy of Surface: a Standard Data Base for Electron Inelastic Mean Free Paths in Solids," *Surf. Interface Anal.*, **1** [1] 2-10 (1979).

A3.3   J.F. Moulder, W.F. Stickle, P.E. Sobol, and K.D. Bomben, *Handbook of X-ray Photoelectron Spectroscopy*. Edited by J. Chastain. Perkin Elmer Corporation, Eden Prairie, Minnesota, 1992.